Effective Date: July 22, 2022
Revision B

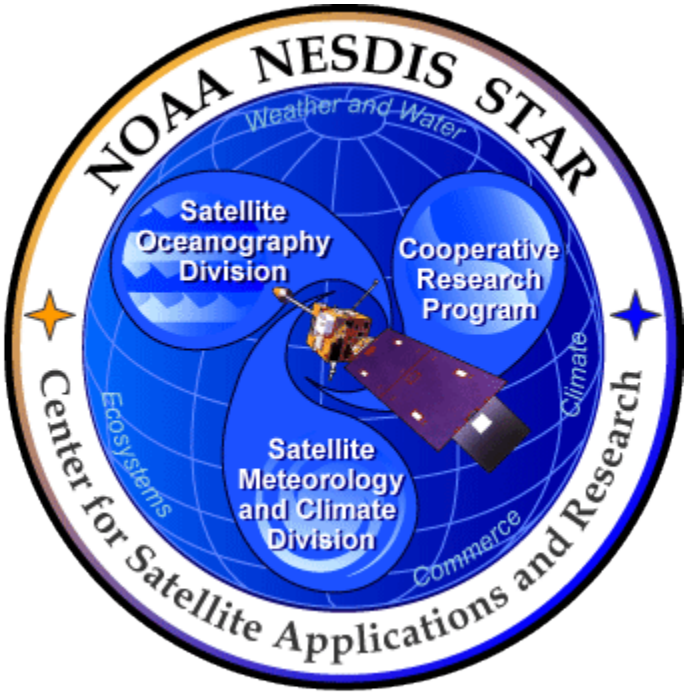

NOAA NESDIS
CENTER for SATELLITE APPLICATIONS and RESEARCH

Joint Polar Satellite System (JPSS) VIIRS Geolocation Algorithm Theoretical Basis Document (ATBD)

https://www.star.nesdis.noaa.gov/jpss/Docs.php

Effective Date: July 31, 2011
Revision -

GSFC JPSS CMO
December 5, 2011
Released

Joint Polar Satellite System (JPSS) Ground Project
Code 474
474-00053

Joint Polar Satellite System (JPSS) VIIRS Geolocation Algorithm Theoretical Basis Document (ATBD)

For Public Release

Goddard Space Flight Center
Greenbelt, Maryland

National Aeronautics and
Space Administration

This page intentionally left blank.

Joint Polar Satellite System (JPSS)
VIIRS Geolocation Algorithm Theoretical Basis Document (ATBD)

JPSS Electronic Signature Page

Prepared By:

Neal Baker
JPSS Data Products and Algorithms, Senior Engineering Advisor
(Electronic Approvals available online at https://jpssmis.gsfc.nasa.gov/mainmenu_dsp.cfm)

Approved By:

Heather Kilcoyne
DPA Manager
(Electronic Approvals available online at https://jpssmis.gsfc.nasa.gov/mainmenu_dsp.cfm)

Goddard Space Flight Center
Greenbelt, Maryland

This page intentionally left blank.

Preface

This document is under JPSS Ground AERB configuration control. Once this document is approved, JPSS approved changes are handled in accordance with Class I and Class II change control requirements as described in the JPSS Configuration Management Procedures, and changes to this document shall be made by complete revision.

Any questions should be addressed to:

JPSS Ground Project Configuration Management Office
NASA/GSFC
Code 474
Greenbelt, MD 20771

This page intentionally left blank.

Change History Log

Revision	Effective Date	Description of Changes (Reference the CCR & CCB/ERB Approve Date)
Original	04/22/2011	**474-CCR-11-0068:** This version baselines D43776, VIIRS Geolocation Algorithm Theoretical Basis Document ATBD, Rev D, dated 12/17/2010, as a JPSS document, version Rev –. This is the version that was approved for NPP launch. Per NPOESS CDFCB - External, Volume V – Metadata, doc number D34862-05, this has been approved for Public Release into CLASS. This CCR was approved by the JPSS Algorithm ERB on April 22, 2011.
STAR Rev A	03/08/2017	Added Appendix C: JPSS-1 VIIRS DNB Aggregation Mode Change to Mitigate DNB Non-linearity that documents algorithm changes for CCR-15-2590.
STAR Rev B	07/22/2022	Updated the documentation, but not the operational algorithm, for making the ATBD applicable for JPSS-2 VIIRS.

This page intentionally left blank.

NATIONAL POLAR-ORBITING OPERATIONAL ENVIRONMENTAL SATELLITE SYSTEM (NPOESS)

VIIRS Geolocation

Algorithm Theoretical Basis Document (ATBD)

CDRL No. A032

Northrop Grumman Space & Mission Systems Corporation

One Space Park

Redondo Beach, California 90278

This document has been identified per the NPOESS Common Data Format Control Book – External Volume 5 Metadata, D34862-05, Appendix B as a document to be provided to the NOAA Comprehensive Large Array-data Stewardship System (CLASS) via the delivery of NPOESS Document Release Packages to CLASS.

The information provided herein does not contain technical data as defined in the International Traffic in Arms Regulations (ITAR) 22 CFR 120.10.
This document has been approved by the Unites States Government for public release in accordance with NOAA NPOESS Integrated Program Office.

Distribution: Statement A: Approved for public release; distribution is unlimited.

NATIONAL POLAR-ORBITING OPERATIONAL ENVIRONMENTAL SATELLITE SYSTEM (NPOESS)

VIIRS Geolocation

Algorithm Theoretical Basis Document (ATBD)

PREPARED BY:

Stephanie Weiss

ELECTRONIC APPROVAL SIGNATURES:

_____

Roy Tsugawa Date
Algorithm & Data Processing IPT Lead &
Algorithm Change Control Board Chairperson

_____

Gerald J. Mulvey Date
Senior Systems Engineer

The following individuals are recognized for their contributions to the current or previous versions of this document.

Jim Storey, Bill Byerly, Stephanie Weiss

Revision/Change Record

Document Number D43776

Revision	Document Date	Revision/Change Description	Pages Affected
---	02/05/2007	Initial PCIM Release to bring document into Matrix Accountability. Reference original document number: Y3258 delivered in 2005	All
A	5/21/2008	ATBD Updates under SPCR ALG00001309: - Updated formatting for Section Headings, Figures, Tables, and Equations (includes renumbering some Figures, Tables, and Equations). - Changed all references to Sections, Tables, Figures, Equations, and Footnotes to cross-referenced hyperlinks. - Updated Table 2.2-1 - Updated Table 3.3-2 (previously labeled 3.3-1B) - Updated Table 3.3-3 (previously labeled 3.3-1C) - Updated Figure 3.3-11 (previously labeled 3.3-10A) - Updated Table 3.3-5 (previously labeled Table 3.3-3) - Updated Figure 3.3-3 - Added Figure 3.3-5 - Updated Figure 3.3-6 (previously labeled 3.3-5) - Updated Section 3.3.1.2.5 - Updated Frame Time Tagging Eqn 3.3-24 in Section 3.3.2.1.3 - Updated Section 3.3.2.1.6 - Updated Section 3.3.2.1.7 - Added Figure 3.3-18 and Figure 3.3-19 - Added Equations 45 and 46	All
B	12/19/2008	ATBD updates under SPCR ALG00001357 were made to address CDA RFA comments. RF561-3: - Section 1.4: Second paragraph, removed statement about updating the Error Analysis with latest error budget models. - Section 3.4: First paragraph, updated to clarify that the error analysis in the ATBD was intended to be a snapshot of the current best estimates at the time of publication, and removed references to updating with latest STOP model numbers. RF561-4: - Section 4.2: First bullet, deleted the second sentence indicating that correction for atmospheric refraction was going to be added to the baseline software. General Updates: Fixed numbering to start at Section 1 and use roman numerals for TOC, TOF, TOT, Acronyms etc.	Page 6 Page 80 Page 117 All

Revision/Change Record

Document Number D43776

Revision	Document Date	Revision/Change Description	Pages Affected
C	3/17/2010	ATBD updates under SPCR ALG00001566: - Deleted Appendix C on FU1 parameters, this information will be reported in a separate document - Updated cover page - General updates throughout document to note that the scan angles reported are computed based on a nominal scan rate - Updated outdated references - Reference ECR A-280B - Approved for Public Release per Contracts Letter 100730-1.	All
D	12/17/2010	ATBD updates under SPCR ALG00001645: - Updated Section 1 to include current program information - Updated Section 3.3.2.1.3 description for frame time equation - Eqn 3.3-24: Updated frame time equation to add the T_{reset} term to Δt rather than subtract it. This essentially moves the readout to occur at the beginning of the frame time rather than at the end. Also changed the EV delay time to use the *earth_view_delay* terminology as used by the code. - Updated Section 3.3.2.1.6 - added details of current implementation of the encoder processing and interpolation method, and updated all equations in the section (3.3-33 through 3.3-44) to reflect current implementation.	All

TABLE OF CONTENTS

Page

LIST OF FIGURES

LIST OF TABLES

GLOSSARY OF ACRONYMS

ATBD	Algorithm Theoretical Basis Document
AVHRR	Advanced Very High-Resolution Radiometer
BOS	Beginning of Scan
CCD	Charge Coupled Device
CDR	Critical Design Review
CTS	Conventional Terrestrial System
DCW	Digital Chart of the World
DEM	Digital Elevation Model
DMSP	Defense Meteorological Satellite Program
DNB	Day-Night Band
DoD	Department of Defense
DTED	Digital Terrain Elevation Database
DWSS	Defense Weather Satellite System
ECEF	Earth Centered Earth Fixed
ECI	Earth Centered Inertial
ECR	Earth Centered Rotating
ECS	EOSDIS Core System
EDC	EROS Data Center
EDR	Environmental Data Record
EM	Electronics Module
EOS	Earth Observing System
EOS	End of Scan
EOSDIS	Earth Observing System Data and Information System
EROS	Earth Resources Observation System
ETM+	Enhanced Thematic Mapper Plus
FOV	Field of View
FPA	Focal Plane Assembly
GCP	Ground Control Point
GIFOV	Ground Instantaneous Field of View
GIID	General Instrument Interface Document
GPS	Global Positioning System
GTOPO-30	Global Topography - 30 arc seconds
HAM	Half Angle Mirror
HDF-EOS	Hierarchical Data Format-Earth Observing System

IDPS	Integrated Data Processing Segment
IERS	International Earth Rotation Service
IFOV	Instantaneous Field of View
IPO	Integrated Program Office
ITSS	Information Technology and Scientific Services
JPSS	Joint Polar Satellite System
Landsat	Land Remote Sensing Satellite
LLLS	Low Level Light Sensor
LOS	Line of Sight
LWIR	Long Wave Infrared (spectral bands)
MODIS	Moderate-Resolution Imaging Spectroradiometer
MSS	Multi-spectral Scanner
MTF	Modulation Transfer Function
NIMA	National Imagery and Mapping Agency
NIR	Near Infrared (spectral bands)
NASA	National Aeronautics and Space Administration
NOAA	National Oceanic and Atmospheric Administration
NPOESS	National Polar-orbiting Environmental Satellite System
NPP	NPOESS Preparatory Project
OLS	Operational Linescan System
PDR	Preliminary Design Review
POES	Polar Operational Environmental Satellite
QA	Quality Assurance
RDR	Raw Data Record
RSS	Root Sum Square
RTA	Rotating Telescope Assembly
SBRS	Santa Barbara Remote Sensing
S/C	Spacecraft
SDP	Science Data Processing
SDPTK	Science Data Processing Toolkit
SDR	Sensor Data Record
SDSM	Solar Diffuser Stability Monitor
SDST	Science Data Support Team
S/MWIR	Short and Mid-Wave Infrared
SPOT	System pour l'Observation de la Terre
SRTM	Shuttle Radar Topography Mission

SSPR	Shared System Performance Responsibility
STOP	Structural, Thermal and Optical Properties
TBR	To Be Revised
TIROS	Television Infrared Observation Satellite
TM	Thematic Mapper
TOA	Top of Atmosphere
USA	United States of America
USGS	United States Geological Survey
USNO	United States Naval Observatory
VIIRS	Visible/Infrared Imager/Radiometer Suite
Vis/NIR	Visible/Near Infrared
WGS84	World Geodetic System 1984

ABSTRACT

The Visible Infrared Imaging Radiometer Suite (VIIRS) geolocation algorithm is part of the VIIRS raw data processing software. Its purpose is to provide Earth location and related spatial information for the various VIIRS data products. Geolocation data fields will be computed for each resolution's ideal band pixels. The Earth location fields, including geodetic latitude, longitude, and height are computed using rigorous models of the Earth and VIIRS instrument pointing. These models account for instrument dynamics including the rotating telescope and half angle mirror, spacecraft position, velocity, and attitude, and the WGS84 ellipsoid, geoid, and Earth's terrain surface

Routine geolocation processing will generate the required data fields using the engineering and spacecraft auxiliary data contained in the VIIRS mission and spacecraft data streams. Offline calibration and analysis activities will ensure the quality of the Earth location data using ground control and instrument/spacecraft parameter estimation techniques. These activities will be particularly intense during the initial checkout and early orbit period when static pointing biases will be measured and removed. Earth location error propagation analyses based on estimates of the spacecraft and instrument performance indicate that the net Earth location accuracy after removal of static biases will be better than the three sigma geolocation requirements throughout the scan.

1. INTRODUCTION

The Visible/Infrared Imager Radiometer Suite (VIIRS) is designed to be carried aboard a sun-synchronous polar orbiting satellite – originally on each platform of the National Polar-orbiting Operational Environmental Satellite System (NPOESS). NPOESS was planned as a joint mission among the Department of Defense (DoD), the National Oceanic and Atmospheric Administration (NOAA), and the National Aeronautics and Space Administration (NASA). The VIIRS is a single visible/infrared instrument capable of satisfying the needs of all three communities, as well as the general research community. As such, the VIIRS has two key attributes: high spatial resolution with controlled growth off nadir, and a large number of spectral bands to satisfy the requirements for generating accurate operational and scientific products.

In February 2010, the Director of the Office of Science and Technology Policy (OSTP), as part of the Executive Office of the President, announced that NOAA and DOD will no longer jointly procure the NPOESS satellite system; instead, each agency would plan and acquire its own satellite system. NOAA is to be responsible for the afternoon orbit and the observations planned for the first and third NPOESS satellites, and DOD is to be responsible for the morning orbit and the observations planned for the second and fourth NPOESS satellites. The Joint Polar Satellite System (JPSS) is the name for the restructured civilian portion of NPOESS, where the word “joint” refers to the collaboration between NASA and NOAA. The Defense Weather Satellite System (DWSS) is the name given for the restructured military portion of NPOESS. Both JPSS and DWSS planned to include VIIRS on all of their respective satellites, but DWSS was cancelled in 2012.

JPSS provides an enduring capability to measure, on a global basis, atmospheric, land, and ocean environmental parameters. The system provides timely and accurate weather and environmental data to weather forecasters, military commanders, civilian leaders, and the scientific community. JPSS satellites operate in near circular, sun-synchronous orbits. Suomi National Polar-orbiting Partnership (Suomi NPP), formerly known as the NPOESS Preparatory Project, satellite was launched in 2011, and carried some of the instruments originally planned for NPOESS, including the VIIRS, whose geolocation algorithm is the subject of this document. The follow-on NOAA-20 satellite, originally named JPSS-1 (J1), was launched in 2017. The JPSS-2 (J2) satellite is planned to be launched in 2022. The JPSS satellites carry sensors operating in different frequency regions of the electromagnetic spectrum and have ascending node equatorial crossings around 13:30 (1:30 P.M.) local sun time. In the NPOESS specification, there were approximately five dozen remote sensing products, each of which is referred to as an Environmental Data Record (EDR) to be retrieved from the radiometric data collected by NPOESS and among them six are considered to be “key” parameters. VIIRS provides 23 of these EDRs including two (imagery and sea surface temperature) that are key parameters.

1.1. HISTORICAL PERSPECTIVE

VIIRS can be considered as a convergence of three existing sensors; the Operational

Linescan System (OLS), the Advanced Very High Resolution Radiometer (AVHRR), and the Moderate Resolution Imaging Spectroradiometer (MODIS). The OLS and AVHRR have seen extensive operational use. MODIS on the *Terra* satellite has been operational since 1999 and MODIS on the *Aqua* satellite has been operational since 2002.

The OLS is the operational visible/infrared scanner for the DoD. Its unique strengths are controlled growth in spatial resolution through rotation of the ground instantaneous field of view (GIFOV) and the existence of a low-level light sensor (LLLS) capable of detecting visible radiation at night. OLS has primarily served as a data source for manual analysis of imagery. The VIIRS Day-Night Band (DNB) has similar capabilities and functions. The AVHRR is the operational visible/infrared instrument flown on the NOAA Television Infrared Observation Satellite (TIROS-N) series of satellites [Planet, 1988]. Its unique strengths are low operational and production cost and the presence of five spectral channels that can be used in a wide number of combinations to produce operational and research products. In December 1999, NASA launched the Earth Observing System (EOS) morning satellite, *Terra*, which includes MODIS. In May 2002, a second MODIS was put into orbit onboard the EOS *Aqua* spacecraft. The third MODIS on the EOS *Aura* satellite was launched on 2004 July 15. MODIS possesses an unprecedented array of thirty-six spectral bands at resolutions ranging from 250 m to 1 km at nadir, allowing for a wide range of satellite-based environmental measurements.

Similar geolocation algorithms are widely used in modeling and geometrically correcting satellite image data from EOS MODIS, Land Remote Sensing Satellite (Landsat) Multi-spectral Scanner (MSS), Landsat Thematic Mapper (TM), System pour l'Observation de la Terre (SPOT), and AVHRR missions. In each case, the fundamental problem is in computing the point at which the sensor line of sight (LOS) intersects the Earth ellipsoid and/or terrain surface, leading to much commonalty among these algorithms. Experience with SPOT, AVHRR, and MODIS data in particular has demonstrated the importance of compensating for the effects of terrain relief when Earth locating off-nadir satellite imagery.

Figure 1.1-1 shows a comparison of VIIRS pixel sizes to the heritage AVHRR and OLS instruments' pixels. Off-nadir pixel growth of the fine resolution imaging bands (the 'I' bands) and the moderate resolution radiometric bands (the 'M' bands) is limited by employing an along scan sample aggregation approach that is described in Section 3.3.1.1.

In the VIIRS data processing system the geolocation algorithm is used to tag each calibrated top of atmosphere (TOA) radiance retrieval with its locational "attributes." This geolocated radiance product is referred to as a Sensor Data Record (SDR). The SDR attributes contribute to the subsequent science processing and can ultimately be used to perform spatial resampling, if desired. In most Landsat and SPOT applications, the geolocation data are used immediately, prior to data analysis, to resample the instrument detector output to an Earth referenced grid. This contrasts with the spatial attribute tagging approach used for the VIIRS, which is similar to the approach used by the MODIS geolocation algorithm. This difference in philosophy leads to data processing and data storage considerations that are somewhat unusual for the VIIRS geolocation algorithm.

Two places where this is particularly relevant are the density at which geolocation fields must be stored to capture the high spatial frequency variations due to terrain relief, and the need to defer band and detector alignment correction until later in the processing stream.

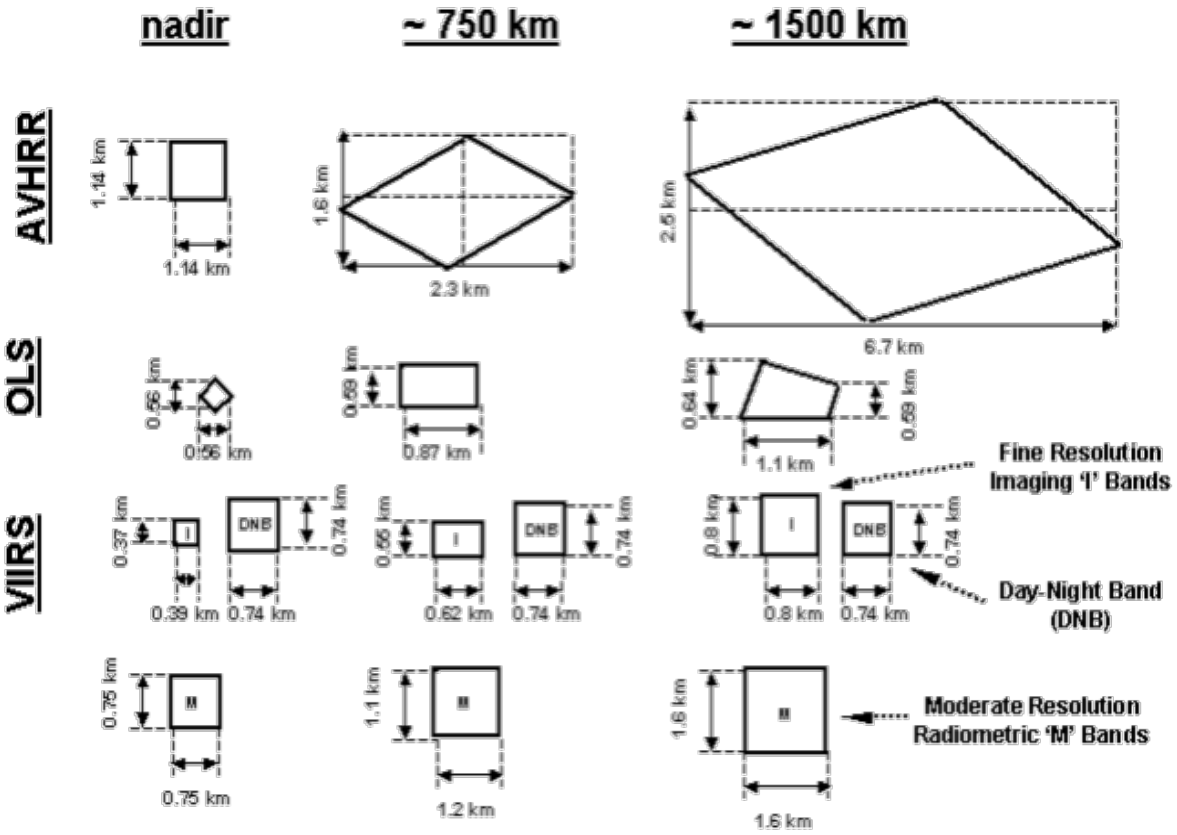

Figure 1-1: VIIRS, OLS, and AVHRR Spatial Resolution

1.2. PURPOSE

This Algorithm Theoretical Basis Document (ATBD) describes the VIIRS geolocation algorithm. This algorithm will be implemented as part of the VIIRS Raw Data Record (RDR) to SDR processing software in order to include Earth location and related spatial information in the VIIRS data products. The geolocation algorithm uses Earth ellipsoid and terrain surface information in conjunction with spacecraft (S/C) ephemeris and attitude data, and knowledge of the VIIRS instrument and satellite geometry to compute geodetic coordinates (latitude and longitude), height, ground to satellite direction and range, and solar and lunar vectors. The heart of the algorithm is a mathematical procedure that intersects the VIIRS instrument's LOS with the U. S. DoD World Geodetic System 1984 (WGS84) ellipsoid and with the Earth's terrain surface (see Section 3.3.2.2). Section 3.4 discusses estimates of uncertainty and product accuracy issues.

1.3. SCOPE

This document describes the conceptual approach and associated mathematical development used to compute the absolute spatial locational attributes for VIIRS Earth view data taken in one of VIIRS' operational modes. In diagnostic mode Earth view science data may be taken from a reduced scan width although this scenario is not described explicitly in this ATBD. This ATBD supports processing options to geolocate to the WGS84 ellipsoid or to the Earth's surface and to correct geolocation for temperature effects that may occur on orbit. Some suggestions are provided regarding key implementation issues, but the goal of this document is not to prescribe any particular implementation strategy.

Adjustments to Earth location to remove the parallax positioning errors that are due to cloud viewing geometry are made within the VIIRS Cloud Module. An appendix to the VIIRS Cloud Cover Layers Unit Level Detailed Design Document [Y2494] describes this algorithm.

This document describes the algorithm used to generate these Earth location and related fields and briefly discusses the supporting data preparation and validation processes.

This document summarizes the theoretical basis, development process, and functional flow of the VIIRS geolocation estimation process. This document identifies sources of input data (both VIIRS and non-VIIRS) that are required for the geolocation retrieval. It provides theory and mathematical background underlying the use of this information in the retrieval process. The implementation, assumptions, and limitations of the adopted approach are also discussed in this document. Some results and validation of the algorithm are also discussed. The main purpose is to provide a sound, repeatable, step-by-step approach for estimating geolocation within the limits required by the VIIRS EDR Mapping Uncertainty requirements in Appendix D of the NPOESS System Specification [SY15-0007].

An overview of the various sections in this document is presented in Figure 1.3-1. Also, an overview of the various coordinate systems and their relationships are illustrated in Figure 1.3-2. Throughout this document are references to various Raytheon Santa Barbara Remote Sensing (SBRS) and NPOESS Shared System Performance Responsibility (SSPR) documents. These references use the SBRS or SSPR document number set in italic font and enclosed in brackets (e.g. *[Y12345]*). When a document is first referenced its complete title is given along with the document number.

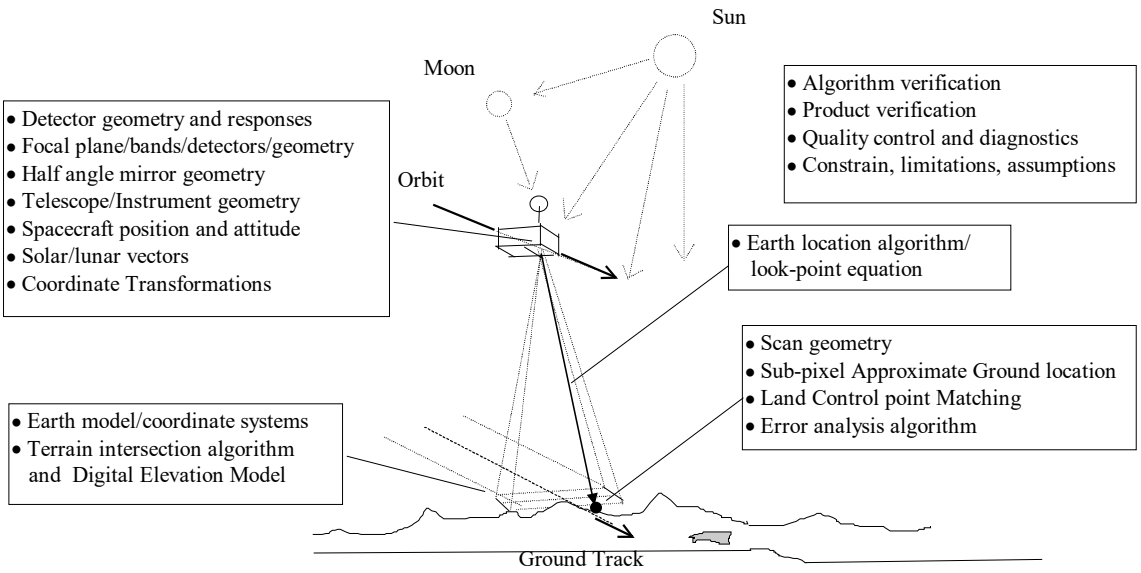

Figure 1-2: VIIRS Instrument and Support Overview

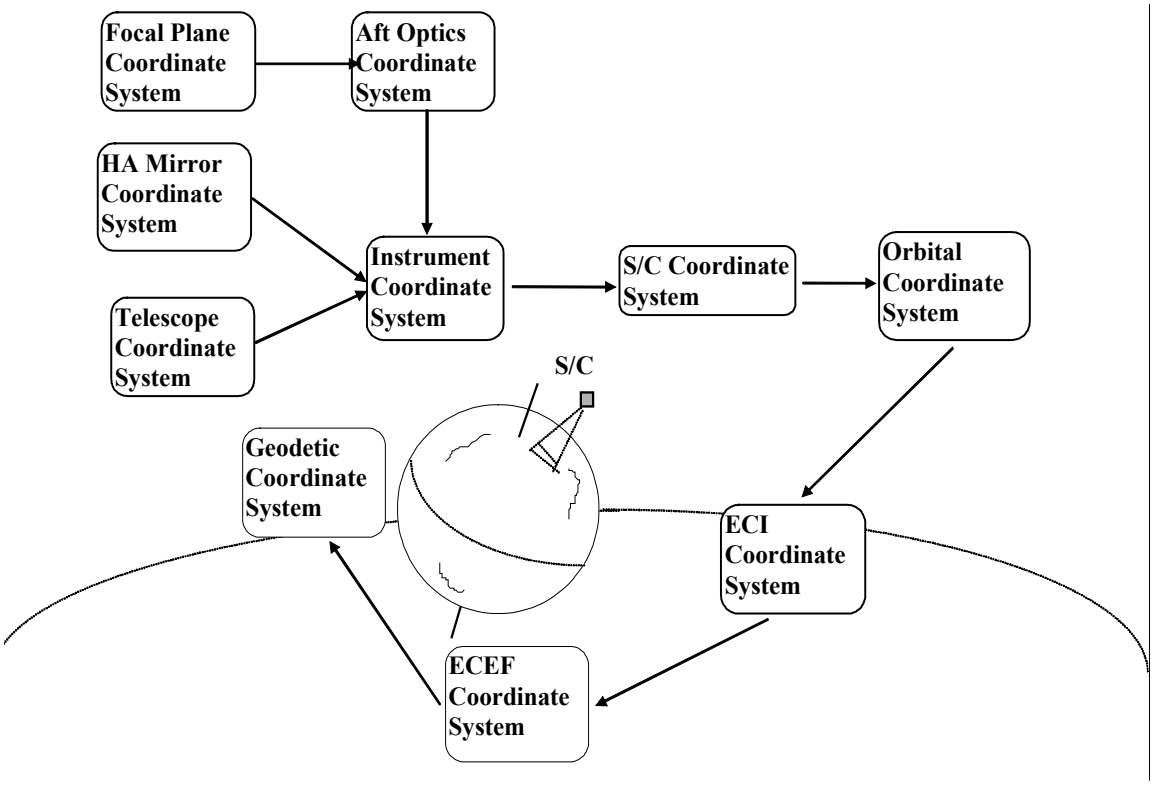

Figure 1-3: Coordinate Systems Overview and Coordinate Transformations

1.4. REVISIONS

Raytheon ITSS delivered the ATBD as Document Y3258, Version 5, Revision 4, in August 2004. At that time, NG took control of the document and in February 2007, it was incorporated into the NG document control system as D43776. All changes made since then are recorded in the Revision Change Record Table at the beginning of this document. Changes made before that time are recorded in this section.

Version 5 revision 5 updates were performed at NG as part of an algorithm update delivered to IDPS in November 2005. Version 5, Rev 5 includes the addition of some missing equations and a description of the solar diffuser coordinate system.

Version 5 revision 2 and version 5 revisions 3 and 4 are post-VIIRS Critical Design Review (CDR) deliverables, dated April 2004 and August 2004. The algorithm modifications documented herein were developed during a period of VIIRS algorithm continuance prior to delivery to the NPOESS Integrated Data Processing Segment (IDPS) for science to operational conversion. These algorithm modifications addressed *NPOESS General Instrument Interface Document (GIID) [D31418]* compliance and the addition of a temperature related correction methodology. Details concerning time tagging and updates to reflect the current state of the VIIRS design have been added. Revision 3 addresses comments made on the revision 2 document.

The error analysis and sensitivity studies section (Section 3.4) was not updated with this revision.

Constants related to the VIIRS design and operation were included in the document as representative of the VIIRS flight models. The actual values for each sensor may vary from those that are presented in this document version.

Version 5 was the third working version of this document and was a VIIRS Critical Design Review (CDR) deliverable. Revision 1 incorporated corrections and clarifications that were motivated by comments from the CDR. It was dated May 2002. Version 4 and Version 5 and its revision were prepared by Bill Byerly of Raytheon Information Technology and Scientific Services (ITSS). At the time of its writing some of the fine details of the VIIRS design were not finalized.

Version 4 was issued in May 2001 to address comments received from the VIIRS Preliminary Design Review (PDR). Version 3 was the first version of this ATBD. Its version number was chosen to match the delivery of the previously existing VIIRS EDR ATBDs, which had undergone two previous version releases. This version of the ATBD was written by Jim Storey of Raytheon ITSS and drew heavily upon the MODIS Level 1A Earth Location ATBD Version 3.0 (Nishihama *et al*, 1997).

[This page is intentionally blank]

2. EXPERIMENT OVERVIEW

2.1. OBJECTIVES OF GEORETRIEVAL

Each band type's pixel is assigned geolocation and related data fields for use in data processing and data analysis. The geolocation and related data fields include geodetic latitude, longitude, height above the Earth ellipsoid, satellite zenith angle, satellite azimuth, range to the satellite, solar zenith angle, solar azimuth, and (for the DNB) lunar zenith angle, lunar azimuth, and lunar phase. These data will be used in subsequent science processing, as well as by the end users of all product levels.

The geolocation latitude and longitude reference is needed to relate the VIIRS science data to other spatially referenced data sets, including other VIIRS data, and to provide a uniform, worldwide spatial reference system for all data products. Earth locations are provided for each pixel in order to capture the terrain relief parallax, the high spatial frequency variations in the locations of off-nadir pixels caused by the Earth's terrain. If effects of the parallax were not included, samples in two data sets acquired with different viewing geometry would be incorrectly located relative to each other by tens of kilometers in areas of high relief.

The solar and lunar angles, satellite angles, and height are for use in VIIRS science processing, such as atmospheric correction. The ground point height and zenith angles are measured with respect to the local normal. The azimuth angles are relative to local geodetic north.

The geolocation and derived products generated for each VIIRS pixel (for ideal Moderate, Ideal Imagery and Day-Night bands) are stored in the following geolocation and data fields:

1. Geodetic latitude
2. Longitude
3. Height above the Earth ellipsoid
4. Satellite zenith angle
5. Satellite azimuth
6. Range to the satellite
7. Solar zenith angle
8. Solar azimuth
9. Lunar zenith angle (DNB only)
10. Lunar azimuth (DNB only)

Lunar phase is computed once per granule and is stored in the DNB's geolocation product granule metadata.

2.2. INSTRUMENT CHARACTERISTICS

Figure 2.2-1 illustrates the design concept for the VIIRS, which is designed and built by Raytheon SBRS. At its heart is a Rotating Telescope Assembly (RTA) that minimizes the

effects of solar impingement and scattered light and a two-sided Half Angle Mirror (HAM) derotator. Calibration is performed onboard using a solar diffuser for short wavelengths and a V-groove blackbody and deep space view for thermal wavelengths. A Solar Diffuser Stability Monitor (SDSM) is also included to track the performance of the solar diffuser. The nominal altitude for an NPOESS satellite is 828 +/- 12 km. The VIIRS scan extends to approximately 56 degrees on each side of nadir.

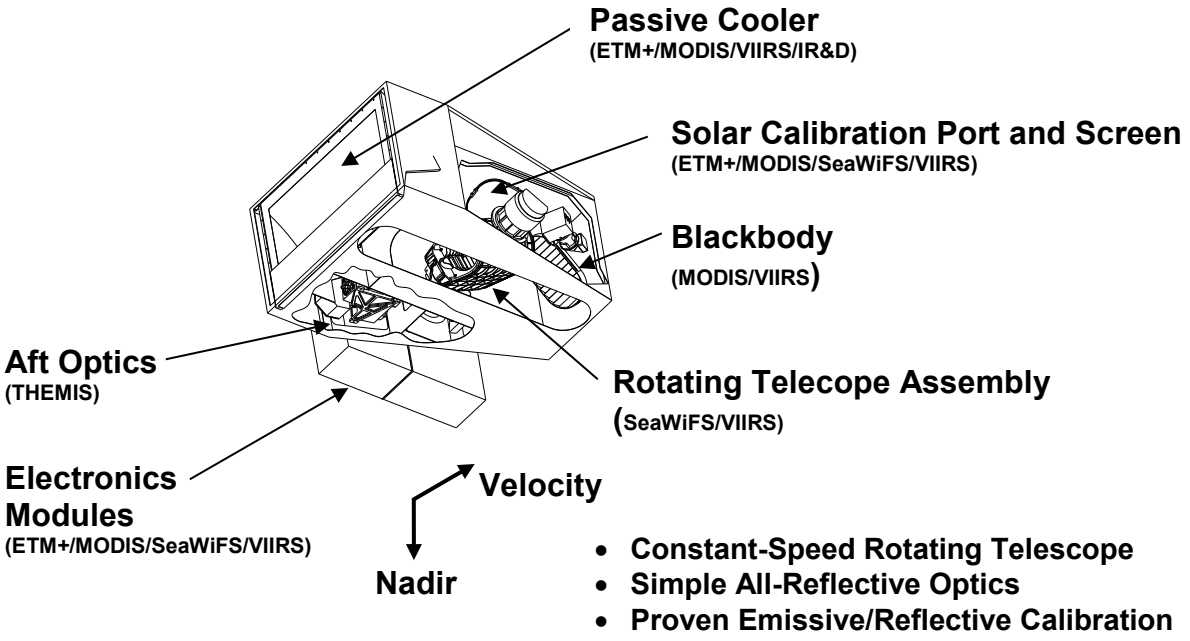

Figure 2-1: Summary of VIIRS Design Concepts and Heritage

Figure 2.2-2 and Figure 2.2-3 present schematic representations of the VIIRS Sensor scan. For most purposes the scan is defined as starting very soon after the HAM turn-around point (HAM Side Change). This is the point in the scan at which the HAM's angular position becomes perpendicular to the rays from the RTA, and thus the optical signal from the RTA stops falling on one side of the HAM and begins to fall on the other side.[1] From this point, the scan proceeds in a counter-clockwise direction to the space view, through the Earth scan (from night to Sun side), to the blackbody, solar diffuser, and then back to the HAM turn-around point. Thus, each scan includes collecting data from each of the calibration sources and the Earth using only one side of the HAM, and each subsequent scan uses alternating sides of the HAM.

[1] The scan start time reported in the VIIRS instrument RDRs is the time at the start of the Earth View segment, not the time of the HAM turn around point

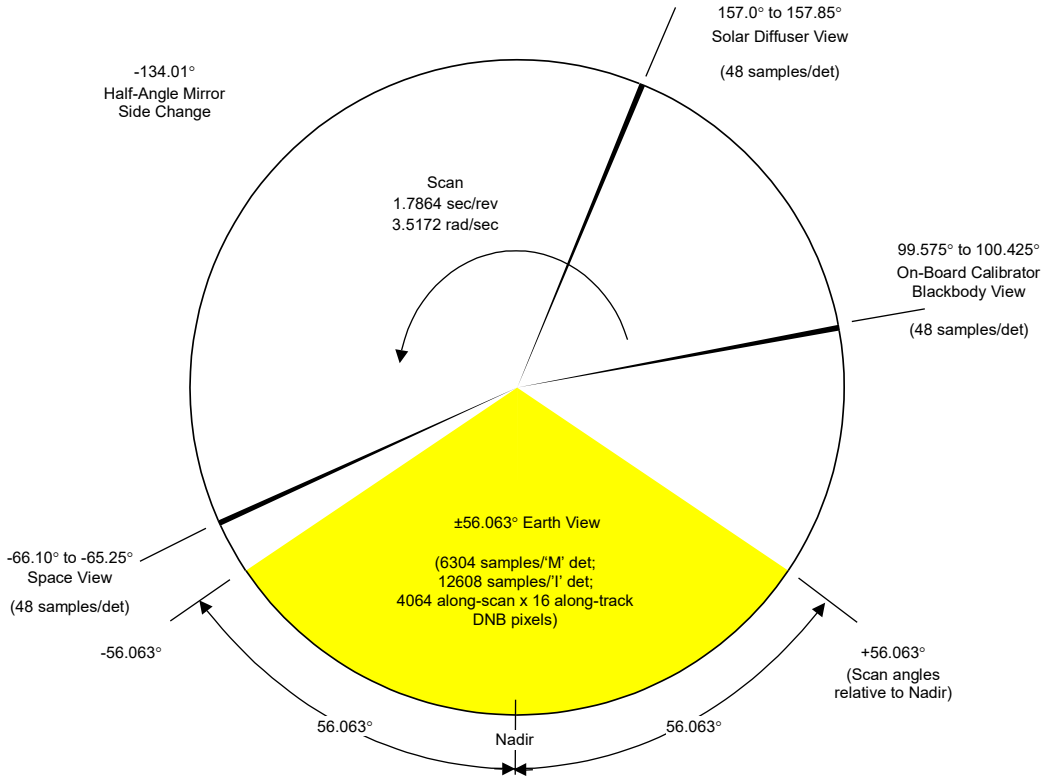

Figure 2-2: VIIRS Scan Pattern[2]

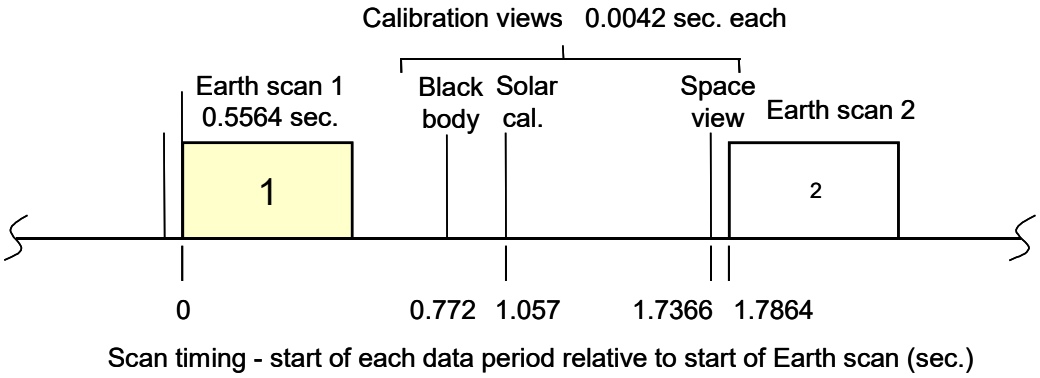

Figure 2-3: Timeline of Typical VIIRS Scan[3]

There are explicit requirements on spatial resolution for the Imagery EDR. Specifically, the horizontal spatial resolution (HSR) of bands used to meet threshold Imagery EDR

[2] The original diagram was taken from SBRS document Y0011672B. This figure has been updated with more recent numbers from SBRS in Sept 2005. Note that these are typical scan values, and may not reflect the final flight configuration.

[3] See Footnote 2.

requirements must be no greater than 400 m at nadir and 800 m at the edge of the scan. This led to the development of a unique scanning approach, which optimizes both spatial resolution and signal-to-noise ratio (SNR) across the scan. The concept is summarized in Figure 2.2-4 for the nested fine resolution imaging ('I') bands. The moderate resolution radiometric bands (i.e. the 'M' bands) follow the same approach at exactly twice the size. The VIIRS 'M' and 'I' band detectors are rectangular, with the smaller dimension projecting along the scan. At nadir, three detector footprints are aggregated[4] to form a single VIIRS "pixel." Moving along the scan away from nadir the detector footprints become larger both along track and along scan due to geometric effects and the curvature of the Earth. The effects are much larger along scan. Using the scan rate assumed in Figure 2.2-2, the aggregation scheme is changed from 3x1 to 2x1 at 31.589 degrees in scan angle. A similar switch from 2x1 to 1x1 aggregation occurs at 44.680 degrees. The pixel growth multiplier is limited to approximately 2 both along track and along scan, compared with a growth factor of 6 along scan which would be realized without the use of the aggregation scheme. The VIIRS DNB is designed with no pixel growth as elements of the DNB Charge Coupled Device (CCD) array are selected to maintain a constant 742 m pixel size across scan.

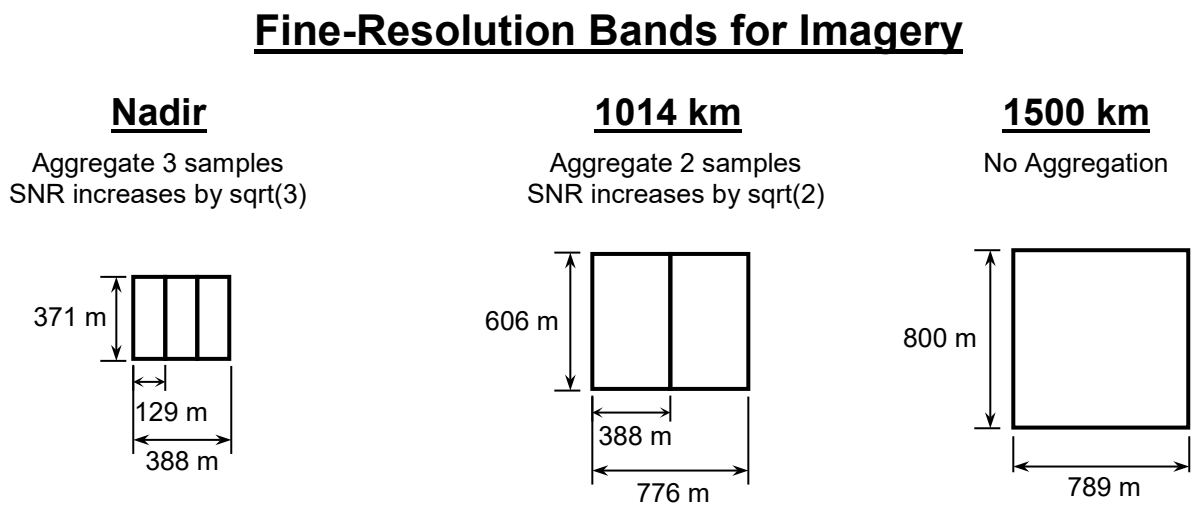

Figure 2-4: VIIRS Detector Along-Scan Aggregation Scheme for Building Pixels (dimensions are approximate)

The VIIRS will provide global coverage from each of the NPOESS orbits. The VIIRS incorporates a cross-track scanner with the spectral channels arranged on four focal planes. The swath width is 3040 km during normal operations. The Instantaneous Field

[4] The along-scan aggregations of dual gain 'M' bands are done during ground processing to match the on-board single gain aggregations. This dual gain sample aggregation must follow radiometric calibration of the individual detector observations.

of View (IFOV) and thus the nadir pixel sizes are variable for the various spectral channels.

Although the basic outline of the VIIRS geolocation algorithm has much in common with other instruments, there are particular characteristics of the VIIRS instrument and science data stream that have special relevance to Earth location. Two of these characteristics (detector geometry and response and scan geometry) are discussed in the following subsections.

2.2.1. Detector Geometry and Detector Response

The spatial characteristics of the detector samples for each band are listed in

Table 2.2-1. Band-to-band registration within the VIIRS electronics produces nominally aligned samples from the 'I' and 'M' bands. A moderate resolution frame (i.e. 16 along-track 'M' pixels assigned to a particular observation time) has nearly the same ground coverage as two imagery resolution frames of 32 along-track pixels per 'I' frame. This band-to-band registration allows geolocation to be performed quite accurately to an "ideal" band target where the "ideal" band can be chosen to be near the VIIRS optical axis as the best representation of all bands of a particular resolution.

Detector misalignments will be measured preflight at Raytheon SBRS and monitored in-flight through image data analysis. The best estimates of the sub-pixel offsets from nominal locations for each detector in each band will be used to compute an average offset per band, and the average offsets will be included in a geolocation parameter file.

The concept of "ideal" band does not apply to the DNB. The DNB is on a separate focal plane assembly (FPA), but shares an optical path with, and is mounted next to (but is thermally isolated from) the Visible/Near Infrared (Vis/NIR) FPA. The VIIRS Electronics Module (EM) aggregates the DNB's sub-pixel detectors so that sixteen along-track pixels are built for each DNB frame. The DNB frame is nearly co-located with the 'M' and 'I' bands at nadir only. Away from nadir sub-pixel aggregations are adjusted to maintain an almost constant 742 m footprint for NPP[5] (see Figure 2.2-5). There are 32 distinct scan position dependent aggregation modes for NPP and J2. The number of aggregation modes used for J1 DNB is less than 32 (see Appendix C). A more detailed discussion of DNB sub-pixel aggregation is in Section 3.3.2.1.3. In developing algorithms for the VIIRS instrument, it is important to understand exactly what the sensor measurements represent. What follows is a basic description of the VIIRS sensor pattern. It describes the response of the instrument on a single pixel basis and shows how individual pixels overlap in the along-scan direction.

[5] J1 DNB footprints at BOS and EOS are different from NPP, see Appendix C.

Table 2.2-1: Spatial Attributes of VIIRS Bands

FPA	Band	Horizontal Sampling Interval (HSI) [km] (Along-Track x Along-Scan)	
		Nadir	End of Scan
Vis/NIR	M1*	0.742 x 0.259	1.60 x 1.58
	M2*	0.742 x 0.259	1.60 x 1.58
	M3*	0.742 x 0.259	1.60 x 1.58
	M4*	0.742 x 0.259	1.60 x 1.58
	I1	0.371 x 0.388	0.80 x 0.789
	M5*	0.742 x 0.259	1.60 x 1.58
	M6	0.742 x 0.776	1.60 x 1.58
	I2	0.371 x 0.388	0.80 x 0.789
	M7*	0.742 x 0.259	1.60 x 1.58
CCD	DNB	0.742 x 0.742	0.742 x 0.742
S/MWIR	M8	0.742 x 0.776	1.60 x 1.58
	M9	0.742 x 0.776	1.60 x 1.58
	I3	0.371 x 0.388	0.80 x 0.789
	M10	0.742 x 0.776	1.60 x 1.58
	M11	0.742 x 0.776	1.60 x 1.58
	I4	0.371 x 0.388	0.80 x 0.789
	M12	0.742 x 0.776	1.60 x 1.58
	M13*	0.742 x 0.259	1.60 x 1.58
LWIR	M14	0.742 x 0.776	1.60 x 1.58
	M15	0.742 x 0.776	1.60 x 1.58
	I5	0.371 x 0.388	0.80 x 0.789
	M16	0.742 x 0.776	1.60 x 1.58
*** Indicates Dual Gain Band – These bands are not along-scan aggregated on-board.**			
Data taken from Raytheon Document PS154640-101, Performance Specification Sensor Specification for VIIRS			

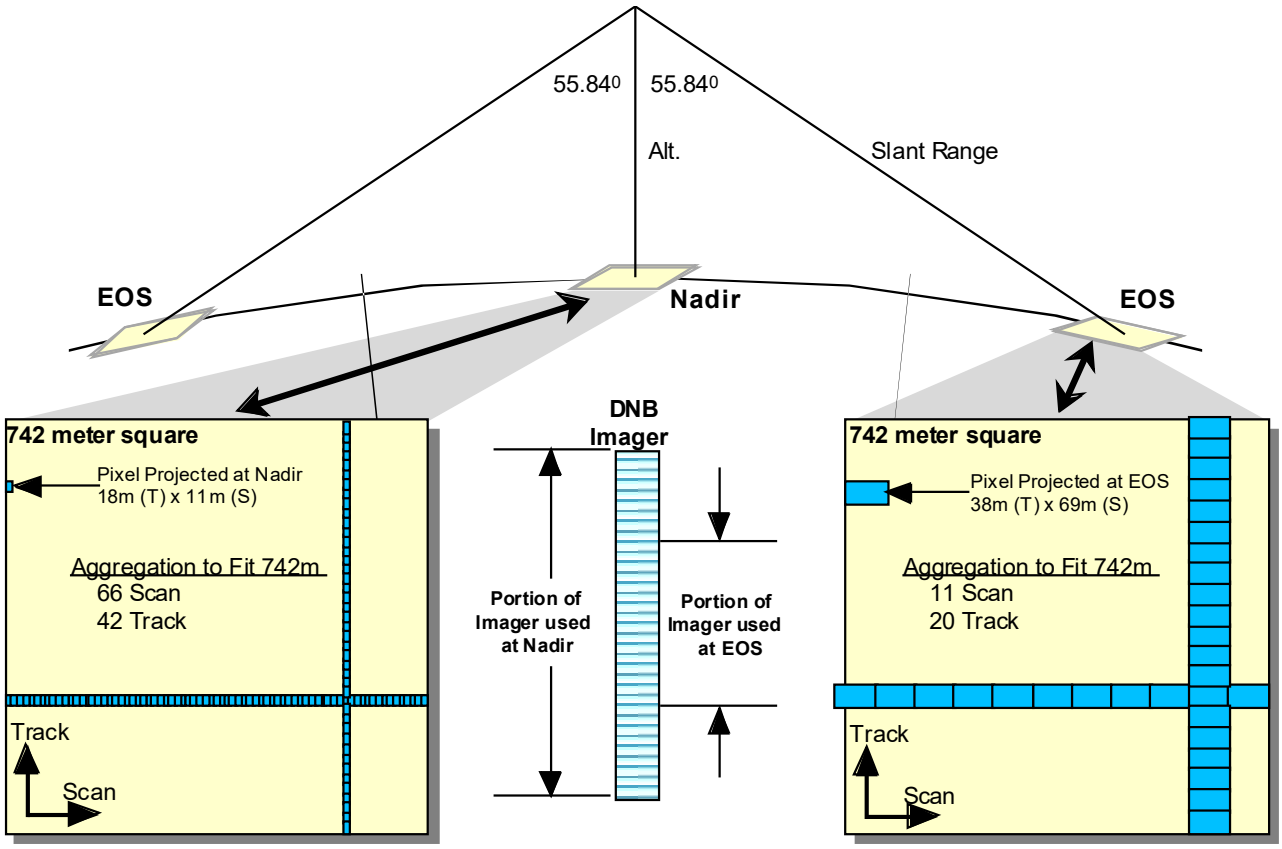

Figure 2-5: VIIRS DNB Sub-pixel Aggregation

2.2.1.1. Spatial Response Function

The VIIRS instrument has detectors that are rectangular in shape and receive a signal at any particular instant of time from an area of the Earth's surface that is approximately 742 m along-track by 259 m across-track (moderate resolution bands - all dimensions are for nadir pixels). These asymmetrical detectors are used to compensate for the asymmetrical effects of pixel growth at high scan angles. The 742 m by 259 m nadir footprint grows to approximately 1600 m by 1579 m at the end of scan. In order to maintain more symmetrical pixel dimensions at all scan angles a sample aggregation scheme is used. At scan angles within +/- 31.589 degrees of nadir (i.e. samples 1377 through 4928[6]) groups of three samples are aggregated to form a single output pixel with effective dimensions of 742 m by 776 m at nadir. At scan angles between 31.589 degrees and 44.680 degrees on either side of nadir (i.e. samples 641 through 1376 and 4929 through 5664) a sample aggregation factor of two is used, transitioning to a factor of one beyond

[6] The convention used is that the first frame of the Earth view scan is frame 1 not frame 0. Also, scan angles derived for typical scan rate assumed in Figure 2.2-2.

+/- 44.680 degrees.

There is a temptation to think that the detector dwells over a single location until a sample is taken and then steps to the next sample. This would produce a rectangular response weighting function as shown in Figure 2.2-6.

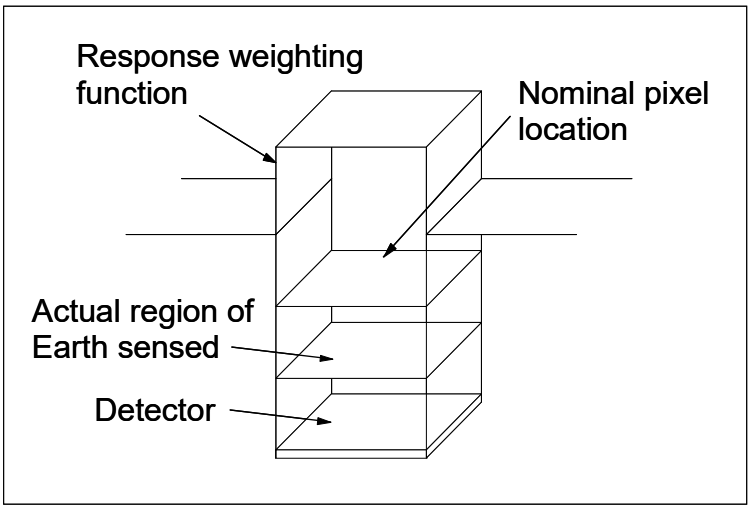

Figure 2-6: Rectangular Response Weighting Function

However, this is not the case; instead, VIIRS senses the Earth using a telescope that rotates at a constant speed. A single sample consists of the integrated signal received at the detector during the entire sampling interval. This sampling interval is typically the amount of time it takes the projected image of the detector on the ground to move sideways (along-scan) one sample, 88.259 μsec (dwell time) for the moderate resolution bands. The small amount of time at the end of the sampling interval needed to read out the integrated information from the detector and reset the detector is ignored in this discussion. The degree to which the actual detector dwell time is less than the sampling interval will cause this triangular pattern to have a flattened top, giving it a trapezoidal shape. Pixel aggregation alters the effective response function in a similar way. This effect is shown in Figure 2.2-7.

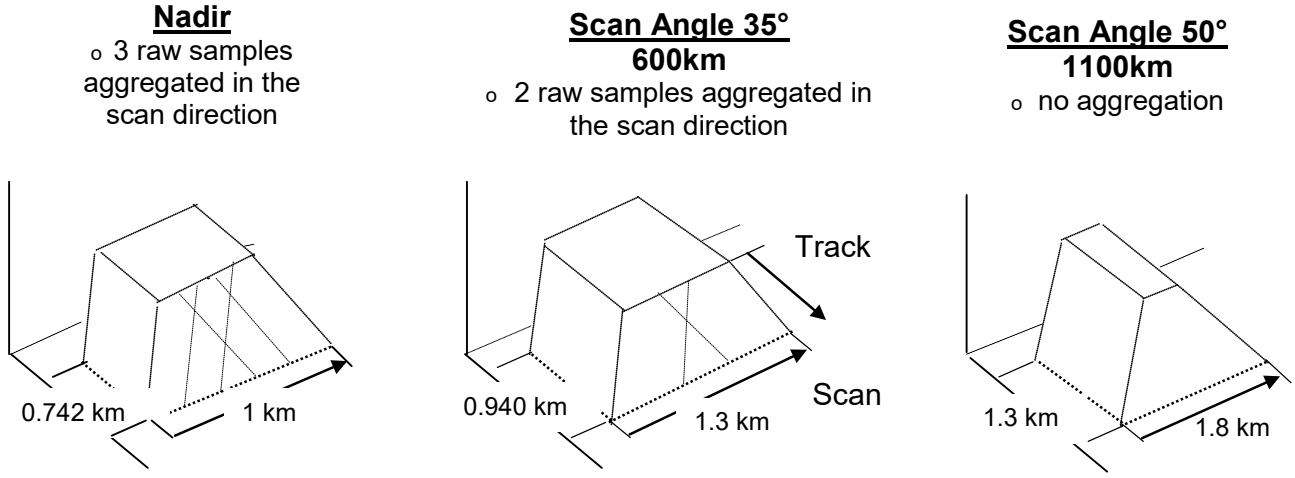

Figure 2-7: VIIRS Spatial Response Functions

Although what actually happens is that the ground image travels across the detector, it is common to speak as if the pixel moves across the surface of the Earth, which is portrayed in this description. So for a detector with a perfect rectangular response, the area actually sensed is twice as long as the nominal detector pattern and the effective time weighted response is triangular as shown in Figure 2.2-8.

Of course, there is not just one sample along a scan line. As soon as the time for one sample ends a new sample is begun. The result is a series of triangular weighted pixels as shown in Figure 2.2-9 and Figure 2.2-10 (for simplicity the remaining figures are done in two dimensions).

Figure 2.2-9 shows that nominal pixel P2 actually obtains signal from the right hand side of nominal pixel P1 and from the left hand side of nominal pixel P3. It also shows that a small hot spot in the exact center of region P1 would have all of its response in P1, but the same hot spot, such as a fire, located at the right hand edge of P1 would have half of its response shown in P1 and half in P2. Although we speak of nominal 259 m pixels, the signal is obtained from a strip that is 518 m along-scan and 742 km along-track at nadir. In fact, as shown in Figure 2.2-10, for a uniform scene of constant brightness, 12.5% of the signal is collected from each side and 75% of the signal is collected from the nominal pixel itself.

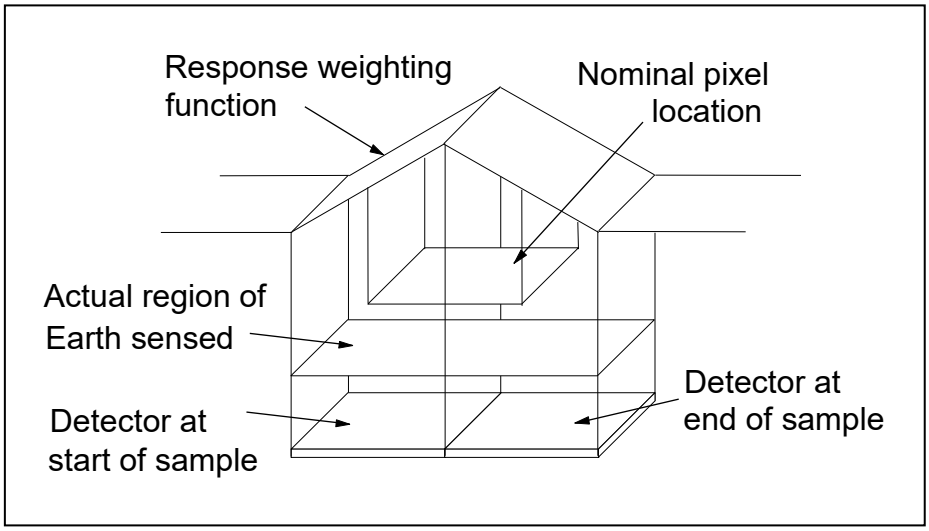

Figure 2-8: Triangular Response Function from the Effective Time Weighting[7]

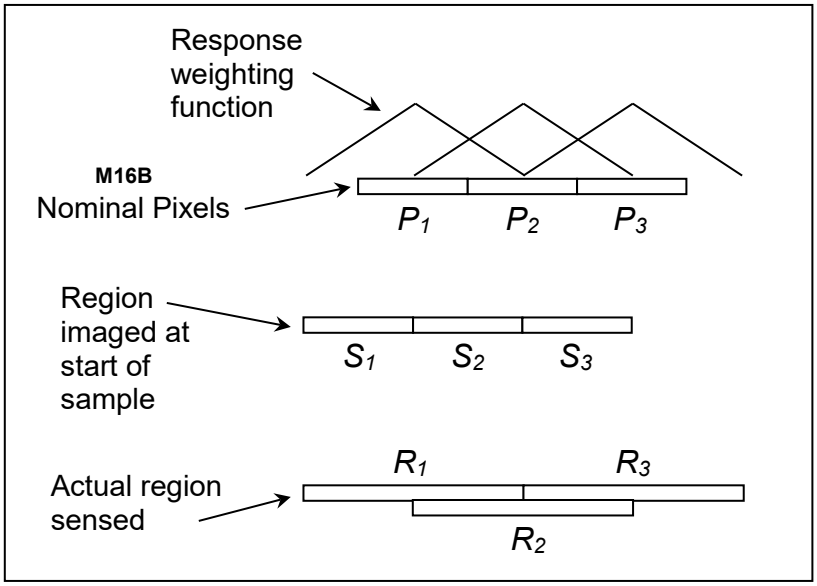

Figure 2-9: Series of Triangular Weighted Pixels (see Footnote 7)

[7] Note as discussed in the text, the VIIRS resonse is trapezoidal vs. triangular.

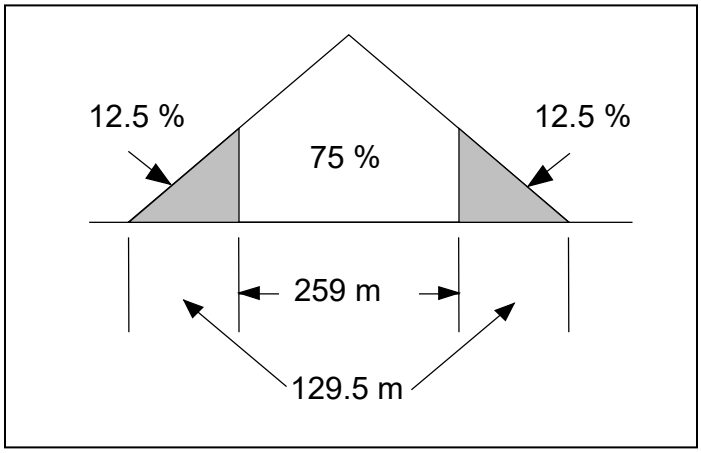

Figure 2-10: 75% of Signal is Collected from Nominal Pixel (see Footnote 7)

2.2.1.2. Location of Pixel

The location of a pixel is associated with the center of the spatial response function for an ideal moderate resolution band detector. From Figure 2.2-9 it can be seen that the peak of the response function corresponds to the location of the detector trailing edge at the end of the sampling interval. Each frame of VIIRS data contains all of the observations from all of the bands corresponding to sixteen moderate resolution band ground locations along-track. There are thus sixteen pixels associated with each data frame.

The effective pixel center must be adjusted to account for along-scan aggregation. In the three-sample aggregation region the center of the pixel is associated with the location of the middle of the three aggregated samples. In the two-sample aggregation region the pixel location is associated with the average of the two aggregated sample locations.

2.2.2. Scan Geometry

The second characteristic of the VIIRS instrument of particular importance for Earth location is the behavior of the cross-track RTA. For the nominal scan rate (see Figure 2.2-2), the RTA sweeps out a 112.13° Earth field of view in each scan, effectively moving the instrument's sixteen pixels over a swath of the Earth approximately 11.9 km wide at nadir. This scan width increases to 25.9 km at the end of scan due to the panoramic "bow tie" effect (Figure 2.2-11). This effect leads to scan-to-scan overlap at scan angles greater than approximately 19 degrees (Figure 2.2-12). On the other hand, the scan gap at nadir is nominally zero.

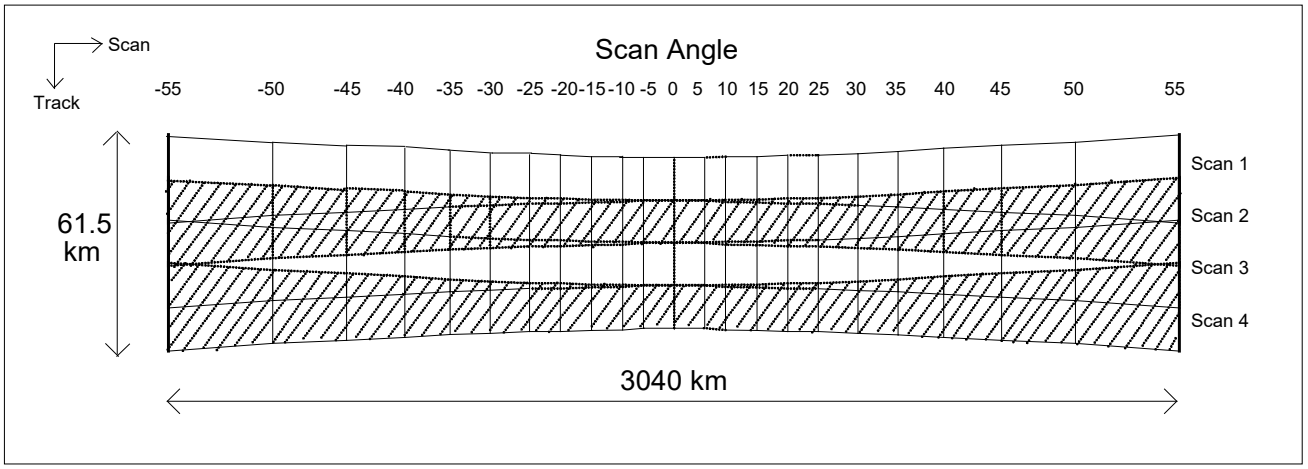

Figure 2-11: Panoramic Bow Tie Effect

A feature of the VIIRS flight software that trims the 'M' band and 'I' band data in the along-track direction as a function of along-scan aggregation zone will be enabled. This will result in some of the samples in the overlap area to be excluded from the data that are delivered to the ground. The *VIIRS Command, Telemetry, Science and Engineering Data Description [EDD154640-101]* describes this "bow-tie deletion" feature, which is illustrated in Figure 2.2-13.

The RTA (and HAM) along-scan motion is measured and down-linked in the instrument data stream. These measurements are explicitly used by the Earth location algorithm to determine the instrument pointing. RTA and HAM motion linearity is not assumed.

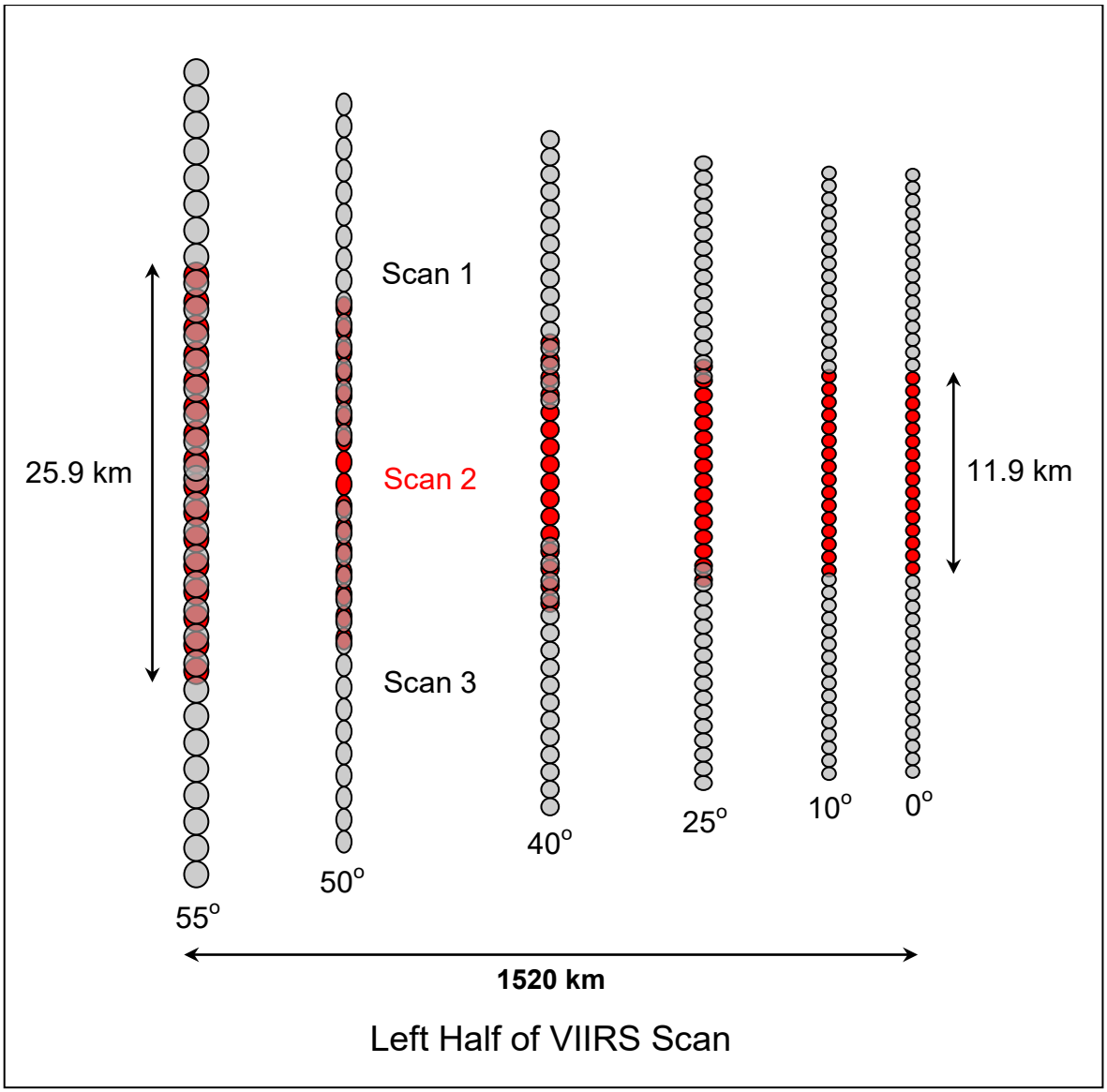

Figure 2-12: Pixel Size Growth and Overlap within a Scan

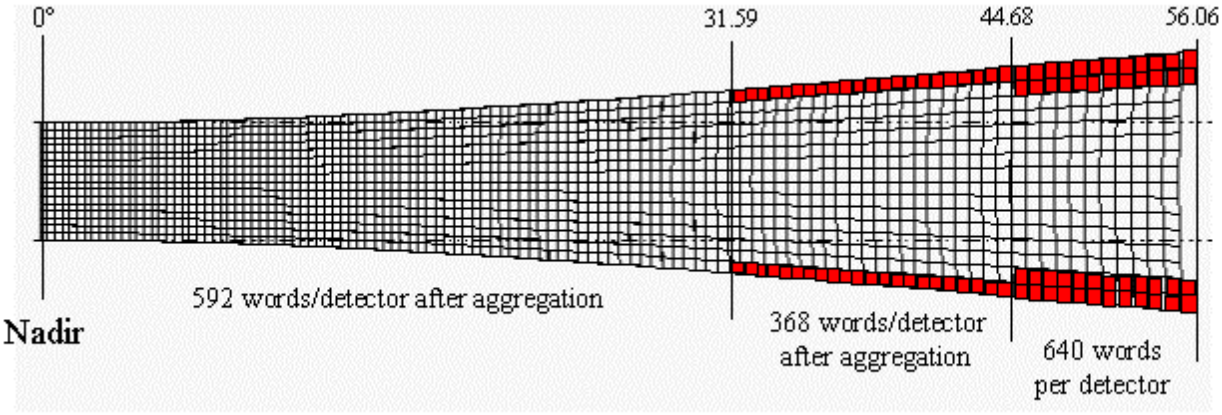

Figure 2-13: VIIRS "Bow-tie Deletion"[8]

2.3. RETRIEVAL STRATEGY

The support data accompanying the imagery will be used to compute Earth location information for each VIIRS pixel. The core of this procedure uses models of the VIIRS sensor and NPOESS spacecraft to construct line-of-sight vectors. The timing information associated with these vectors is then used to intersect them with the terrain surface of the rotating Earth. The geodetic position of this terrain intersection point or the earth ellipsoid point is stored in the VIIRS product geolocation fields. The terrain intersection procedure is described in Section 3.3.2.2.2.

Georetrieval begins with assembling the S/C auxiliary and instrument engineering data that are required. These data include time-tagged S/C position, velocity, and attitude, scan start times, and RTA and HAM encoder data (encoder start values and encoder timestamps). S/C attitude may be converted from quaternion to Euler error angles (i.e. roll, pitch, and yaw error) or may be used directly. Band type specific geolocation then proceeds on a frame-by-frame basis. The steps in the process are as follows:

1. Determine frame time
2. Interpolate S/C position to the frame time using S/C velocity reports
3. Determine scan angle at frame time using interpolated RTA and HAM encoder data
4. Determine each pixel's line of sight by transforming from FPA coordinates to instrument coordinates
5. Convert each pixel's line of sight to S/C coordinates using a transformation matrix that reflects actual instrument mounting (nominally the instrument coordinates will be co-aligned with the S/C coordinates)
6. Determine roll, pitch, and yaw from S/C attitude data at the frame time
7. Apply an optional thermal correction to roll, pitch, and yaw

[8] Red-filled pxels are not sent to the ground.

8. Determine each pixel's line of sight in orbital coordinates by applying effective roll, pitch, and yaw to the instrument centered line of sight
9. Intersect each pixel's line of sight with the WGS84 ellipsoid and output geodetic latitude and longitude if terrain intersection is not to be done
10. If terrain correction is to be performed then determine each pixel's line of sight intersection with the geoid or terrain using the Digital Elevation Model (DEM) with the Science Data Processing Toolkit (SDPTK) and output terrain corrected geodetic latitude and longitude
11. Compute and output derived geolocation products (i.e. solar, sensor, and lunar [DNB only] azimuth and zenith for each pixel in the frame

Lunar phase is computed once per granule if processing the DNB.

[This page is intentionally blank]

3. ALGORITHM DESCRIPTION

3.1. PROCESSING OUTLINE

The geolocation process first loads and quality checks the supporting engineering and spacecraft auxiliary data from each Verified VIIRS RDR. These validated support data are then used to construct dynamic models of the VIIRS instrument and NPOESS platform. These models make use of the time and S/C position and velocity and S/C attitude data as well as the instrument telemetry (e.g., RTA and HAM encoder data) contained in the NPOESS S/C ephemeris and attitude data and VIIRS engineering data. Once constructed, these models are used to generate line-of-sight vectors for each VIIRS pixel, propagate these vectors through the instrument optics, and orient the vectors in inertial space. Each inertial line-of-sight is then intersected with the rotating WGS84 ellipsoid and Earth's surface, taking into account variations in the Earth's terrain surface by using a digital elevation model if terrain correction is desired.

3.2. ALGORITHM INPUT

The VIIRS geolocation algorithm uses the spacecraft and instrument engineering data contained in the Verified VIIRS RDRs along with key external support data sets to generate the geolocation and related data fields for each VIIRS pixel. These input data sets are divided into those "internal" VIIRS data that are a part of each VIIRS data set and those ancillary items that must be assembled and maintained on the processing system, independent of the VIIRS data stream.

3.2.1. VIIRS Data

The VIIRS observation data are not required to perform the routine geolocation processing. Rather it is the engineering data and the S/C ephemeris and attitude data, which are downlinked separately and merged with the VIIRS data prior to geolocation, that are of primary importance. In particular, the S/C ephemeris and attitude data are used to construct a model of the platform position, velocity, and orientation as a function of time. The VIIRS RTA and HAM encoder data contained in the instrument telemetry are used to construct models of the RTA and HAM rotation as functions of time. The scan timing information is used to relate the VIIRS spatial elements to the models of both the dynamic components of the instrument (RTA and HAM) and the S/C. Details about the downlinked VIIRS data can be found in the *VIIRS Command, Telemetry, Science [EDD154640-101]*. The S/C ephemeris and attitude data are described in the NPOESS *Operations Concept (OPSCON) Chapter 5 – Volume 6, Scenarios SYS-020-040 and SYS-020-041, Auxiliary Data: Spacecraft Ephemeris and Attitude [NGST D31400-06].*

3.2.2. Non-VIIRS Data

Ancillary geoid height and digital elevation data are used to ascertain the Earth's ocean and terrain surface. Instrument constants describe the internal geometry of the VIIRS instrument. Ground control point (GCPs) are used to validate the accuracy of the Earth location data during post-processing analysis.

The VIIRS Earth location algorithm was developed using the Digital Elevation Model (DEM) that is currently in use for MODIS geolocation, i.e. that which is supplied with the Earth Observing System Data and Information System (EOSDIS) Core System (ECS) Science Data Processing Toolkit (SDPTK). This DEM was derived from the best available 30 arc-second resolution global database of terrain information and is supplied in HDF-EOS format by the United States Geological Survey's Earth Resources Observation System (EROS) Data Center (EDC). This DEM is considered constant during processing although it is understood that the values of these parameters may change with time, or may be updated as better knowledge of their true values becomes available. The current VIIRS Geolocation algorithm uses the Shuttle Radar Topography Mission (SRTM) terrain data, Version 2.

The SDPTK time conversion functions require two additional ancillary files that need to be updated on a regular basis. These are the Leap Seconds File (i.e. leapsec.dat) and the Earth Rotations File (i.e. utcpole.dat). Data to update each of these files is available from the United States Naval Observatory (USNO).

The first type of instrument constants includes the focal plane, band, and detector locations. These constants are stored in the VIIRS Geolocation Parameter File as a table of locations to generate corrections applicable to each detector (channel) in a spatial element. The second type may be classified as optics parameters. They include the focal lengths of the aft optics, the relationship between the optical axis and instrument alignment axes, angles that describe the HAM surfaces, the relationship between the HAM and telescope assemblies and the instrument alignment axis, and the RTA angle as a function of encoder number. The aft focal lengths are needed to generate a viewing vector from a location on the focal plane. The other optics parameters are needed to determine the orientation of the normal to the HAM surface and the orientation of the RTA at a given sample time. Once this is known, the viewing vector is reflected off the HAM and through the RTA to produce an object space viewing vector. The third type of instrument constant required is the instrument-to-spacecraft alignment matrix. This matrix describes the spatial relationship between the VIIRS instrument alignment axes and the NPOESS spacecraft. This relationship may have a time varying component that can be detected and modeled over time, but will be assumed to be static at launch.

The GCPs used to validate the VIIRS Earth location algorithm's performance are image windows containing well defined features with known ground locations. The MODIS Ground Control Point Library will be a good source for these control points. In addition to the original MODIS control point library, a new set of libraries derived from Landsat 7 Enhanced Thematic Mapper Plus (ETM+) data will be added with the improved absolute geodetic accuracy of the ETM+ data. The current VIIRS operational concept includes the use of control with a subset of VIIRS data products only. This is based on the idea that it will be more effective to concentrate the acquisition of high-quality ground control along a few orbits so that one product in ten, for example, has abundant control rather than all having minimal control. Concentrating high quality control throughout a few orbits allows both short-term and long-term variations in parameter biases to be detected. Additional ground control will be used throughout the rest of the world to verify the accuracy of the Earth location parameters globally.

3.3. THEORETICAL DESCRIPTION OF GEOLOCATION

The underlying theory and mathematical development of the VIIRS geolocation algorithm is provided in Sections 3.3.1 and 3.3.2. Implementation and operational considerations are addressed in Section 3.5.

3.3.1. Physics of the Problem

The supporting theoretical concepts and mathematics of the VIIRS geolocation algorithm are presented in the following subsections. This section presents a review of the VIIRS viewing geometry to put the subsequent discussion in context. This section then addresses the coordinate systems used by the algorithm and the relationships between them, citing references where appropriate.

3.3.1.1. Viewing Geometry Overview

The VIIRS ‘M’ and ‘I’ band detectors are aligned in parallel rows on three focal plane assemblies. The aft optics assembly illuminates the detectors on each of the three focal planes. The detector placement geometry and aft optics focal length define the internal geometry of each focal plane relative to the instrument optical axis. Each band consists of a row of either 16 (‘M’ bands) or 32 (‘I’ bands) detectors. The rows of detectors from each band are separated on the focal plane in the along-scan (cross-track) direction. The different bands are aligned into corresponding samples by delaying the observations from each band to account for the slight along-scan motion needed to view the same target point. In the discussion to follow, the angles reported are computed based on a nominal scan rate of 3.5172 radians per second, and no timing delays are assumed. It should be noted that the scan angles are dependent on the scan rate since the detector sampling period and number of samples are held constant. The instrument's 112.126-degree Earth view is swept over the three focal planes by the combined motions of a double-sided rotating HAM and a rotating telescope assembly (RTA). The RTA rotates at a rate of 33.587 revolutions per minute with the HAM rotating at half this rate to illuminate the aft optics/focal plane assemblies. The nominal VIIRS scan period is 1.7864 seconds of which approximately 0.5564 seconds is devoted to the Earth view portion of the scan. Significant spacecraft motion and Earth rotation take place during this scan period. The detector sampling period is 88.259 microseconds with the ‘M’ bands sampled once per period and the ‘I’ bands sampled twice per period. The sampling strategy also includes along-scan sample aggregation as a function of scan angle.

The 112.126-degree wide instrument field of view sweeps out a ground swath approximately 3040 km long during the 0.5564 seconds Earth view period. The wide ground swath made possible by the ±56.063 degree viewing angles exhibits significant Earth curvature effects. The apparent Earth zenith angle of a LOS at a 55-degree scan angle is increased to approximately 65 deg by Earth curvature. This effect, along with the increasing target range, also contributes to the growth of the projected ground spatial element as a function of scan angle. Asymmetrical detectors are used with a variable pixel aggregation scheme in the cross-track direction to moderate this pixel growth and provide a more uniform ground sample size at all scan angles. The along-scan aggregation factor ranges from 3:1 at nadir to 1:1 at the maximum 56.063-degree scan

angle. Figure 3.3-1 is a graph depicting the growth of the spatial element ground field of view with scan angle. The discontinuities in this curve identify the aggregation factor transition points from 3:1 aggregation to 2:1 aggregation at +/- 31.589 degrees and from 2:1 aggregation to 1:1 at +/- 44.680 degrees. The ground dimensions of 'M' band pixels range from 0.776 km along-scan by 0.742 km along-track at nadir to 1.6 km along-scan by 1.6 km along-track at a 56.063-degree scan angle. The center of the pixel (nominal detector) will be used when computing lines of sight. It should be noted that there is a very small distance between the pixel center and the centroid of the ground projected field of view for off-nadir pixels. This distance is less than 2 m near the edges of the scan.

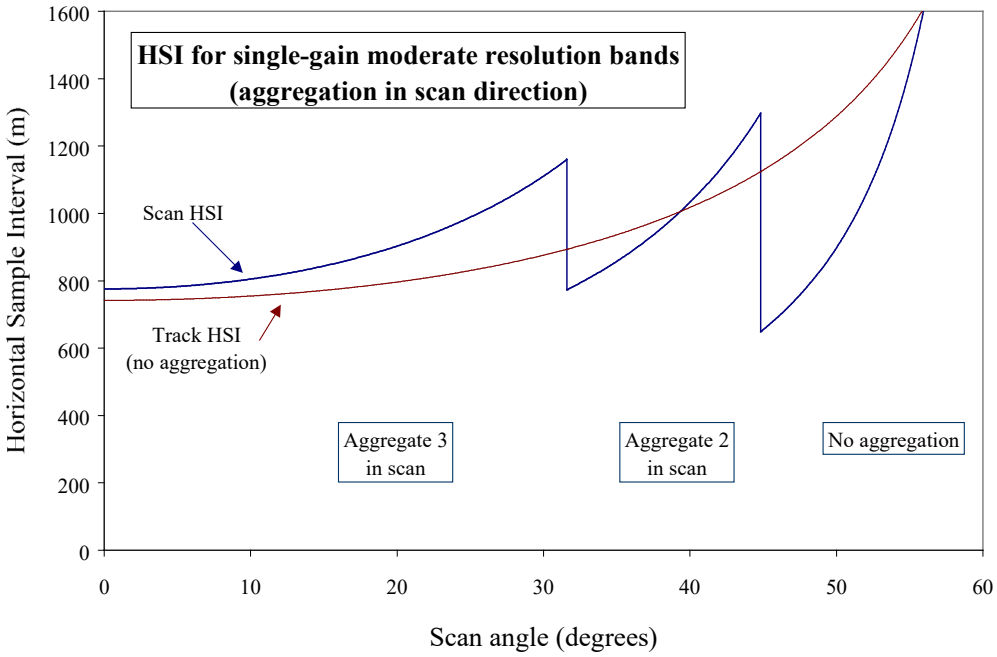

Figure 3-1: Growth of Spatial Element Ground Field of View

3.3.1.2. Coordinate Systems

There are ten basic coordinate systems used by the VIIRS geolocation algorithm. These coordinate systems are defined here and referred to frequently in the remainder of this document. They are presented in the logical order in which a viewing vector and sample time would be transformed into a geodetic position. The orientation of the focal plane, aft optics, HAM, RTA, and instrument coordinate system's axes chosen for this model are somewhat arbitrary. It should also be noted that the origin of the instrument coordinate system does not coincide with the origin of the spacecraft (which is located at the spacecraft center of mass). This offset will be ignored in the rest of the document.

3.3.1.2.1. Focal Plane Coordinate System

The Z-axis of the focal plane coordinate system coincides with the aft optics Z-axis. A detailed layout of each band and its detectors is shown in Figure 3.3-2A and Figure 3.3-2B. The X-axis of the focal plane corresponds to the scan direction. The Y-axis corresponds to the negative direction of the ground track. For example, the X-coordinates of the detectors in M5 are all negative as they are placed down scan of the optical axis located near the center of the FPA, while all detectors in M2 have positive X-coordinates as they are up scan from the optical axis. Note that a detector numbering convention is shown that has the first detector as the one that is furthest in the track direction. This is opposite to the array indexing scheme that is used when building VIIRS Sensor Data Records. Additional details concerning the focal plane coordinates are in Section 3.3.2.1.1.

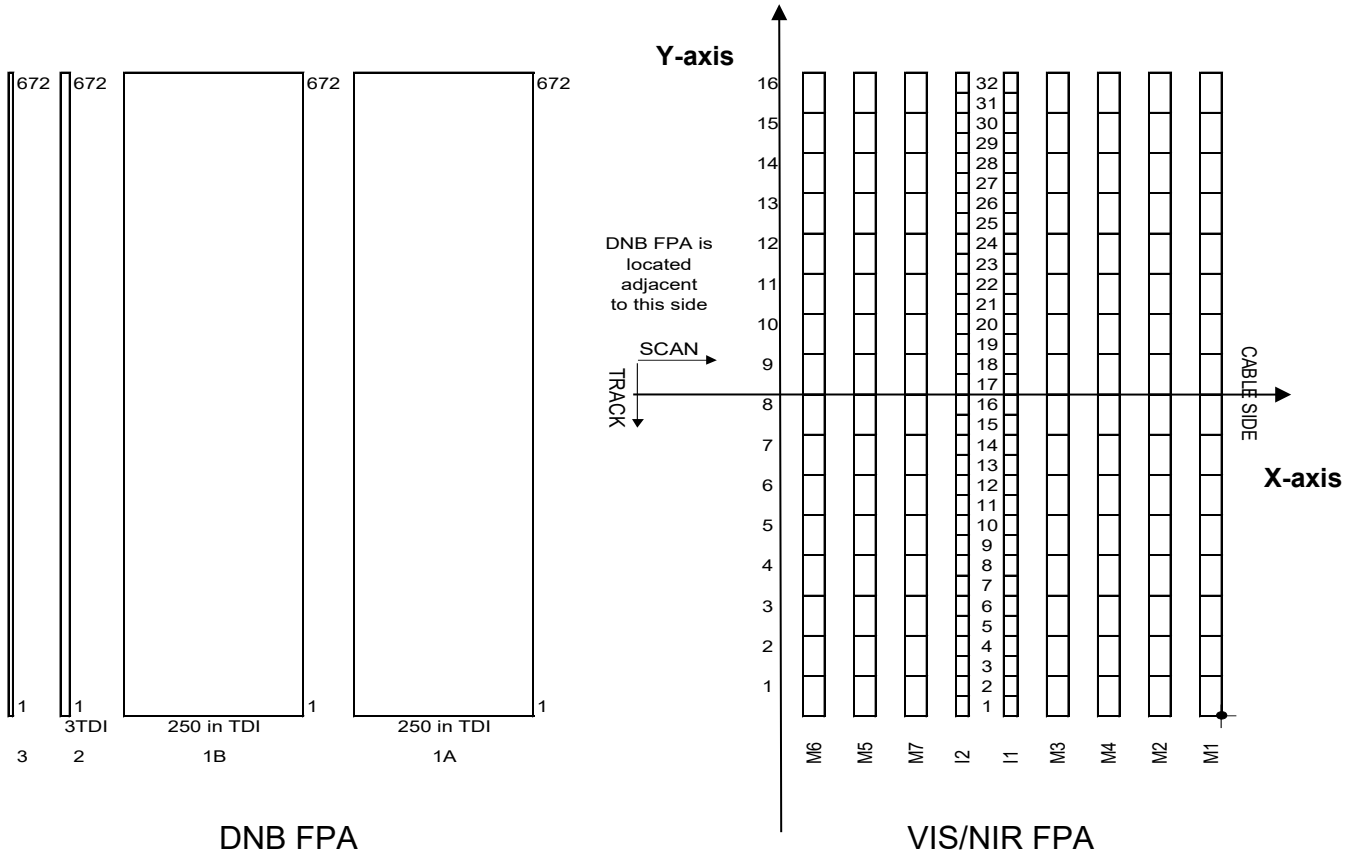

Figure 3-2A: CCD and Detector Layout (DNB and VIS/NIR)

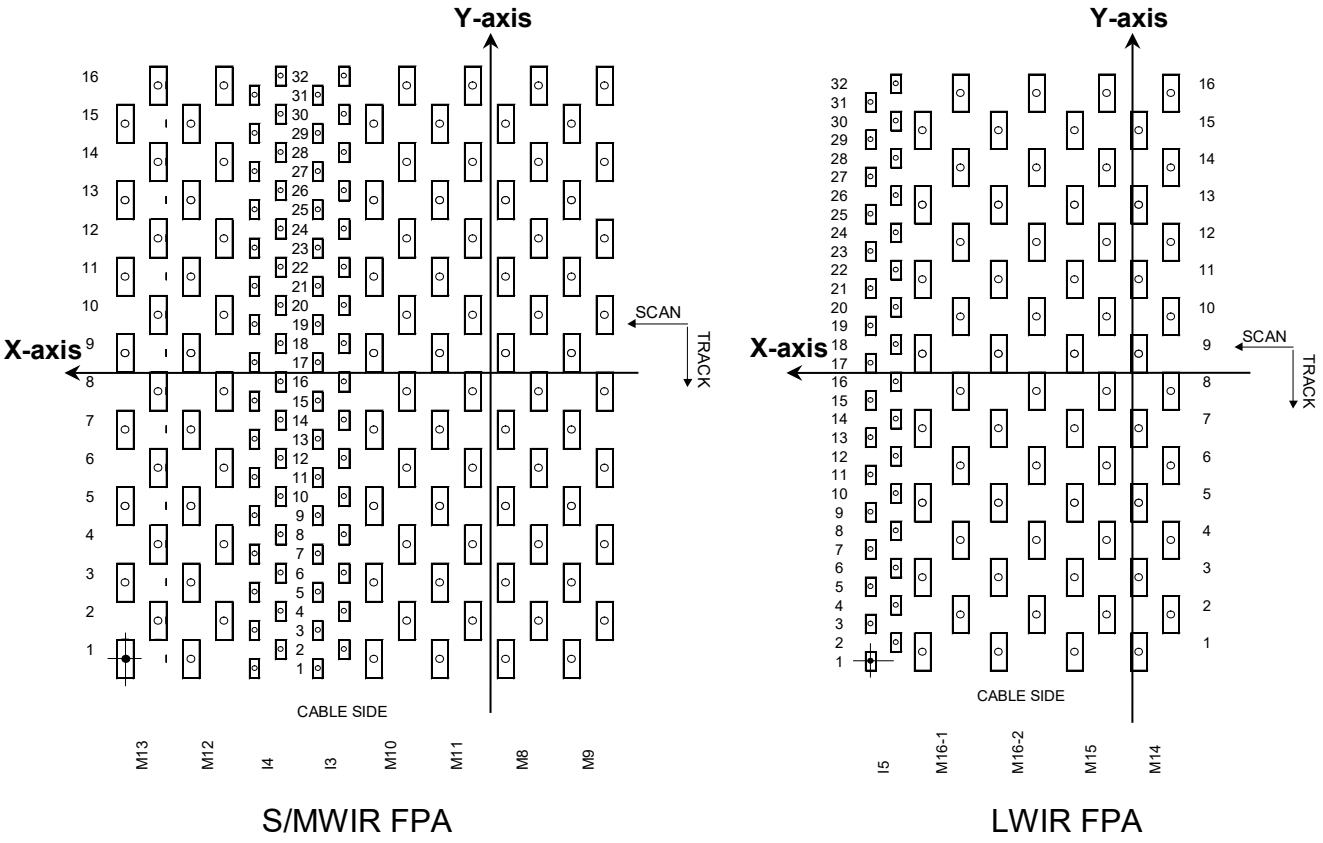

Figure 3.3-2B: CCD and Detector Layout (S/MWIR and LWIR)

3.3.1.2.2. Aft Optics Coordinate System

The aft optics coordinate system is the place where the image space viewing vector is generated for either individual detector samples or for the ideal spatial elements. The origin is where an ideal optical axis intersects the focal planes (Figure 3.3-3 where the focal plane rotation is shown). The Aft Optics coordinate system is defined with the positive Z-axis pointed at the center of the HAM, such that the Z-axis is approximately parallel to the RTA optical axis after reflection off the HAM. The X-axis is perpendicular to the HAM's axis of rotation, where the positive direction is toward the band on the leading edge of the focal plane. The Y-axis is in the focal plane's negative along-track direction after a reflection off the HAM, with the positive direction toward the highest detector number.

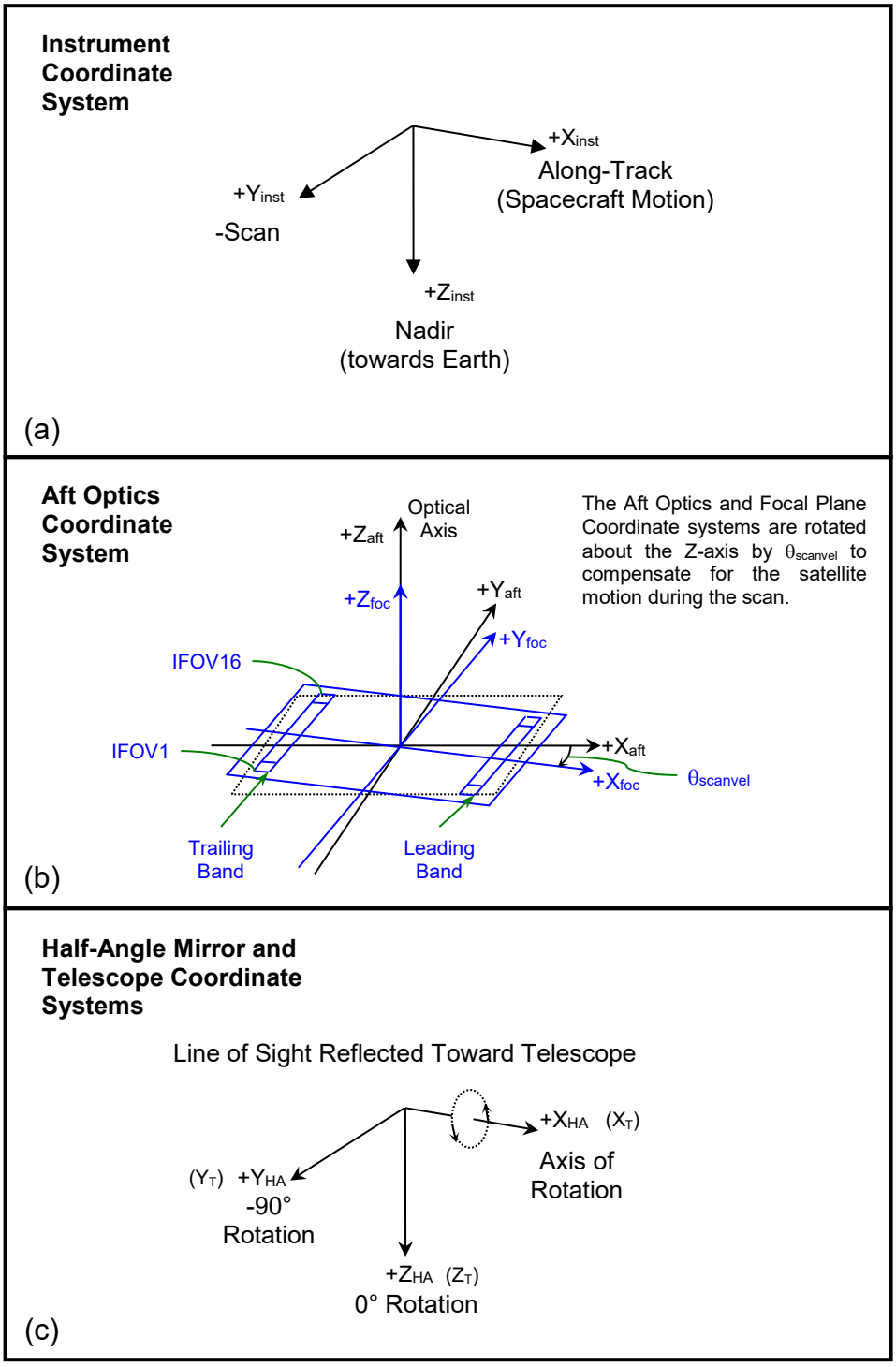

Figure 3-3: Instrument, Aft Optics and Half Angle Mirror Coordinate Systems' Relative Orientation

3.3.1.2.3. Half Angle Mirror Coordinate System

The HAM model is defined in the HAM coordinate system. It is nominally aligned with the instrument coordinate system. This coordinate system is defined (Figure 3.3-3) so that the X axis is along the axis of rotation of the HAM, which is parallel to the RTA axis of rotation which is also parallel to the along-track direction, and the Z axis is downward toward the Earth (geodetic nadir if there is no attitude error). The Y axis completes the right-handed coordinate system.

When the normal of HAM side 1 is parallel to the Z-axis, the mirror is defined to have a zero-rotation angle (ignoring the small mirror wedge angles and axis error). When the mirror is rotated to either 23 or 203 degrees (these angles are measured from the Z-axis to the HAM side 1 normal), the LOS along the aft optics' optical axis is reflected by the mirror directly into the RTA, which in turn redirects it straight down toward nadir. As the RTA rotates about the scan axis the HAM must rotate at exactly half the RTA rate so that the doubling effect of reflection of the LOS off the HAM exactly compensates for the RTA rotation. A view of the HAM, RTA, and instrument coordinate systems from the positive X instrument axis is illustrated in Figure 3.3-4 to show their relationship.

It should be noted that the actual locations of the focal planes vary. However, all the focal planes can be symbolized and placed at one location as depicted in Figure 3.3-4. The light leaving the HAM will be redirected by a mirror to the aft optics to reach a focal plane.

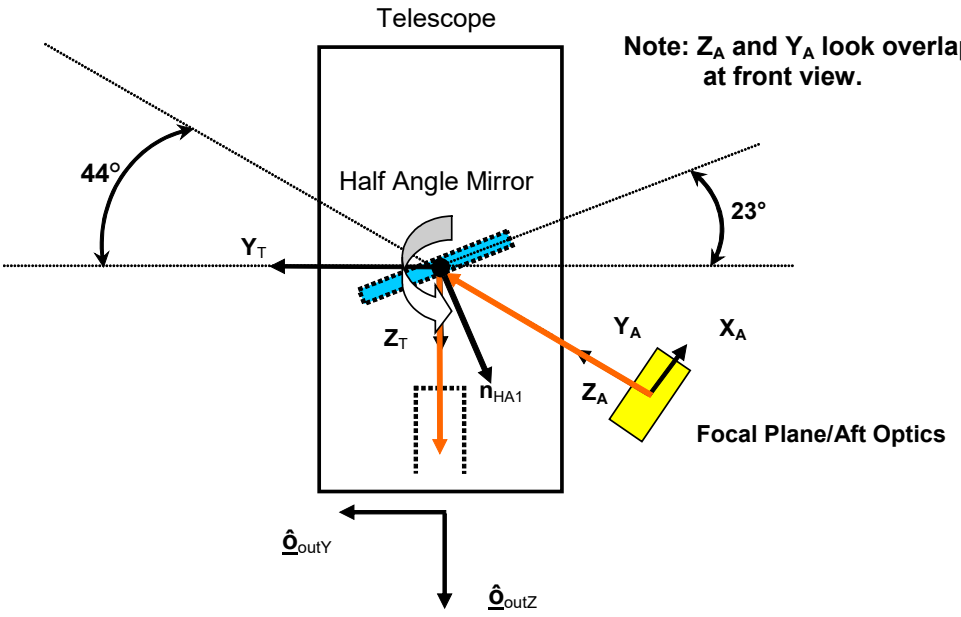

Figure 3-4: Off-Nadir View, Half Angle Mirror Rotation, Telescope Rotation in Instrument Coordinate System

3.3.1.2.4. Solar Diffuser Coordinate System

The solar diffuser coordinate system is defined such that the Z axis is normal to the solar diffuser surface, where the positive Z axis points away from the surface. The X and Y

coordinates define the plane of the solar diffuser. The transformation from the Instrument coordinate system to the Solar Diffuser system is described in Section 3.3.1.3.4.

3.3.1.2.5. Telescope Coordinate System

The telescope coordinate system is nominally aligned with the instrument coordinate system with the X-axis being the axis of RTA rotation during scanning. The Z-axis is aligned to the RTA axis at a 0-degree scan angle (nadir pointing), which nominally makes the Z-axis point toward the Earth (positive toward the Earth). The Y-axis is the cross-product of the X-axis and the Z-axis. The nominal telescope coordinate system is illustrated in Figure 3.3-5. The RTA transforms line-of-sight vectors from the entrance aperture (facing the aft optics) to the exit aperture (facing the Earth), applying a 4X (de)magnification factor along the way. A set of basis vectors are constructed for the entrance aperture, $(\hat{o}_{inX}, \hat{o}_{inY}, \hat{o}_{inZ})$, and exit aperture, $(\hat{o}_{outX}, \hat{o}_{outY}, \hat{o}_{outZ})$, as shown in Figure 3.3-6. These basis vectors are defined such that the Z-axis vector corresponds to the RTA optical axis for each set. These basis vectors can be used to model the RTA operation by mapping LOS vectors from the HAM onto the entrance basis vectors, applying the magnification scale factor to the aperture X and Y axes, and reconstructing the LOS at the exit aperture using the exit basis vectors. These aperture basis vectors are constructed in the telescope coordinate system so the incoming LOS vector must first be transformed from the instrument coordinate system to the telescope coordinate system. Similarly, the outgoing LOS is transformed from the telescope coordinate system to the instrument coordinate system.

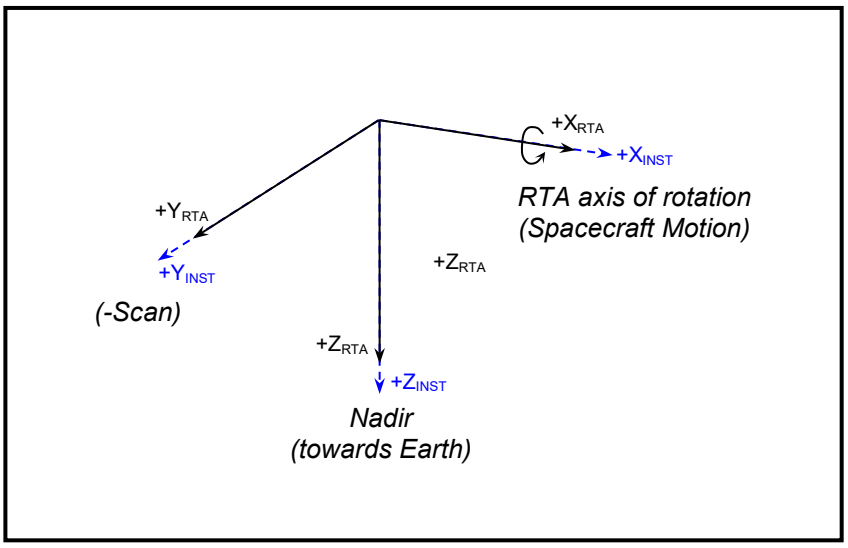

Figure 3-5: Telescope Coordinate System

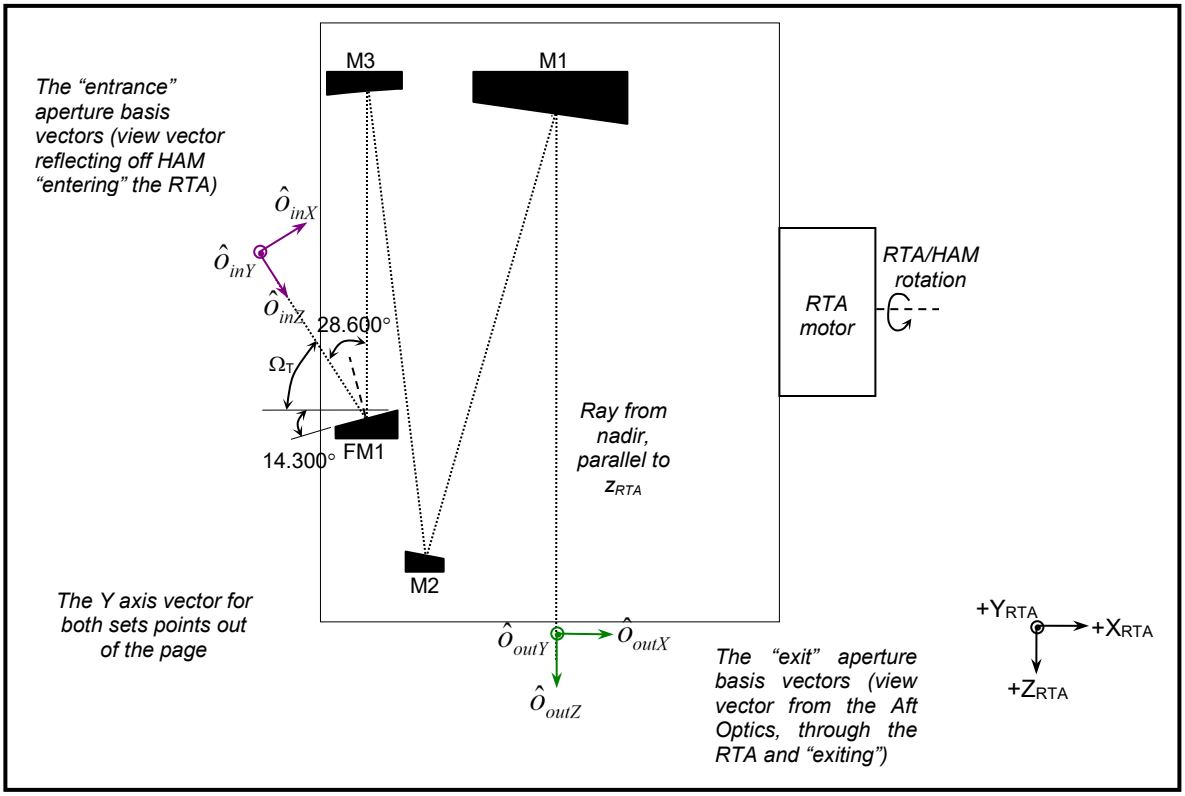

Figure 3-6: Telescope Entrance and Exit Basis Vectors from Aft/Optics

3.3.1.2.6. Instrument Coordinate System

The instrument coordinate system is the coordinate system in which an image space vector emanating from the center of a detector or spatial element number and sample time is converted to an object space viewing vector. It is based on the VIIRS reference axes defined by the VIIRS alignment cube. During preflight testing, the actual alignment of the RTA, HAM, aft optics/focal plane, and the spacecraft coordinate system to the instrument coordinate system will be measured. This relationship will be monitored in-flight by analyzing pointing errors as functions of scan angles. This coordinate system is based on preflight measurements of the orientation of the instrument alignment cube. The sides of this cube could be slightly non-orthogonal because of manufacturing limits but an orthogonal transformation is used to convert to and from this coordinate system. The instrument coordinate system is defined with the positive Z-axis pointing towards nadir, the positive X-axis in the along-track direction (direction of spacecraft motion), and the Y-axis completes the right-hand coordinate system, with positive Y-axis is along the negative scan direction. The instrument coordinate system is illustrated in Figure 3.3-3.

3.3.1.2.7. Spacecraft Coordinate System

The spacecraft coordinate system is fixed to the NPOESS spacecraft with its origin at the spacecraft center of mass. The coordinate axes are defined by the spacecraft attitude control system. It is the orientation of this coordinate system relative to the orbital

coordinate system that is captured in the spacecraft attitude data.

3.3.1.2.8. Orbital Coordinate System

The orbital coordinate system is centered on the satellite and its orientation is based on the spacecraft position in inertial space (Figure 3.3-7). The origin is the spacecraft center of mass with the Z axis pointing from the spacecraft center of mass to the direction perpendicular to the reference ellipsoid. The Y axis is the normalized cross product of the Z axis and the instantaneous (inertial) velocity vector. It corresponds to the direction of the negative of the instantaneous angular momentum vector direction. The X axis is the cross product of the Y and Z axes.

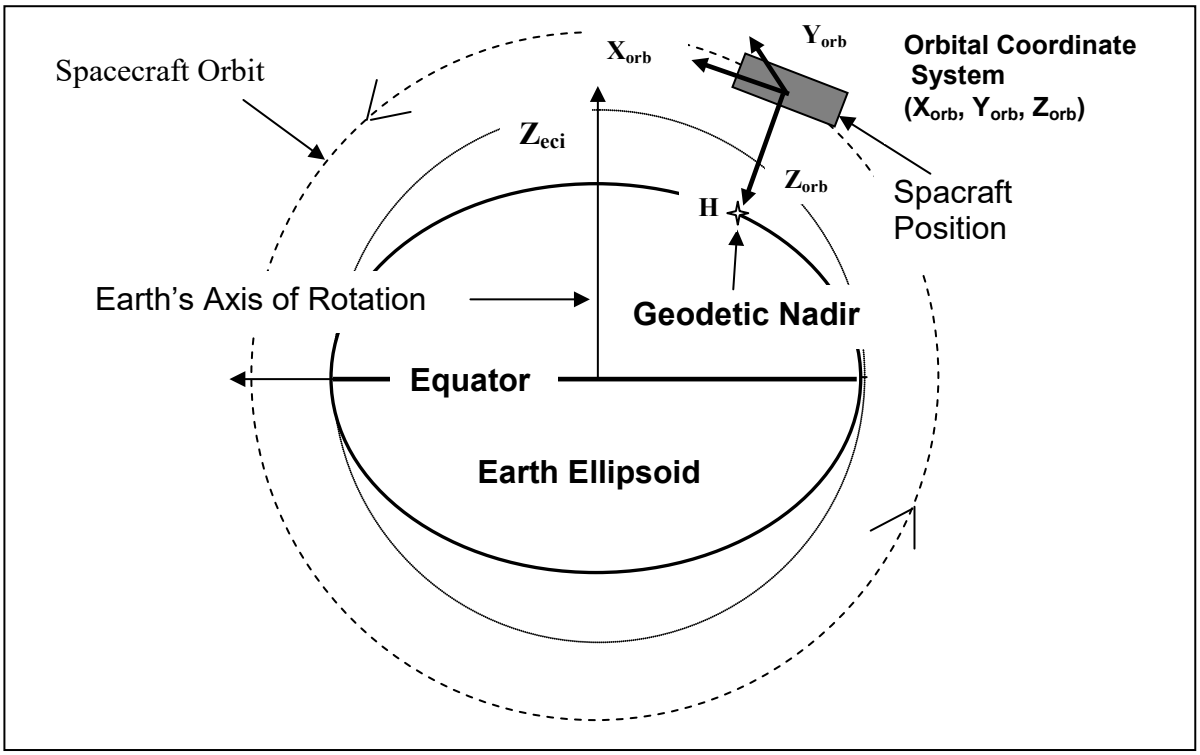

Figure 3-7: Oribital Coordinate System

3.3.1.2.9. Earth Centered Inertial Coordinate System

The Earth Centered Inertial (ECI) coordinate system has its origin at the Earth's center of mass (Figure 3.3-8). The Z axis corresponds to the mean north celestial pole of epoch J2000.0. The X axis is based on the mean vernal equinox of epoch J2000.0. The Y axis is the cross product of the Z and X axes. This coordinate system is described in detail in NIMA, 1997.

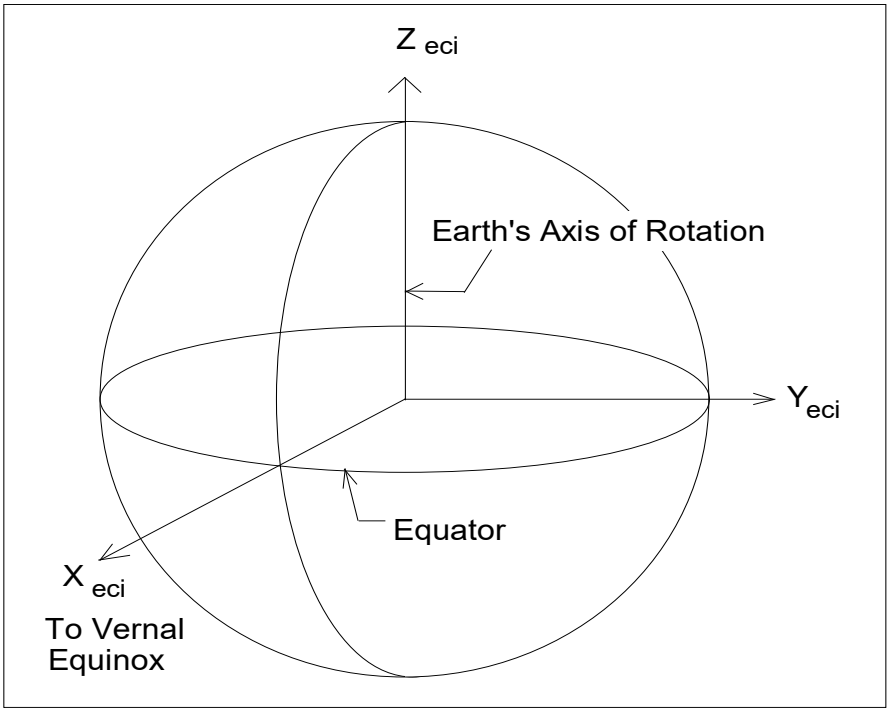

Figure 3-8: Earth Centered Inertial (ECI) Coordinate System

3.3.1.2.10. Earth Centered Earth Fixed Coordinate System

The Earth Centered Earth Fixed (ECEF) coordinate system has its origin at the center of mass of the Earth (Figure 3.3-9). It corresponds to the Conventional Terrestrial System (CTS) defined by the International Earth Rotation Service (IERS), which is the same as the U. S. Department of Defense World Geodetic System 1984 (WGS84) geocentric reference system. This coordinate system is described thoroughly in NIMA, 1997. ECEF can also be referred to as Earth Centered Rotating (ECR) coordinate system.

3.3.1.2.11. Geodetic Coordinate System

The geodetic coordinate system is based on the WGS84 reference frame with coordinates expressed in latitude, longitude, and height above the reference Earth ellipsoid. No ellipsoid is required by the definition of the ECEF coordinate system but the geodetic coordinate system depends on the selection of an Earth ellipsoid. Latitude and longitude are defined as the angle between the ellipsoid normal and its projection onto the equator and the angle between the local meridian and the Greenwich meridian, respectively. The Earth location data fields in each VIIRS SDR will be expressed in the geodetic coordinate system.

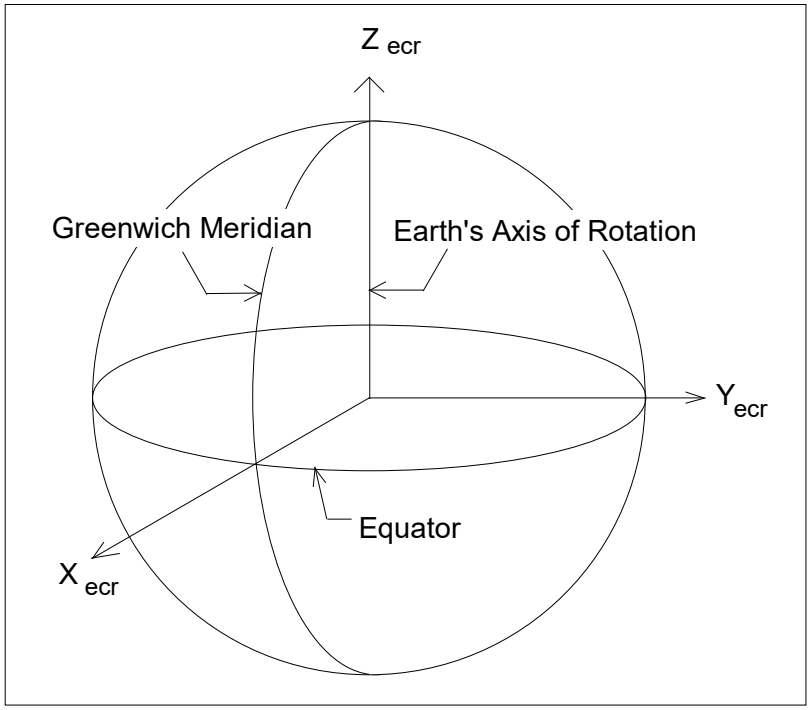

Figure 3-9: ECEF Coordinate System

3.3.1.3. Coordinate Transformations

There are nine transformations between the ten basic coordinate systems used by the VIIRS Earth location algorithm. These transformations are referred to frequently in the remainder of this document and are defined here. They are presented in the logical order in which a spatial element number and sample time would be transformed into a geodetic position. An overview of the ten coordinate systems and their relationship is illustrated in Figure 1.3-2.

3.3.1.3.1. Focal Plane to Aft Optics

The focal planes are rotated by a small angle $\theta_{scanvel}$ of approximately -0.12859 degrees. This rotation is necessary to compensate for the along-track spacecraft sub-satellite point movement of approximately 12.188 m during the 1.853439 milliseconds between the time the leading-edge band (M1) and trailing edge band (M6) see the same area on the ground. The motion along the spacecraft ground track velocity varies a small amount because of the velocity of the Earth relative to the satellite and the orbit's and Earth's eccentricity. The actual rotation will be measured preflight and will be included in the transformation from the focal to the telescope coordinate system. If there is a slight difference in rotation between the focal planes one value will be used and the residual rotation will be absorbed in the detector focal plane locations. The transformation matrix for this rotation is given by:

$$\mathbf{T}_{aft\,/\,foc} = \begin{bmatrix} \cos(\theta_{\text{scanvel}}) & -\sin(\theta_{\text{scanvel}}) & 0 \\ \sin(\theta_{\text{scanvel}}) & \cos(\theta_{\text{scanvel}}) & 0 \\ 0 & 0 & 1 \end{bmatrix} \qquad (3.3\text{-}1)$$

3.3.1.3.2. Aft Optics to Instrument

The aft optics alignment matrix describes the relationship between the aft optics and instrument coordinate systems. This relationship will be measured preflight. The transformation $T_{inst/aft}$ from the aft optics to the instrument coordinate system is a three-dimensional transformation implemented as a matrix multiplication. The transformation matrix is expected to be constant in-flight. Considering that the HAM angle of 23° or 23°+180° makes a view vector (0,0,f) that enters the telescope and points to nadir, the aft optics coordinate system is rotated around $\mathbf{X}_{inst}$ axis by an angle $\mathbf{\Omega_A}$ and another rotation around $\mathbf{X}_{aft}$ by an angle $\mathbf{90° - \Omega_T}$ (Refer to Figure 3.3-10A how a view vector from aft/optics enters the backside of telescope).

The relationship between instrument and initial aft optics coordinate systems before rotation can be expressed by:

$$\begin{bmatrix} 0 & -1 & 0 \\ -1 & 0 & 0 \\ 0 & 0 & -1 \end{bmatrix} \qquad (3.3\text{-}2a)$$

The relationship between aft optics and instrument coordinate system can be built by the following steps[9]:

Step 1. Place a focal plane at Nadir direction as in Figure 3.3-10A.

[9] Much of this procedure was taken from Julian,R.L., "*VIIRS Line of Sight vs Telescope Angles*" *And H.A.M.*
Raytheon SBRS Interdepartmental Correspondence Y0011855, February 2002

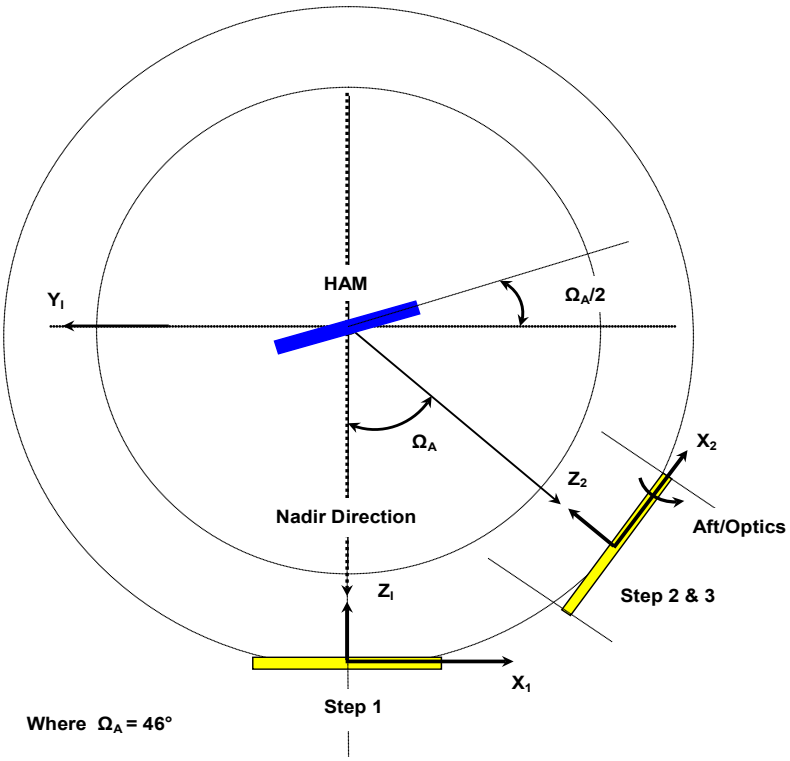

Figure 3-10: Steps in Aft Optics to Instrument Coordinates Transformation

Step 2. Rotate Aft/Optics around axis $\mathbf{X_I}$ by $\mathbf{\Omega_A}$ to Step 2 location.

$$\begin{bmatrix} \cos(\Omega_A) & 0 & -\sin(\Omega_A) \\ 0 & 1 & 0 \\ \sin(\Omega_A) & 0 & \cos(\Omega_A) \end{bmatrix} \tag{3.3-2b}$$

Step 3. Rotate Aft/Optics around axis $\mathbf{X_2}$ by $\mathbf{90° - \Omega_T}$.

$$\begin{bmatrix} 1 & 0 & 0 \\ 0 & \cos(90-\Omega_T) & -\sin(90-\Omega_T) \\ 0 & \sin(90-\Omega_T) & \cos(90-\Omega_T) \end{bmatrix} = \begin{bmatrix} 1 & 0 & 0 \\ 0 & \sin(\Omega_T) & -\cos(\Omega_T) \\ 0 & \cos(\Omega_T) & \sin(\Omega_T) \end{bmatrix} \tag{3.3-3}$$

Combining matrices (1), (2) and (3), $\mathbf{T}_{inst/aft}$ can be expressed by:

$$T_{inst/aft} = \begin{bmatrix} 0 & -1 & 0 \\ -1 & 0 & 0 \\ 0 & 0 & -1 \end{bmatrix} \begin{bmatrix} \cos(\Omega_A) & 0 & -\sin(\Omega_A) \\ 0 & 1 & 0 \\ \sin(\Omega_A) & 0 & \cos(\Omega_A) \end{bmatrix} \begin{bmatrix} 1 & 0 & 0 \\ 0 & \sin(\Omega_T) & -\cos(\Omega_T) \\ 0 & \cos(\Omega_T) & \sin(\Omega_T) \end{bmatrix}$$

$$= \begin{bmatrix} 0 & -\sin(\Omega_T) & \cos(\Omega_T) \\ -\cos(\Omega_A) & \cos(\Omega_T)\sin(\Omega_A) & \sin(\Omega_T)\sin(\Omega_A) \\ -\sin(\Omega_A) & -\cos(\Omega_T)\cos(\Omega_A) & -\sin(\Omega_T)\cos(\Omega_A) \end{bmatrix} \quad (3.3\text{-}4)$$

Current nominal value for Ω_A is 46° and Ω_T is 90°-28.5° (see geometry in Figure 3.3-6). These angles may be updated with measured values for the final flight configuration.

The aft optics coordinate system is tilted with respect to the instrument coordinate system. The resulting side view of HAM and RTA at nadir pointing is illustrated in Figure 3.3-10B.

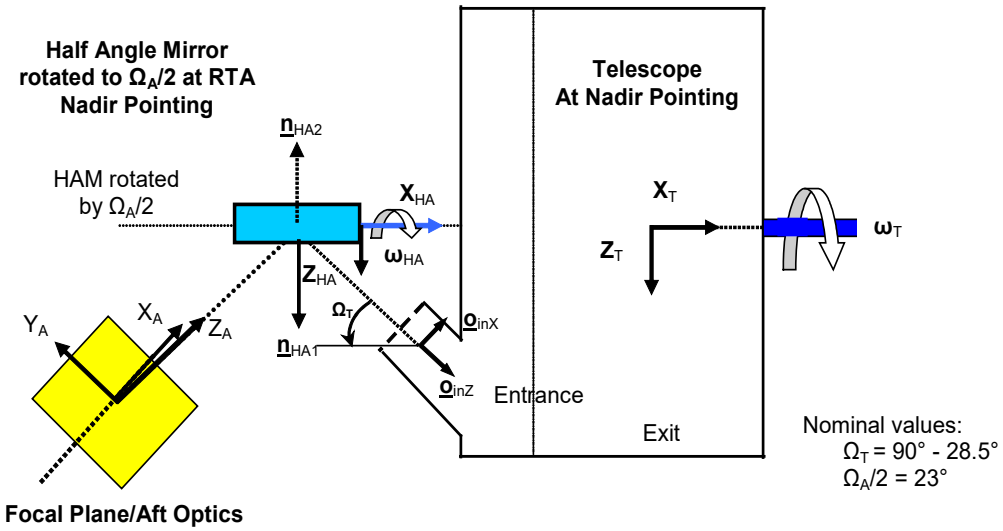

Figure 3-11: VIIRS Optics Model

3.3.1.3.3. Half Angle Mirror to Instrument

The HAM alignment matrix describes the relationship between the HAM and instrument coordinate systems. This relationship will be measured preflight. The transformation $T_{inst/HA}$ from the HAM to the instrument coordinate system is a three-dimensional affine transformation implemented as a matrix multiplication. The transformation matrix is expected to be constant in-flight.

The nominal rotation matrix for a perfectly aligned HAM is:

$$\mathbf{T}_{\text{inst/HA}} = \begin{bmatrix} 1 & 0 & 0 \\ 0 & 1 & 0 \\ 0 & 0 & 1 \end{bmatrix} \tag{3.3-5}$$

The actual transformation matrix $T_{inst/HA}$ will be stored in a geolocation input parameter file.

3.3.1.3.4. Instrument to Solar Diffuser

The transformation matrix that describes the relationship between the instrument coordinate system and the Solar Diffuser assembly is described by the transformation matrix $T_{SD/inst}$:

$$\begin{aligned}
\mathbf{T}_{sd/inst} &= R_z(\gamma_{SD}) R_y(\beta_{SD}) R_z(\alpha_{SD}) \\
&= \begin{bmatrix} \cos\gamma_{SD} & \sin\gamma_{SD} & 0 \\ -\sin\gamma_{SD} & \cos\gamma_{SD} & 0 \\ 0 & 0 & 1 \end{bmatrix} \cdot \begin{bmatrix} \cos\beta_{SD} & 0 & -\sin\beta_{SD} \\ 0 & 1 & 0 \\ \sin\beta_{SD} & 0 & \cos\beta_{SD} \end{bmatrix} \cdot \begin{bmatrix} \cos\alpha_{SD} & \sin\alpha_{SD} & 0 \\ -\sin\alpha_{SD} & \cos\alpha_{SD} & 0 \\ 0 & 0 & 1 \end{bmatrix} \\
&= \begin{bmatrix} \cos\alpha_{SD}\cos\beta_{SD}\cos\gamma_{SD} - \sin\alpha_{SD}\sin\gamma_{SD} & \sin\alpha_{SD}\cos\beta_{SD}\cos\gamma_{SD} + \cos\alpha_{SD}\sin\gamma_{SD} & -\sin\beta_{SD}\cos\gamma_{SD} \\ -\cos\alpha_{SD}\cos\beta_{SD}\sin\gamma_{SD} - \sin\alpha_{SD}\cos\gamma_{SD} & -\sin\alpha_{SD}\cos\beta_{SD}\sin\gamma_{SD} + \cos\alpha_{SD}\cos\gamma_{SD} & \sin\beta_{SD}\sin\gamma_{SD} \\ \cos\alpha_{SD}\sin\beta_{SD} & \sin\alpha_{SD}\sin\beta_{SD} & \cos\beta_{SD} \end{bmatrix} \\
&= \begin{bmatrix} 0.74977311 & -0.54875096 & -0.36974676 \\ 0.59060567 & 0.80696031 & 0 \\ 0.29837096 & -0.21837453 & 0.92913257 \end{bmatrix}
\end{aligned} \tag{3.3-5a}$$

Nominal values for the rotation angles α_{SD}, β_{SD}, and γ_{SD} are:

α_{SD} = -36.2°
β_{SD} = 21.7°
γ_{SD} = 0°

These rotation angles may be updated with measured values for the final flight configuration.

3.3.1.3.5. Telescope to Instrument

The transformation matrix $T_{inst/tel}$ describes the relationship between the telescope and instrument coordinate systems. This relationship will be measured preflight. The transformation $T_{inst/tel}$ from the telescope to the instrument coordinate system is a three-dimensional affine transformation implemented as a matrix multiplication. The transformation matrix is expected to be constant in-flight.

The nominal rotation matrix for a perfectly aligned RTA is:

$$\mathbf{T}_{\text{inst/tel}} = \begin{bmatrix} 1 & 0 & 0 \\ 0 & 1 & 0 \\ 0 & 0 & 1 \end{bmatrix} \quad (3.3\text{-}6)$$

The actual rotation matrix $T_{inst/tel}$ will be stored in a geolocation input parameter file.

3.3.1.3.6. Instrument to Spacecraft

The instrument alignment matrix describes the relationship between the instrument and spacecraft coordinate systems. This relationship will be measured preflight and refined in-flight as described in Section 3.6. The transformation from instrument coordinates to spacecraft coordinates $\mathbf{T}_{\text{sc/inst}}$ is a three dimensional affine transformation implemented as a matrix multiplication. The transformation matrix will initially be defined to be fixed. Subsequent analysis may detect repeatable variations with time that can be effectively modeled making this a (slowly) time varying transformation.

The terminator flexure effect, non-uniform thermal expansion/contraction when going from night to day or vice versa, is one of the dynamic error sources that may be included in this time varying transformation. Typically, the settle time for this phenomenon is several minutes and may have very high frequency components (thermal snap). This error source is expected to be relatively small and below the measurement threshold. Still, analysis will follow to determine if a repeatable pattern can be found. The thermal effects will be monitored yearly, orbit-by-orbit, and over other periods, and variations will be translated into additional attitude corrections. An algorithm to compensate for thermal effects is provided in Appendix A.

The nominal rotation matrix for a perfectly aligned instrument is the identity matrix:

$$\mathbf{T}_{\text{sc/inst}} = \begin{bmatrix} 1 & 0 & 0 \\ 0 & 1 & 0 \\ 0 & 0 & 1 \end{bmatrix} \quad (3.3\text{-}7)$$

The actual rotation matrix $\mathbf{T}_{\text{sc/inst}}$ will be stored in a geolocation input parameter file.

3.3.1.3.7. Spacecraft to Orbital

The relationship between the spacecraft and orbital coordinate systems is defined by the spacecraft attitude. For JPSS satellites, attitude information will be provided as quaternion, which is defined as a transformation from J2000 ECI to spacecraft coordinate system. The quaternions will be converted to Euler angles (see Appendix B) to maintain consistency with the heritage algorithm. The transformation from spacecraft to orbital coordinates is a three-dimensional rotation matrix with the components of the rotation matrix being functions of the spacecraft roll, pitch, and yaw attitude angles. The nature of the functions of roll ξr, pitch ξp, and yaw ξy depends on the exact definition of these angles (i.e. how they are generated by the attitude control system). Wertz (1985) requires

the proper order to perform the rotation to be yaw, roll, and pitch. Since the spacecraft attitude is constantly changing, this transformation is time varying. The transformation matrix is:

$$\mathbf{T}_{\text{orb/sc}} = \begin{bmatrix} \cos\xi_y & -\sin\xi_y & 0 \\ \sin\xi_y & \cos\xi_y & 0 \\ 0 & 0 & 1 \end{bmatrix} \begin{bmatrix} 1 & 0 & 0 \\ 0 & \cos\xi_r & -\sin\xi_r \\ 0 & \sin\xi_r & \cos\xi_r \end{bmatrix} \begin{bmatrix} \cos\xi_p & 0 & \sin\xi_p \\ 0 & 1 & 0 \\ -\sin\xi_p & 0 & \cos\xi_p \end{bmatrix}$$

$$\mathbf{T}_{\text{orb/sc}} = \begin{bmatrix} \cos\xi_y\cos\xi_p - \sin\xi_y\sin\xi_r\sin\xi_p & -\sin\xi_y\cos\xi_r & \cos\xi_y\sin\xi_p + \sin\xi_y\sin\xi_r\cos\xi_p \\ \sin\xi_y\cos\xi_p + \cos\xi_y\sin\xi_r\sin\xi_p & \cos\xi_y\cos\xi_r & \sin\xi_y\sin\xi_p - \cos\xi_y\sin\xi_r\cos\xi_p \\ -\cos\xi_r\sin\xi_p & \sin\xi_r & \cos\xi_r\cos\xi_p \end{bmatrix} \quad (3.3\text{-}8)$$

3.3.1.3.8. Orbital to ECI

The relationship between the orbital and ECI coordinate systems is based on the spacecraft's instantaneous ECI position and velocity vectors. The rotation matrix to convert from orbital to ECI can be constructed by forming the orbital coordinate system axes in ECI coordinates:

P	- Spacecraft position vector in ECI	
V	- Spacecraft velocity vector in ECI	
H	- Geodetic nadir location on ellipsoid in ECI (See Figure 3.3-7)	
p'	- vector **H** $\rightarrow$ **p**	
$\mathbf{T}_{eci/orb}$	- Rotation matrix from orbital to ECI	
$\hat{\mathbf{b}}_3 = -\mathbf{p}'/\lvert\mathbf{p}'\rvert$	- Nadir vector direction	(3.3-9)
$\hat{\mathbf{b}}_2 = \hat{\mathbf{b}}_3 \times \mathbf{v}/\lvert\hat{\mathbf{b}}_3 \times \mathbf{v}\rvert$	- Negative of angular momentum vector direction	(3.3-10)
$\hat{\mathbf{b}}_1 = \hat{\mathbf{b}}_2 \times \hat{\mathbf{b}}_3$		(3.3-11)
$\mathbf{T}_{eci/orb} = \begin{bmatrix} \hat{\mathbf{b}}_1 & \hat{\mathbf{b}}_2 & \hat{\mathbf{b}}_3 \end{bmatrix}$	- Rotation matrix from orbital to ECI	(3.3-12)

3.3.1.3.9. ECI to ECEF

The transformation from ECI to ECEF coordinates is a time varying rotation due primarily to Earth rotation but also containing more slowly varying terms for precession, astronomic nutation, and polar wander. The ECI to ECEF rotation matrix can be expressed as a composite of these transformations:

$$\mathbf{T}_{ecef/eci} = \mathbf{ABCD} \tag{3.3-13}$$

where:

A - Polar Motion

B - Sidereal Time

C - Astronomical Nutation

D - Precession

Each of these transformation terms is described in detail in NIMA, 1997.

3.3.1.3.10. ECEF to Geodetic

The relationship between ECEF and geodetic coordinates can be expressed simply in its direct form (NIMA, 1997):

$$x = (N + h)\cos(lat)\cos(lon) \tag{3.3-14}$$

$$y = (N + h)\cos(lat)\sin(lon) \tag{3.3-15}$$

$$z = (N(1 - e^2) + h)\sin(lat) \tag{3.3-16}$$

$$N = a/(1 - e^2 \sin^2(lat))^{\frac{1}{2}} \tag{3.3-17}$$

$$e^2 = 1 - \frac{b^2}{a^2} \tag{3.3-18}$$

where:

(x, y, z) - ECEF coordinates

(lat, lon, h) - Geodetic coordinates

N - Ellipsoid radius of curvature in the prime vertical

e - Ellipsoid eccentricity

a, b - Ellipsoid semi-major and semi-minor axes

Unfortunately, there is no closed form solution for the inverse problem (which is the problem of interest here). Latitude and height must be solved iteratively for points that do not lie on the ellipsoid surface. This iterative solution is described in Section 3.3.2.2.2.

3.3.2. Mathematical Description of Algorithm

The VIIRS geolocation algorithm is separated into two parts. The first part describes the algorithm that generates a viewing vector in object space corresponding to either the center of a spatial element or a detector. The second part describes the algorithm that calculates the Earth location of the viewing vector.

3.3.2.1. Instrument Model Algorithm

A model of the instrument is used to generate an object space viewing vector in instrument coordinates for a spatial element or detector. The instrument model is composed of three elements: the focal plane/aft optics assembly; the HAM assembly; and the RTA as shown in Figure 3.3-10A. After discussing each model, a summary of the algorithm for the generation of the viewing vector is given.

Instrument models are described in the following order:

- Focal Plane Assembly Model,
- Detector Sampling and Aggregation,
- Aft Optics Model,
- Half Angle Mirror Assembly Model,
- RTA Encoder Assembly,
- RTA Model,
- Generation of the Object Viewing Vector.

3.3.2.1.1. Focal Plane Assembly Model

The layout of the 21 VIIRS spectral bands on the three focal planes were illustrated in Figure 3.3-2A and Figure 3.3-2B. The relationship between the focal plane coordinate system and the aft optics coordinate system is described in the beginning of Section 3.3.1.3.1. The detector sizes, ground resolutions, and number of detectors for each of the bands on these focal planes are given in Table 3.3-1. Refer to Table 3.3-6 for DNB aggregation scheme.

Table 3.3-1: Detector Specifications

Bands	Ground Projection	Detector Size	Number of Detectors
Imagery	371 m (Track) by 129.3 m (Scan)	508.2 μm by 177.1 μm	32
Moderate resolution	742 m (Track) by 259 m (Scan)	1016.4 μm by 354.2 μm	16
Day/Night Band	17.6667m (Track) by 11.2424m (Scan)	24.2 μm by 15.4 μm	66 x 42 x 16 at Nadir

The relative location in units of 'M' band instantaneous Field of View (IFOV) of each of the trailing edges of all bands in the along-scan direction, with respect to the Focal Plane Reference axis, is given in Table 3.3-2 and illustrated in Figure 3.3-12. All the band locations are estimated by the band center locations given in *VIIRS Sensor Overview* (2003 Julian), where all the start bands in three focal planes are aligned, and Ideal band locations for moderate and imagery bands are placed at the trailing edge of band M6.

Table 3.3-3 displays each band center location of x-coordinate (X_{cen}) in mm with respect to the Focal Plane Reference Axis. The relative locations of the start bands and locations of ideal bands may change based on a detailed analysis by SBRS.

Table 3.3-2: Nominal Band Layout with Respect to Focal Plane Reference Axis

Band (j)	Distance from Ref. Axis (given in M-Band IFOV units) (F_j)	Band (j)	Distance from Ref. Axis (given in M-Band IFOV units) (F_j)
Ideal Band	0	M13-Odd	-21
M1	-21	M13-Even	-18
M2	-18	M14-Odd	13
M3	-12	M14-Even	16
M4	-15	M15-Odd	7
M5	-3	M15-Even	10
M6	0	M16A-Odd	-5
M7	-6	M16A-Even	-2
M8-Odd	11	M16B-Odd	1
M8-Even	14	M16B-Even	4
M9-Odd	17	I1	-10
M9-Even	20	I2	-8
M10-Odd	-1	I3-Odd	-5.5
M10-Even	2	I3-Even	-4.0
M11-Odd	5	I4-Odd	-10.0
M11-Even	8	I4-Even	-8.5
M12-Odd	-15	I5-Odd	-10.0
M12-Even	-12	I5-Even	-8.5
		DNB	N/A

Table 3.3-3: Band Center Location with Respect to Focal Plane Reference Axis

Band	X_{cen} (mm)	Band	X_{cen} (mm)
Ideal Band M0	0.1771	Ideal Band I0	0.08855
M1	7.6153	M13-Odd	7.6153
M2	6.5527	M13-Even	6.5527

Band	X_{cen} (mm)	Band	X_{cen} (mm)
M3	4.4275	M14-Odd	-4.4275
M4	5.4901	M14-Even	-5.4901
M5	1.2397	M15-Odd	-2.3023
M6	0.1771	M15-Even	-3.3649
M7	2.3023	M16A-Odd	1.9481
M8-Odd	-3.7191	M16A-Even	0.8855
M8-Even	4.7817	M16B-Odd	-0.1771
M9-Odd	-5.8443	M16B-Even	-1.2397
M9-Even	-6.9069	I1	3.63055
M10-Odd	0.5313	I2	2.92215
M10-Even	-0.5313	I3-Odd	2.03665
M11-Odd	-1.5939	I3-Even	1.50535
M11-Even	-2.6565	I4-Odd	3.63055
M12-Odd	5.4901	I4-Even	3.09925
M12-Even	4.4275	I5-Odd	3.63055
		I5-Even	3.09925

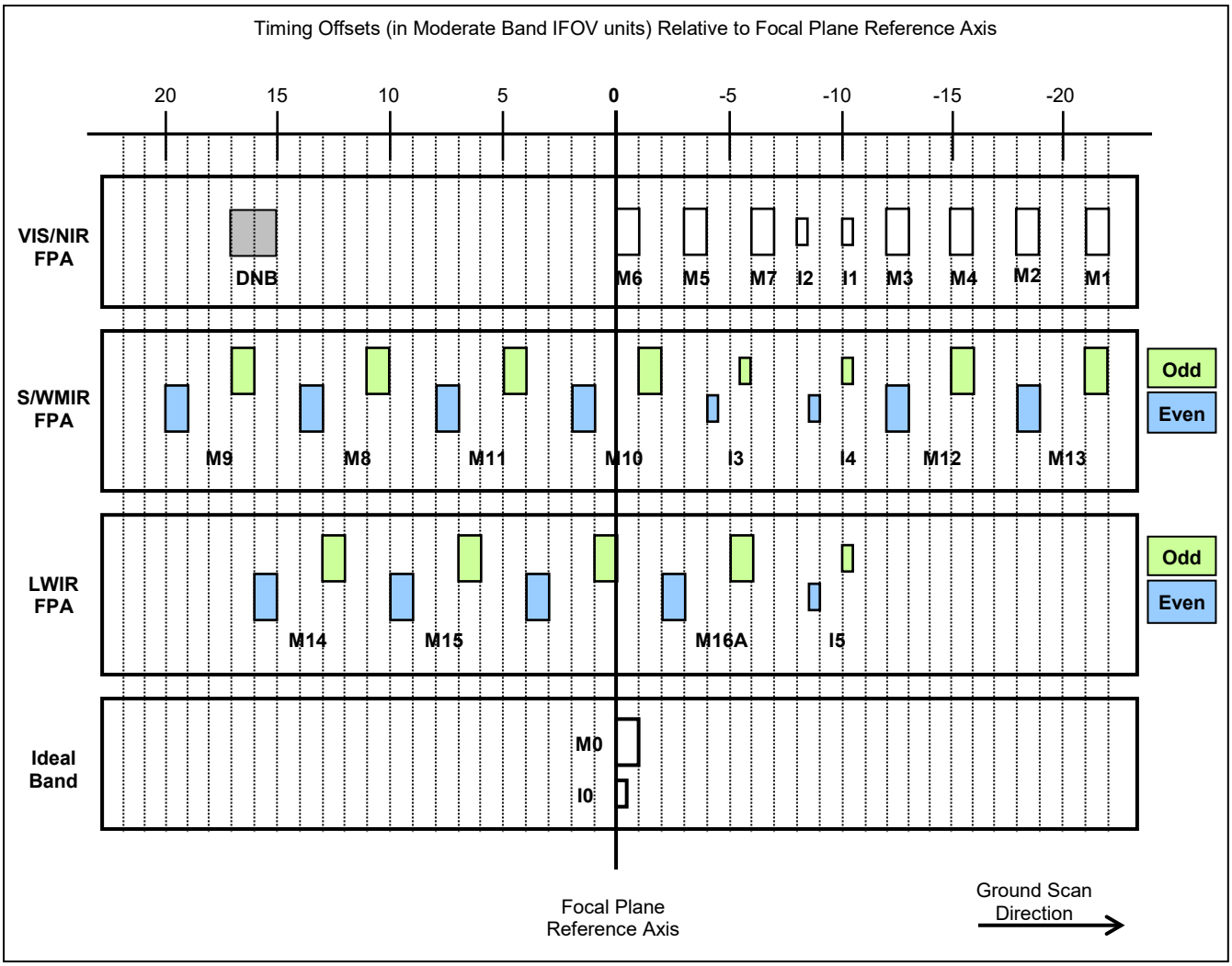

Figure 3-12: Offset of Each Band Relative to the Focal Plane Reference Axis

Note that the DNB location is estimated from its physical location in VIS/NIR/DNB focal plane. One IFOV corresponds to 0.3542 mm on a focal plane.

The detectors are laid out on the focal plane so that when they are sampled there are an integral number of frames between the M bands. The actual locations of each of the bands without the optical distortions will be measured both preflight and in-flight. The location $(x_{i,j}, y_{i,j})$ of the center of detector *i* in band *j* is:

$$\begin{aligned} x_{i,j} &= x_{\text{cen}\,j} + x_{\text{resi},j} \\ y_{i,j} &= y_{\text{cen}\,j} + y_{\text{space}\,j}\left[i - \tfrac{1}{2}(N_{\text{det}\,j} + 1)\right] + y_{\text{resi},j} \end{aligned} \quad [10] \qquad (3.3\text{-}19)$$

[10] The geolocation science code implements a detector renumbering scheme that is required by CCR-184 by reversing

where (see Figure 3.3-13):

$(x_{\text{cen}\,j}, y_{\text{cen}\,j})$ - Location of the center of band *j* relative to the optical axis

$N_{\text{det}\,j}$ - Number of detectors for band *j*

$y_{\text{space}\,j}$ - Spacing between detectors for band *j*

$(x_{\text{res}\,i,j}, y_{\text{res}\,i,j})$ - Residual distortion for detector *i*, band *j*

$i = 1, ..., N_{\text{det}\,j}$ - Detector number for band *j* (see Table 3.3-1)

The equation for computing $x_{\text{cen}\,j}$ term in the equation for $x_{i,j}$ band *j*:

$$x_{\text{cen}\,j} = -(B_{pos} - 0.5 / N_{samp}) * N_{samp} * x_{\text{space}\,j} * f_j / f_0 \qquad \text{(3.3-19a)}$$

where:

B_{pos} - Location of band j in Moderate IFOV units (see Table 3.3-1B)

N_{samp} - Scale factor, N_{samp} = 1 for MOD and DNB, N_{samp} =2 for IMG

$x_{\text{space}\,j}$ - Spacing between detectors in scan direction for band *j*

f_j - Focal length for band *j* (band *j* = 0 is the ideal band)

For calculations involving the ideal 'M' band the values for these quantities are:

$$(x_{\text{cen}}, y_{\text{cen}}) = (177.1\mu\text{m}, 0)$$
(for the I bands, $(x_{\text{cen}}, y_{\text{cen}}) = (88.55\mu\text{m}, 0)$) (3.3-20)

$$N_{\text{det}} = 16$$
(for the I bands, $N_{\text{det}} = 32$) (3.3-21)

$$y_{\text{space}} = 1016.4\mu\text{m}$$
(for the I bands, $y_{\text{space}} = 508.2\mu\text{m}$) (3.3-22)

$$(x_{\text{res}\,i}, y_{\text{res}\,i}) = (0,0) \qquad \text{(3.3-23)}$$

---

the order of the two terms in the square brackets of the $y_{i,j}$ equation: $\left\lfloor \frac{1}{2}(N_{\text{det}\,j} + 1) - i \right\rfloor$

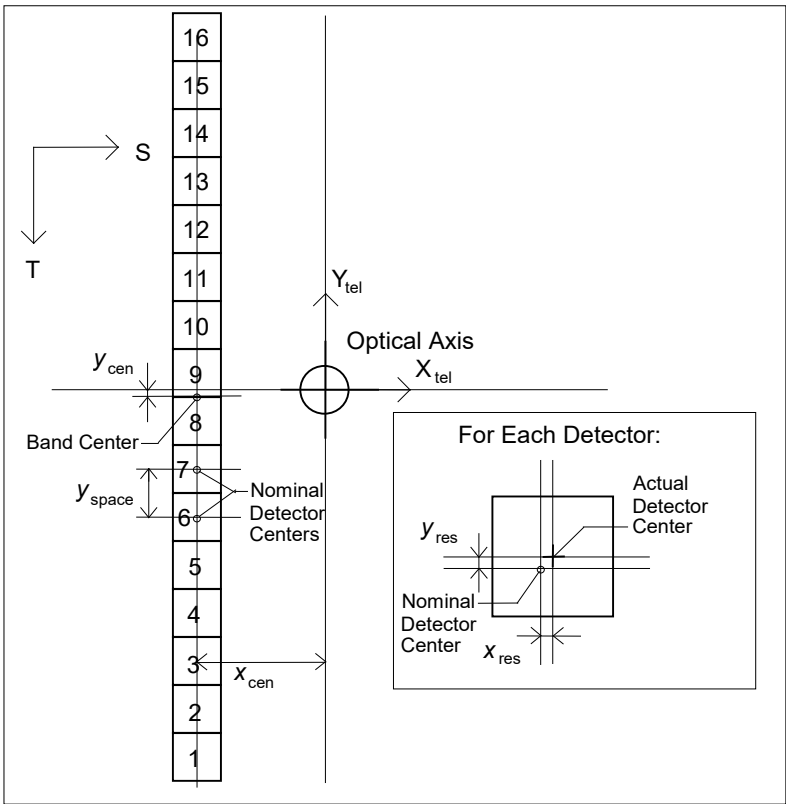

Figure 3-13: Measurements of Detector Locations on Focal Plane

3.3.2.1.2. Detector Sampling and Aggregation

Moderate resolution band detectors are sampled every 88.529 μsec and the imagery band detectors are sample twice as often. The raw samples are aggregated in the along-scan direction to normalize the effective ground footprint of each aggregated sample over the full range of VIIRS scan angles, as noted above. There are three aggregation regions: for scan angles between –31.589 degrees and +31.589 degrees three raw samples are aggregated to form one output sample. This reduces the effective number of samples in this zone from 7104 to 2368 for the imagery bands and from 3552 to 1184 for the moderate resolution bands. The second aggregation zone covers scan angles between +/-44.680 degrees and +/–31.589 degrees. Two raw samples are aggregated to create each output sample in this zone. This reduces the effective number of samples in this zone from 2944 (1422 on each side) to 1472 (736 on each side) for the imagery bands and from 1472 (736 on each side) to 736 (368 on each side) for the moderate resolution bands. For scan angles between +/-56.063 degrees and +-44.680 degrees no sample aggregation is applied. There are 2560 (1280 per side) imagery band samples and 1280 (640 per side) moderate resolution band samples in this zone. The sample time, number of raw samples, and number of aggregated samples per scan for each type of band are given in Table 3.3-4. The actual integration time is given by Table 3.3-5 for each band. Readout time (T_{reset}) is the difference between sample time and integration time.

Table 3.3-4: Detector Sampling

Bands	Actual/Effective Sample Time (µs)	Number of Samples per Scan	Number of Samples after Aggregation
Imagery Agg 1	44.13 44.13	2560	2560
Imagery Agg 2	44.13 88.529	2944	1472
Imagery Agg 3	44.13 132.39	7104	2368
Imagery Total	N/A	12608	6400
Moderate resolution Agg 1	88.529 88.529	1280	1280
Moderate resolution Agg 2	88.529 176.52	1472	736
Moderate resolution Agg 3	88.529 264.78	3552	1184
Moderate resolution Total	N/A	6304	3200

For purposes of line-of-sight generation, the effective sample times are taken to be the raw sample time of the central raw sample in the three sample aggregation zone, the mean of the two raw sample times in the two sample aggregation zone, and the raw sample time in the one sample aggregation zone.

Table 3.3-5: Band and Frame Integration Times

Vis/NIR FPA		S/MWIR FPA		LWIR FPA	
Band	**Integration Time(µs)**	**Band**	**Integration Time(µs)**	**Band**	**Integration Time(µs)**
M1	77.23	M8	77.23	M14	79.43
M2	77.23	M9	77.23	M15	79.43
M3	77.23	I3	33.10	I5	22.06
M4	77.23	M10	77.23	M16	79.43
I1	33.10	M11	77.23		
M5	77.23	I4	33.10		
M6	77.23	M12	77.23		
I2	33.10	M13	77.23		
M7	77.23				

The DNB has the same along-track extent on the FPA as all the other bands however where the other bands have 16 or 32 along-track detectors the DNB has 672 "sub-pixel" detectors. When scanning near nadir 16 pixels per frame are constructed on-board from an aggregation of 42 along-track sub-pixel detectors each. These 16 pixels coincide with the 16 ideal ‘M’ band pixels only at nadir. As the sensor scans away from nadir the number of sub-pixel detectors in the aggregation is reduced to eliminate the bow-tie effect and to keep the field of view on the ground very nearly constant at 0.742 km. This scheme involves a total of 32 different aggregation modes, each of which is used on both sides of nadir. Table 3.3-6 shows how the DNB sub-pixel detectors are aggregated from nadir to end of scan for NPP and J2[11]. Figure 3.3-14 illustrates where these 32 aggregation modes project to the ground this half of a scan. The number of aggregation modes used for J1 DNB is less than 32 (see Appendix C). The S/C is assumed to be at its nominal 833km altitude and the orbit inclination is assumed to be zero, and the sub-spacecraft point is assumed to be at latitude/longitude (0, 0).

[11] J1 VIIRS DNB aggregation is different from NPP, see Appendix C.

Table 3.3-6: DNB Aggregation for NPP and J2 (Nadir to End-of-Scan)

Aggregation Mode from Nadir	Number of Sub-pixels per Pixel		Number of Pixels per Mode	Time per Pixel (sec)
	Track Direction	Scan Direction		
1	42	66	184	2.5326E-04
2	42	64	72	2.4559E-04
3	41	62	88	2.3791E-04
4	40	59	72	2.2640E-04
5	39	55	80	2.1105E-04
6	38	52	72	1.9954E-04
7	37	49	64	1.8803E-04
8	36	46	64	1.7652E-04
9	35	43	64	1.6500E-04
10	34	40	64	1.5349E-04
11	33	38	64	1.4582E-04
12	32	35	80	1.3431E-04
13	31	33	56	1.2663E-04
14	30	30	80	1.1512E-04
15	29	28	72	1.0744E-04
16	28	26	72	9.9770E-05
17	27	24	72	9.2095E-05
18	27	23	32	8.8258E-05
19	26	22	48	8.4421E-05
20	26	21	32	8.0583E-05
21	25	20	48	7.6746E-05
22	25	19	40	7.2909E-05
23	24	18	56	6.9071E-05
24	24	17	40	6.5234E-05
25	23	16	72	6.1397E-05
26	23	15	24	5.7559E-05
27	22	15	32	5.7559E-05
28	22	14	64	5.3722E-05
29	21	13	64	4.9885E-05
30	21	12	64	4.6048E-05
31	20	12	16	4.6048E-05
32	20	11	80	4.2210E-05
Total			**2032**	

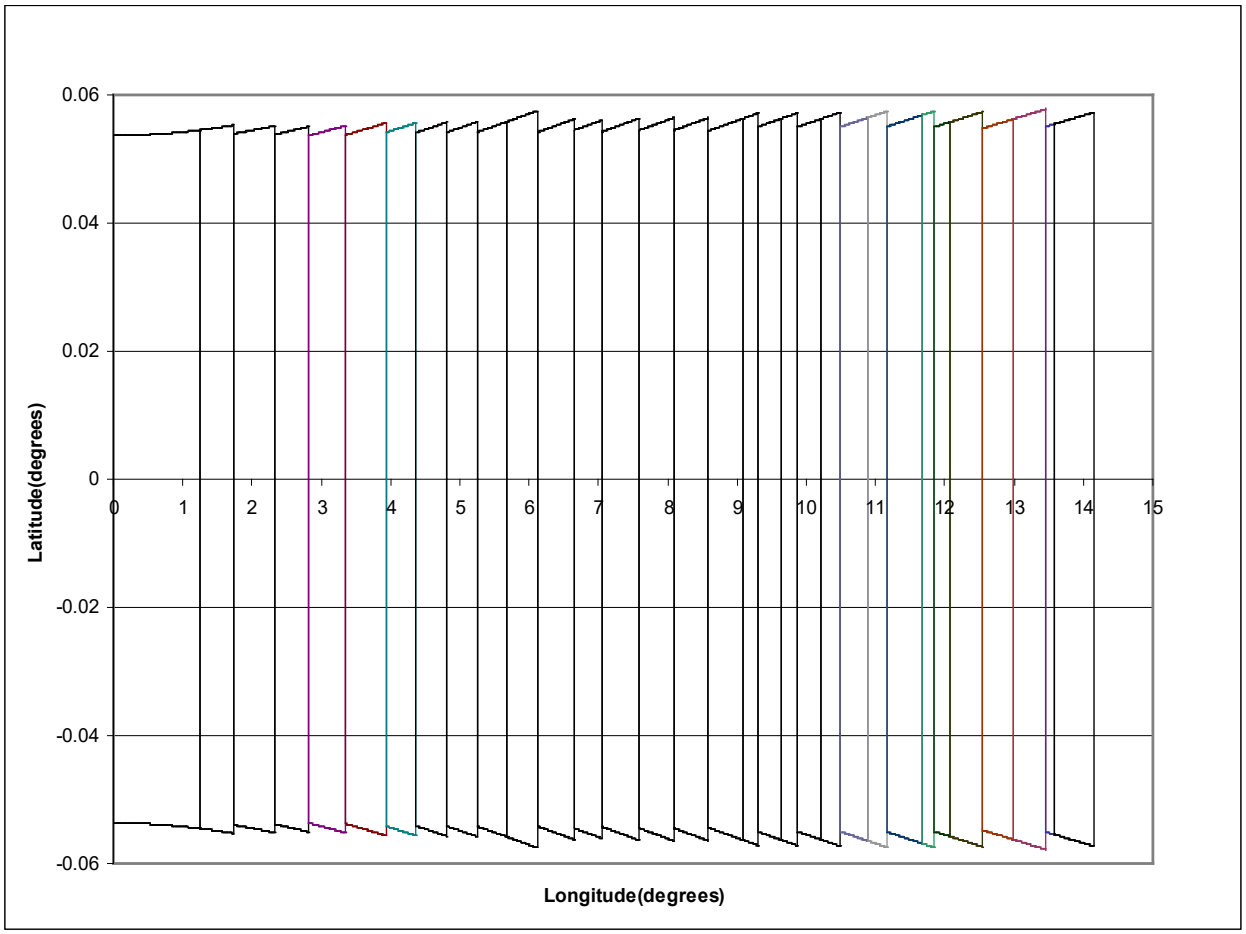

Figure 3-14: DNB Aggregation Zone Ground Coverage for NPP and J2 (Nadir to End-of-Scan)

3.3.2.1.3. Time-Tagging of Individual Frames in Each Band

Due to the along-scan aggregations that are necessary to build VIIRS pixels, VIIRS specific time tagging algorithms are explained for each band type. A frame numbering convention is used where '1' rather than '0' indicates the first frame. Let t_{scan_start} be the time associated with the "Earth Start" trigger encoder[12]. The Earth Start trigger is a pseudo 15-bit RTA encoder tick that triggers the start of the Earth View scan by resetting the scan time clock. There is a small time delay between the Earth Start tigger time and when the scan time clock is reset to zero. This time delay is denoted at t_{sync} and it varies from scan to scan. Details of how t_{sync} is computed will be discussed in Section 3.3.2.1.6.

3.3.2.1.3.1. Moderate and Imagery Resolution Frame Time Tagging

A set of 16 along-track samples is produced every 88.259 μs for each 'M' band and a set of 32 along-track samples is produced every 44.1295 μs for each 'I' band during the Earth View segment of each scan. Let Δt represent this sampling frame time where Δt = 88.259

[12] This "Earth Start" value is provided in Table 54 "Uploadable Table ID 8" in the VIIRS Engineering Data Description (EDD) document, EDD154640-104 (Rev P).

μs for the 'M' bands, and Δt = 44.1295 μs for the 'I' bands.

Before aggregation:

The frame time calculation starts with the time at the Earth view trigger, (t_{scan_start}), and the sync time delay is added to compute the time when the scan time clock is reset to zero. The term *earth_view_delay* represents a timing delay after the start of the scan time clock to allow for electronic settling before Earth view sampling[13], or any additional timing offsets needed to co-align the bands. Note that M1 is the first band that images the ground, and all of the other bands see the same spot on the ground at a slightly later time since they are physically offset from M1 on the FPA. All of the bands have timing offsets relative to M1 in order to co-register the bands; however, these offsets are not used in the *earth_view_delay* calculation since the band timing offsets and the band position offsets are designed to cancel each other so that the bands (including the ideal bands) are co-aligned with M1. The earth_view_delay time currently includes only the timing delay to allow for electronic settling. The reset time, T_{reset}, is the time for reading out the data and is defined as the frame time minus the integration time given in Table 3.3-5. Note that the readout time occurs at the beginning of the frame time. The general equation for the frame time t_i of the i^{th} frame is given by:

$$t_i = t_{scan\_start} + t_{sync} + earth\_view\_delay + (i-1)\cdot\Delta t + 0.5(\Delta t + T_{reset}) \quad (3.3\text{-}24)$$

for: i = 1, … 6304 ('M' band) or

i = 1, … 12608 ('I' band)

Note: Δt and T_{reset} change for MOD or IMG samples

After aggregation:

For 3200 'M' band frames using Δt = 88.259 μs:

Aggregation Zone	Frame Time Equation	Frame Number Range
1	$T_i = t_i$	i = 1, …, 640
2	$T_{641}=T_{640} + 1.5\ \Delta t$ $T_i = T_{i-1} + 2\Delta t$	641 i = 642, …,1008
3 & 4	$T_{1009} = T_{1008} + 2.5\Delta t$ $T_i = T_{i-1} + 3\Delta t$	1009 i = 1010, …, 2192
5	$T_{2193} = T_{2192} + 2.5\Delta t$ $T_i = T_{i-1} + 2\Delta t$	2193 i = 2194, …, 2560

[13] The number of delay samples periods for each band to align with Band M1 is listed in Table 53, "Uploadable table ID 7 description table" in the VIIRS Engineering Data Description (EDD) document, EDD154640-104 (Rev P).

6	$T_{2561} = T_{2560} + 1.5\ \Delta t$ $T_i = T_{i-1} + \Delta t$	2561 i = 2562, …, 3200

For 6400 'I' band frames using Δt = 44.1295 µs:

Aggregation Zone	Frame Time Equation	Frame Number Range
1	$T_i = t_i$	i = 1, …, 1280
2	$T_{1281}=T_{1280} + 1.5\ \Delta t$ $T_i = T_{i-1} + 2\Delta t$	1281 i = 1282, …, 2016
3 & 4	$T_{2017} = T_{2016} + 2.5\Delta t$ $T_i = T_{i-1} + 3\Delta t$	2017 i = 2018, …, 4384
5	$T_{4385} = T_{4384} + 2.5\Delta t$ $T_i = T_{i-1} + 2\Delta t$	4385 i = 4386, …, 5120
6	$T_{5121} = T_{5120} + 1.5\ \Delta t$ $T_i = T_{i-1} + \Delta t$	5121 i = 5122, …, 6400

3.3.2.1.3.2. Day-Night Band

A set of 16 along-track pixels is produced every observation period during the Earth View segment. The time corresponding to an observation period is dependent on which of the 32 along-scan aggregation zones the observation is taken. The 32 along-scan aggregation zones are described in Table 3.3-6. The observation period is the number of along-scan photosites times the sampling time per photosite. The DNB photosite sampling rate is approximately 260.6 KHz.

As mentioned previously, the start of the Earth View segment is triggered by the Earth Start encoder. After a short synchronization time denoted by t_{sync}, the scan time clock is reset to zero and the the Earth view collection begins. The earth view period is slightly shorter for the moderate & imagery resolution bands, (6304 x 8.8259E-05 s)=0.5563847 s, versus 0.55658238 s for NPP DNB.

The scan starts in DNB aggregation zone 32 then proceeds to aggregation zone 1 through nadir then to aggregation zone 32 again at end of scan[14]. Aggregation zone 32 has 11 along-scan photosites so the time for DNB pixel 1 ($T_{DNB(1)}$) will be

$$T_{DNB(1)} = t_{scan\_start} + t_{sync} + N_{delay\_DNB} \cdot \Delta t_{MOD} + 0.5 \cdot N_{agg(32)} \Delta t_{DNB} \qquad (3.3\text{-}25)$$

where:

t_{scan_start} - Scan Start time associated with the "Earth Start" trigger encoder

[14] J1 VIIRS DNB aggregation is different from NPP, see Appendix C.

N_{delay_DNB} - Number of M-band sample periods to the start of DNB sampling

$N_{agg(32)}$ = 11 (the number of along-scan sub-pixel photosites in an aggregation mode 32 pixel (see Table 3.3-6))

Δt_{DNB} = 3.837299E-06 seconds/photosite

[NOTE: all "constants" are subject to change and therefore should be considered as external input parameters to facilitate any needed adjustments.]

For all other pixels except the first pixel in each aggregation zone,

$$T_{DNB(i)} = T_{DNB(i-1)} + N_{agg(j)} \cdot \Delta t_{DNB} \quad (3.3\text{-}26)$$

where:

$N_{agg(j)}$ - The number of along-scan sub-pixel photosites in the aggregation mode *j* that is assigned to the pixel (see Table 3.3-6).

For the first pixel in each aggregation zone (except the first)

$$T_{DNB(i)} = T_{DNB(i-1)} + \Delta t_{DNB} \cdot \left(N_{agg(j)} + N_{agg(j-1)}\right)/2 \quad (3.3\text{-}27)$$

Figure 3.3-15 illustrates how sub-pixels are aggregated during a 4064-frame scan for NPP and J2[15]. Additional detail is provided in Table 3.3-6.

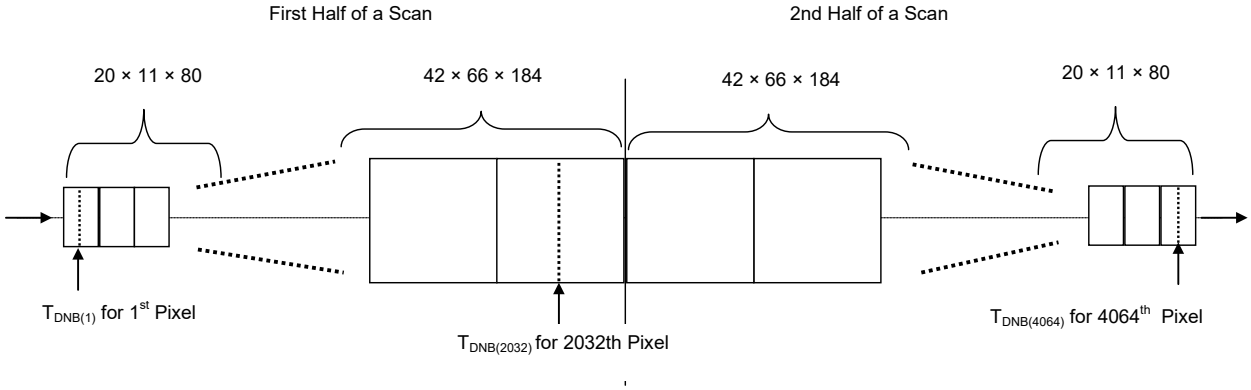

Figure 3-15: Sub-pixel DNB Aggregation Along a Scan for NPP and J2

3.3.2.1.4. Aft Optics Model

The aft optics is modeled as a simple optical system. There are three focal planes illuminated by the aft optics, with several independent elements in the optical path for the

[15] J1 VIIRS DNB aggregation is different from NPP and J2, see Appendix C.

long wave IR focal plane. The optical distortion of the lenses for each optical path was modeled before the focal planes were built and the layout of the detectors on the focal plane was adjusted for this distortion. These adjustments to the detector locations are not included in the focal plane coordinates used in the instrument model; thus, a simple optical model can be used. Given focal plane coordinates (x, y) and aft optics focal length *f*, the corresponding image space-viewing vector $\mathbf{u}_{foc}$ in the aft optics coordinate system is:

$$\mathbf{u}_{\text{foc}} = \begin{bmatrix} x \\ y \\ f \end{bmatrix} \tag{3.3-28}$$

When doing this calculation for an ideal band, the aft optics focal length of 285.25 mm (RTA magnification factor, m = 4) will be used with detector sizes listed in Table 3.3-1. The x and y focal plane coordinates are computed as a function of band and detector number as described above.

3.3.2.1.5. Half Angle Mirror Assembly Model

The Half Angle Mirror (HAM) assembly consists of a double-sided mirror and motor-encoder assembly. The HAM assembly and Rotating Telescope Assembly are shown in Figure 3.3-16.

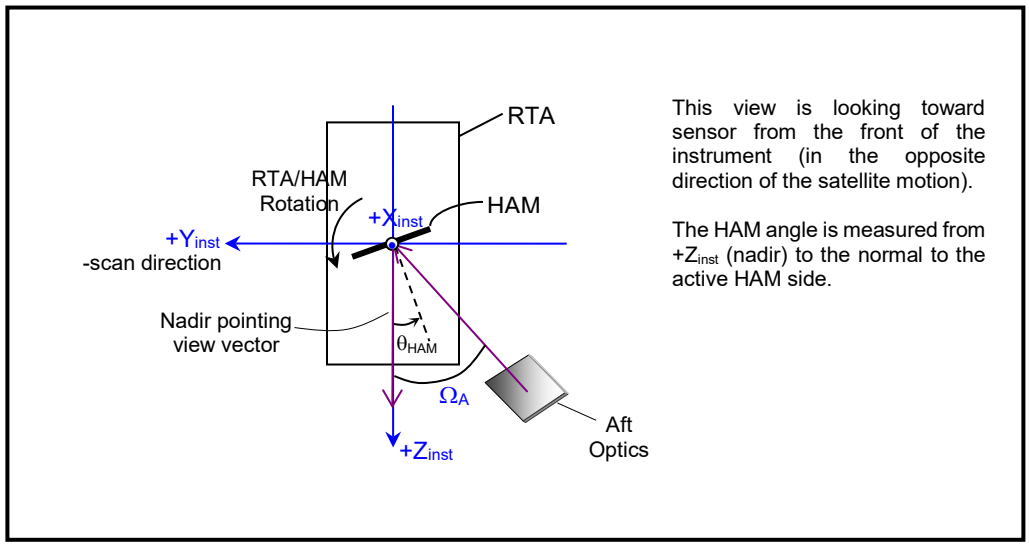

Figure 3-16: HAM and RTA Relationship

The wedge angle α is the non-parallelism of the HAM in the along-scan axis and creates an along-scan offset between scans from mirror sides 1 and 2. The wedge angle β is the non-parallelism of the mirror in the along-track axis and creates an along-track offset (conical scan). The axis error γ is the misalignment of the mirror plane-of-symmetry

(defined as the midway between the 2 mirror surfaces) to the axis of rotation (HAM motor axis), which results in a static, along-track error. There is also a dynamic along-track axis error that is caused by the HAM motor bearings. These along-scan axis errors cause a scan-to-scan along-track overlap or under-lap. The axis error δ is the misalignment of the mirror's nominal axis-of-rotation to the HAM motor axis (see Figure 3.3-18), and does not have a direct geometric effect. The wedge angles and the non-dynamic axis errors are static errors that will be measured preflight and are not expected to change in-flight. The dynamic along-track axis error will be characterized preflight and may be a function of the mirror angular position.

The two wedge angles α and β are illustrated in Figure 3.3-17. Note that the wedge angle α is shown from the top view looking down towards the HAM motor, and the wedge angle β is shown from the side view of the HAM motor.

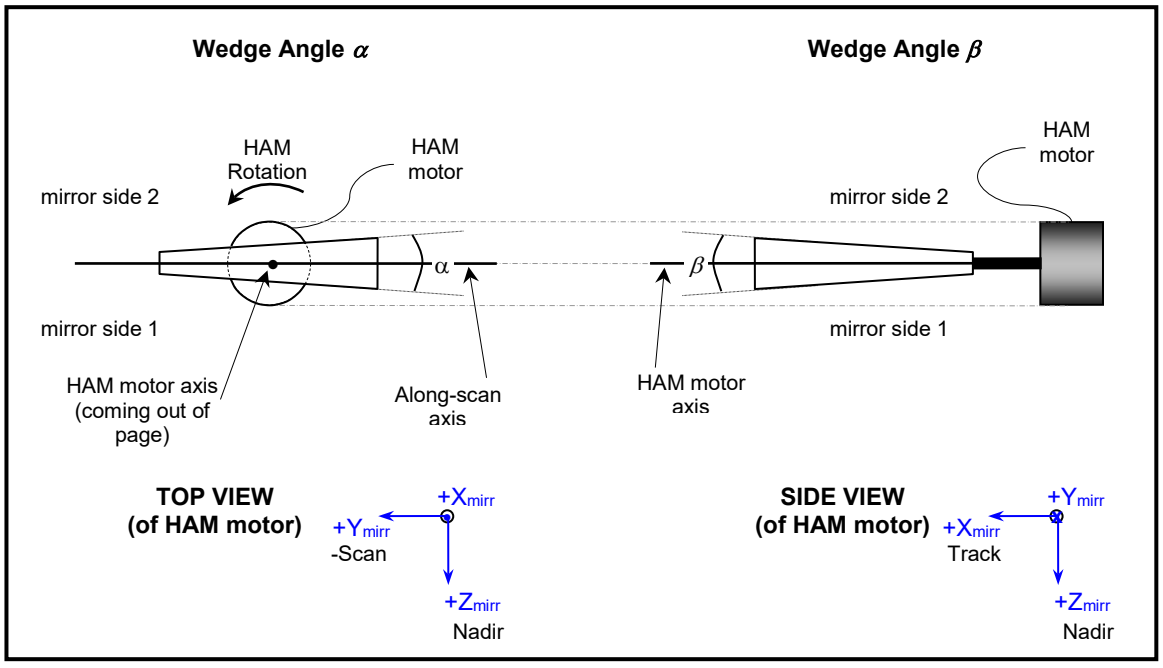

Figure 3-17: Mirror Wedge Angle Errors Definitions

The two axis errors δ and γ are illustrated in Figure 3.3-18. Both axis errors are shown from the side view of the HAM motor; however, for the δ error illustration, the HAM is rotated such that the mirror surface is parallel to the X-Z plane.

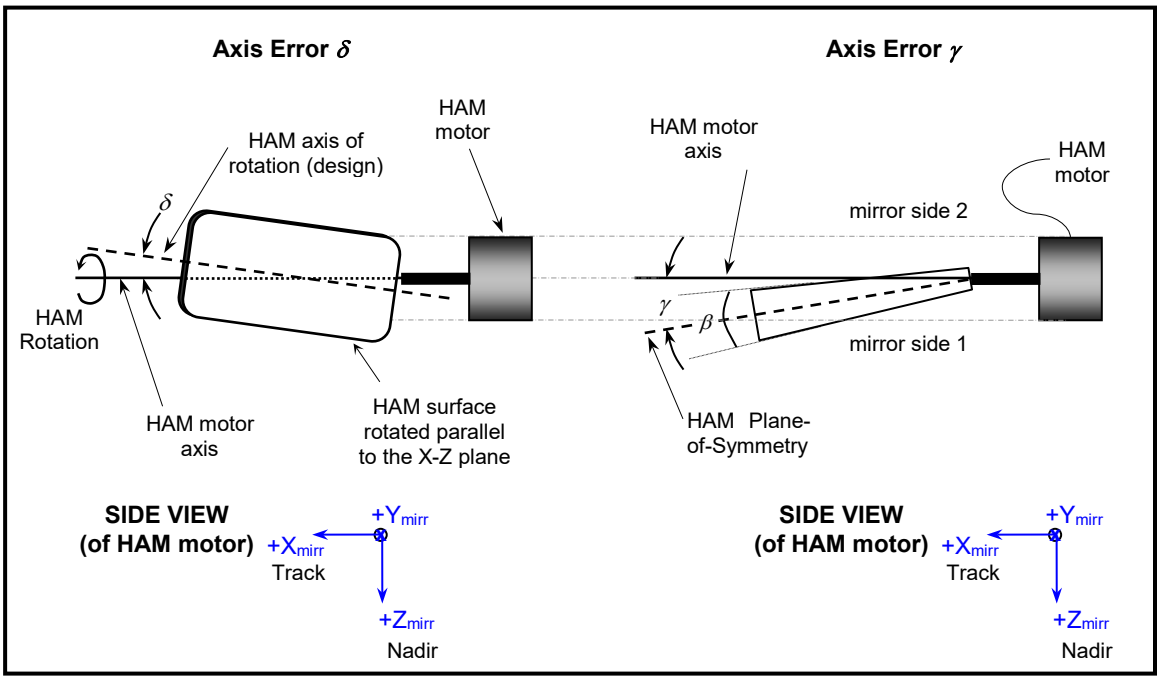

Figure 3-18: Mirror Axis Errors Definitions

The normal vectors for each of the HAM surfaces can be determined from these axis and wedge errors. Figure 3.3-19 illustrates the construction of the normal vectors in the scan mirror coordinate system with zero rotation of the mirror. When the mirror is at the “zero rotation” position, this means that the HAM plane-of-symmetry is exactly parallel to the mirror Y-axis (along-scan axis). At the zero rotation position, the HAM angle is 0˚, where the HAM angle is defined as the angle measured from the mirror Z-axis towards the normal to the active HAM side. Note that the scan mirror coordinate system is co-aligned with the instrument coordinate system.

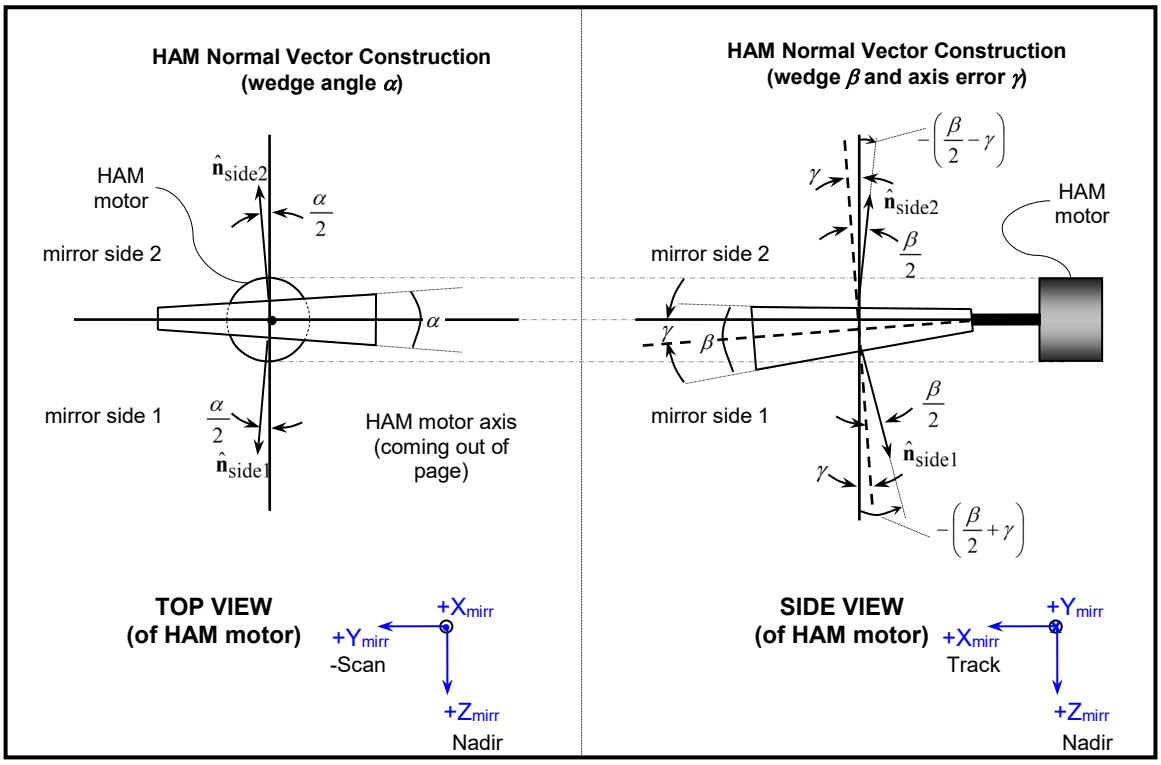

Figure 3-19: Half Angle Mirror Normal Vectors

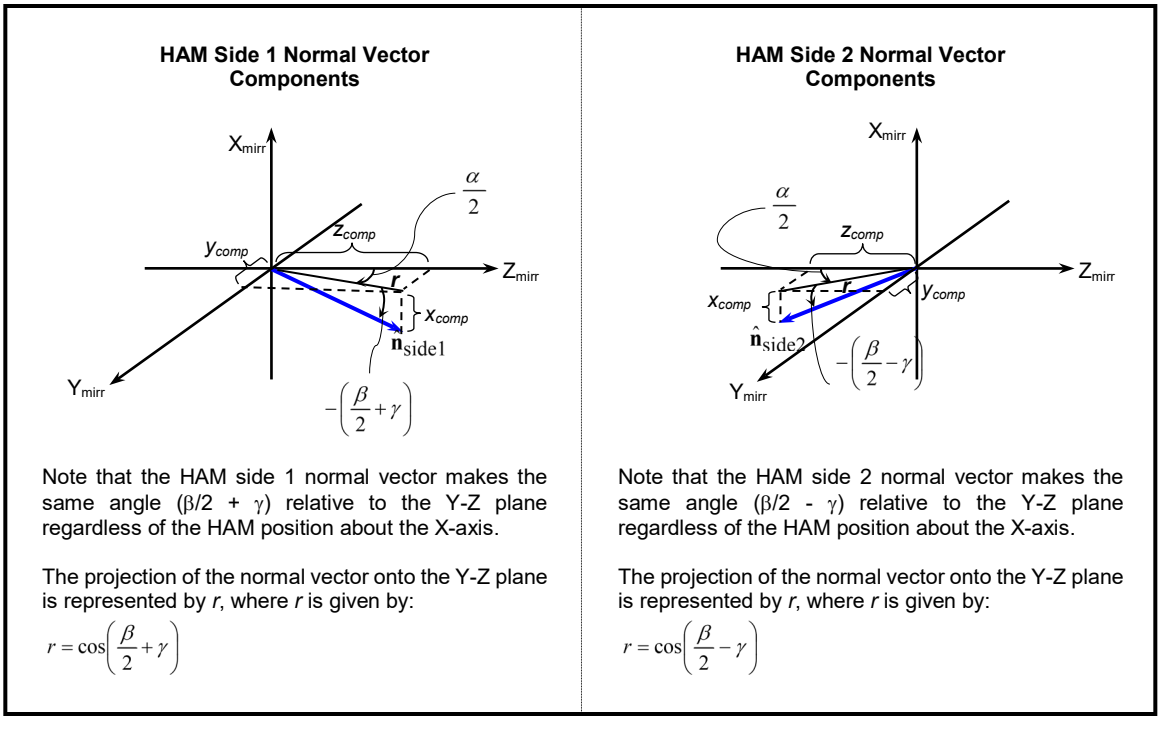

Note that the HAM side 1 normal vector makes the same angle (β/2 + γ) relative to the Y-Z plane regardless of the HAM position about the X-axis.

The projection of the normal vector onto the Y-Z plane is represented by *r*, where *r* is given by:

$$r = \cos\left(\frac{\beta}{2} + \gamma\right)$$

Note that the HAM side 2 normal vector makes the same angle (β/2 - γ) relative to the Y-Z plane regardless of the HAM position about the X-axis.

The projection of the normal vector onto the Y-Z plane is represented by *r*, where *r* is given by:

$$r = \cos\left(\frac{\beta}{2} - \gamma\right)$$

Figure 3-20: HAM Normal Vector Components

Using the geometry in Figure 3.3-20, the normal vectors are:

$$\hat{\mathbf{n}}_{\text{side}1} = \begin{bmatrix} -\sin\left(\frac{\beta}{2}+\gamma\right) \\ \sin\left(\frac{\alpha}{2}\right)\cos\left(\frac{\beta}{2}+\gamma\right) \\ \cos\left(\frac{\alpha}{2}\right)\cos\left(\frac{\beta}{2}+\gamma\right) \end{bmatrix} \tag{3.3-29}$$

$$\hat{\mathbf{n}}_{\text{side}2} = \begin{bmatrix} -\sin\left(\frac{\beta}{2}-\gamma\right) \\ \sin\left(\frac{\alpha}{2}\right)\cos\left(\frac{\beta}{2}-\gamma\right) \\ -\cos\left(\frac{\alpha}{2}\right)\cos\left(\frac{\beta}{2}-\gamma\right) \end{bmatrix} \tag{3.3-30}$$

These equations assume a sign convention as shown in Figure 3.3-20.

The HAM rotates about the HAM coordinate system X-axis. The following rotation matrix is used to rotate a mirror normal vector through an angle of θ_{HA}.

$$\mathbf{T}_{\text{rot}}(\theta_{HA}) = \begin{bmatrix} 1 & 0 & 0 \\ 0 & \cos(\theta_{HA}) & -\sin(\theta_{HA}) \\ 0 & \sin(\theta_{HA}) & \cos(\theta_{HA}) \end{bmatrix} \tag{3.3-31}$$

Each of the mirror normal vectors is only relevant when the mirror side is facing toward the aft optics and telescope entrance. When the mirror is rotated 0 degrees the LOS from the aft optics reflected off HAM side 1 through the RTA is pointed toward nadir. The following equation is used to compute the HAM normal $\hat{\mathbf{n}}_{\text{HA}}$ at any angle θ for the appropriate mirror side *i*:

$$\hat{\mathbf{n}}_{\text{HA}} = \mathbf{T}_{\text{rot}}(\theta_{HA})\hat{\mathbf{n}}_{\text{side}\,i} \tag{3.3-32}$$

where $i = 1$ when $-44.01^o < \theta_{HA} \le 135.99^o$ and $i = 2$ when $135.99^o < \theta_{HA} \le 315.99^o$. HAM angles are determined from HAM encoder values that are present in the VIIRS RDRs.

3.3.2.1.6. RTA and HAM Encoder Assemblies

The RTA and HAM use identical 14-bit motor/optical encoders to report when the RTA and HAM pass pre-determined scan positions. The primary 14-bit encoder pulses (train A) are shifted by 90 degrees to create a secondary train B pulse. The two pulse trains generate an unevenly spaced pseudo 15-bit pulse train. A unique index pulse or absolute reference point is defined for both the RTA and HAM encoders, and the pseudo 15-bit

encoder pulses are counted with respect to the index pulse location. There is one start-of-scan (SOS) trigger encoder that initiates the Earth View scan. This SOS trigger is a pseudo 15-bit RTA encoder that is a configurable parameter stored in an uploadable table[16]. The absolute time at the SOS trigger encoder is reported in the Engineering Packets. In addition, the number in the HAM counter register at the SOS trigger time is saved in the Engineering Packets as the HAM SOS encoder. The SOS trigger value is echoed as the RTA SOS encoder value in the Engineering Packets. The SOS encoder values are needed to relate the relative encoder timestamps to absolute encoder values, referenced to the index pulse. There is a variable sync time which is defined as the time delay from the SOS trigger pulse to the encoder clock counter reset point. This variable sync time must be computed for every scan in order to align the encoder timestamps to the SOS trigger time.

Constants related to the primary encoder output are listed in Table 3.3-7 with derived values in Table 3.3-8. Detector line of sight at a frame time is a function of both the RTA and HAM angle. Because so many encoder pulses are available simple linear interpolation is sufficient to determine RTA and HAM angles at any frame time.

Table 3.3-7: Encoder Geometric Constants[17]

Characteristic (Values for 14-bit encoders)	Value
RTA Encoder Pulses	5160
Number of RTA Time Samples	1290
Encoder Pulses per RTA Time Sample	4
HAM Encoder Pulses	2580
Number of HAM Time Samples	1290
Encoder Pulses per HAM Time Sample	2

Table 3.3-8: Encoder Geometric Derived Values (see Footnote 17)

Characteristic (Values for 14-bit encoders)[18]	Derived Value
Rotation per Encoder Pulse (RTA or HAM)	383.5 μrad
Rotation per RTA Time Samples	1533.98 μrad
Time per RTA Encoder Pulse	1.09033e-04 s
Time per RTA Time Samples	4.36133e-04 s
Rotation per HAM Time Samples	767 μrad

[16] SOS trigger defined by the “Earth Start” parameter in the VIIRS EDD Table 54: “Uploadable Table ID 8”.

[17] Constants refer to the Earth View Sector only, not the entire scan.

[18] These values were calculated using a scan rate of 1.7864 seconds/revolution.

Characteristic (Values for 14-bit encoders)[18]	Derived Value
Time per HAM Encoder Pulse	2.18066e-04 s
Time per HAM Time Samples	4.36133e-04 s

The times at which every 4th 14-bit RTA encoder pulse and every 2nd 14-bit HAM encoder pulse occurs after the start of the Earth view are transmitted as part of the instrument telemetry. A total of 1290 RTA time samples (or timestamps), in units of scan time counter ticks, are collected during the Earth view. The first time a sample is reported at the next rising edge of the train A pulse after the SOS trigger pulse. The scan time counter is a 16-bit counter that resets to zero after the SOS trigger pulse plus the sync time delay. The scan time counter values are reported in the raw encoder data, and the counter will wrap around several times during the earth view scan. The raw encoder data is unwrapped and converted to times by multiplying by the encoder data scale factor, *t_encoder*. The timestamps provide the times at every 4th 14-bit RTA pulse and every 2nd 14-bit HAM pulse relative to the encoder clock counter reset point, $t_{pulserel}$. The relative times must be added to the telemetered Earth view SOS time, t_{SOS} plus the variable sync time, t_{sync}, to generate the absolute time samples t_{pulse}.

$$t_{pulse_i} = t_{SOS} + t_{sync} + t_{pulserel_i} \quad i = 0, \ldots 1289 \tag{3.3-33}$$

The variable delay time between the SOS trigger and the encoder clock reset needs to be computed for every scan. This sync time can be computed by estimating the scan rate from the first two RTA timestamps. The general equation for the sync time is given by:

$$t_{sync} = \frac{t\_encoder}{16} \cdot \left(C\_enc\_adj \cdot T[1] - (C\_enc\_adj + 16) \cdot T[0] \right) \tag{3.3-34}$$

Where: $$C\_enc\_adj = \begin{cases} 4 \; if \; start\_enc_{tel15bit} \; is \; odd \\ 3 \; if \; start\_enc_{tel15bit} \; is \; even \end{cases}$$

- *t_encoder* is the encoder data scale factor, [sec/scan time counter tick]
- T[0] is the relative time of the first RTA timestamp, [scan time ticks]
- T[1] is the relative time of the second RTA timestamp, [scan time ticks]

The encoder timestamps need to be translated to absolute RTA and HAM encoder values in order to convert encoders to angles. Since the RTA and HAM SOS encoder values are provided in the unevenly spaced pseudo 15-bits, all of the values are converted to an evenly spaced virtual 16-bit space to make the calculations easier. This is referred to as a “virtual” 16-bit space since each tick does not directly correspond to the physical 14-bit encoders. The pseudo 15-bit SOS encoder values are converted to the virtual 16-bit value by the following equations:

$$start\_enc_{16bit} = start\_enc_{15bit} * 2 - A\_bit\_adj \quad (3.3\text{-}35)$$

Where:
$$A\_bit\_adj = \begin{cases} 0 \; if \; start\_enc_{15bit} \; is \; odd \\ 1 \; if \; start\_enc_{15bit} \; is \; even \end{cases}$$

Recall that the first timestamp is recorded at the next rising edge of the train A pulse after the SOS trigger. The virtual 16-bit encoder value at the first timestamp (T0) is computed by:

$$n_{16bit}(T0) = start\_enc_{16bit} + B\_HAM\_adj(HAMside) + C\_enc\_adj \quad (3.3\text{-}36)$$

Where:
$$B\_HAM\_adj(HAMside) = \begin{cases} 0 \; if \; HAM \; side \; is \; 0 \\ 32768 \; if \; HAM \; side \; is \; 1 \end{cases} \text{ for HAM,} \quad (3.3\text{-}37)$$

$$B\_HAM\_adj(0) = 0 \text{ always for RTA,} \quad (3.3\text{-}38)$$

$$C\_enc\_adj = \begin{cases} 4 \; if \; start\_enc_{15bit} \; is \; odd \\ 3 \; if \; start\_enc_{15bit} \; is \; even \end{cases}$$

Note that there is no HAM side dependency for the telescope encoder calculations, so the term *B_HAM_adj* is simply set to 0. The encoder values for remaining timestamps can be computed by:

$$n_{tel16bit}(Ti) = n_{tel16bit}(T0) + 16i \text{ for RTA} \quad (3.3\text{-}39)$$

$$n_{HAM16bit}(Ti) = n_{HAM16bit}(T0) + 8i \text{ for HAM} \quad (3.3\text{-}40)$$

Where: i = 1, …, 1289

Note that since the RTA timestamps are sampled every 4th 14-bit encoder pulse, each timestamp is separate by sixteen virtual 16-bit ticks. The HAM timestamps are sampled every 2nd 14-bit encoder, so the HAM timestamps are separated by eight 16-bit ticks. The absolute times and absolute encoder values for the timestamps are used to compute fractional encoder values at any time *t* after the start of the Earth view. To determine the angle at any time *t* after the start of the Earth view, it is necessary to interpolate between the encoder times in the spacecraft telemetry. The Chebyshev polynomials interpolation technique was used in the initial model (based on heritage); however, with so many pulses, linear interpolation should predict the actual angle at any time within 1 μradian [Julian, 2003]. Linear interpolation has been implemented in the current model to

determine the fractional encoder at a given time, *t*.

The pseudo 15-bit encoder numbers at nadir for both the RTA and the HAM were measured during preflight testing. Only one measurement point was provided by the preflight testing since a linear relationship is assumed for the encoder-to-angle conversion. The encoder values at nadir are used to compute the offset coefficients for the linear equation. The measured encoder values are converted to virtual 16-bit values before computing the offset coefficients (A_0 term below). Note that the RTA offset is adjusted by 2π to generate angles measured from $\pm\pi$ about nadir. A 5th order polynomial is used in the geolocation model for the encoder to angle conversion; however, only the first two coefficients (A_0 and A_1) are used. The general equation for converting encoders to angles is given by:

$$\theta = A_0 + A_1 n_{16bit} \tag{3.3-41}$$

where:

$$A_{0\_tel} = NadirAngle_{tel} - A_1 \cdot n_{tel16bit\_meas} - 2\pi \tag{3.3-42}$$

$$A_{0\_HAM} = NadirAngle_{HAM} - A_1 \cdot n_{HAM16bit\_meas} \tag{3.3-43}$$

$$A_1 = \frac{2\pi}{2^{16}} \text{ radians/16-bit tick} \tag{3.3-44}$$

3.3.2.1.7. Telescope Model

The components of the telescope model include two sets of basis vectors: one for the entrance aperture facing the HAM and one for the exit aperture facing the Earth; a magnification factor, and a rotation about the telescope coordinate system X-axis. The aft optics effective focal length for the VIS/NIR, S/MWIR, LWIR, and DNB focal planes is 285.25 mm and the RTA magnification factor is 4. The basic concept of the telescope model is as follows:

1. Construct the entrance and exit aperture basis vectors.
2. Rotate both sets of basis vectors in the telescope coordinate system through the telescope rotation angle.
3. Convert both sets of rotated basis vectors to the instrument coordinate system.
4. Project the viewing vector (after reflection off the HAM) onto the entrance aperture basis vectors by taking scalar (dot) products.
5. Reconstruct the viewing vector using the exit aperture basis vectors.

The relationship between the entrance and exit aperture basis vectors can be shown schematically as shown in Figure 3.3-21.

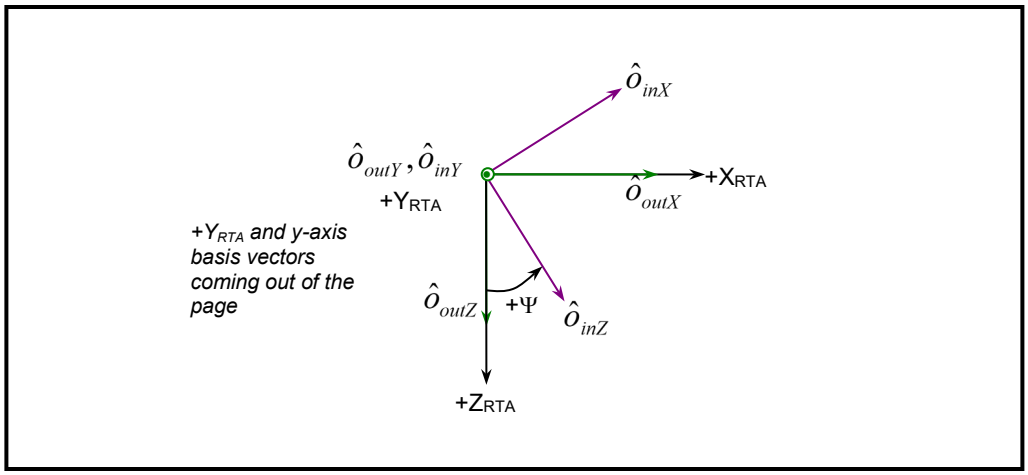

Figure 3-21: Relationship Between Telescope Entrance and Exit Basis Vectors

The entrance aperture basis vectors $(\hat{o}_{inX}, \hat{o}_{inY}, \hat{o}_{inZ})$ are rotated from the exit aperture basis vectors $(\hat{o}_{outX}, \hat{o}_{outY}, \hat{o}_{outZ})$ a positive angle of Ψ about the Y_{RTA} axis. From the geometry shown in Figure 3.3-6, $\Psi = 90° - \Omega_T$, where $\Psi = 28.600°$, and $\Omega_T = 61.4°$. A positive rotation of Ψ about the Y_{RTA} axis can be expressed by the matrix:

$$\begin{bmatrix} \cos(\Psi) & 0 & -\sin(\Psi) \\ 0 & 1 & 0 \\ \sin(\Psi) & 0 & \cos(\Psi) \end{bmatrix} \tag{3.3-45}$$

Substituting in $\Psi = 90° - \Omega_T$ into Equation (1), we have:

$$\begin{bmatrix} \cos(90-\Omega_T) & 0 & -\sin(90-\Omega_T) \\ 0 & 1 & 0 \\ \sin(90-\Omega_T) & 0 & \cos(90-\Omega_T) \end{bmatrix} = \begin{bmatrix} \sin(\Omega_T) & 0 & -\cos(\Omega_T) \\ 0 & 1 & 0 \\ \cos(\Omega_T) & 0 & \sin(\Omega_T) \end{bmatrix} \tag{3.3-46}$$

From Equation (3.3-46), the entrance aperture basis vectors are:

$$\hat{\mathbf{o}}_{inX} = \begin{bmatrix} \sin(\Omega_T) \\ 0 \\ -\cos(\Omega_T) \end{bmatrix} \quad \hat{\mathbf{o}}_{inY} = \begin{bmatrix} 0 \\ 1 \\ 0 \end{bmatrix} \quad \hat{\mathbf{o}}_{inZ} = \begin{bmatrix} \cos(\Omega_T) \\ 0 \\ \sin(\Omega_T) \end{bmatrix} \tag{3.3-47}$$

The exit aperture basis vectors are aligned with the telescope coordinate system axes:

$$\hat{\mathbf{o}}_{outX} = \begin{bmatrix} \cos\delta_T \\ 0 \\ -\sin\delta_T \end{bmatrix} \quad \hat{\mathbf{o}}_{outY} = \begin{bmatrix} 0 \\ 1 \\ 0 \end{bmatrix} \quad \hat{\mathbf{o}}_{outZ} = \begin{bmatrix} \sin\delta_T \\ 0 \\ \cos\delta_T \end{bmatrix} \tag{3.3-48}$$

The angle δ_T represents the deviation of the telescope Z-axis from the nominal direction about the telescope Y-axis. This allows for the telescope model to account for misalignment of the telescope Z-axis from the nominal position (pointing down towards nadir). This δ_T error can be considered as a "pitch" error during the VIIRS scan, and is illustrated in Figure 3.3-22.

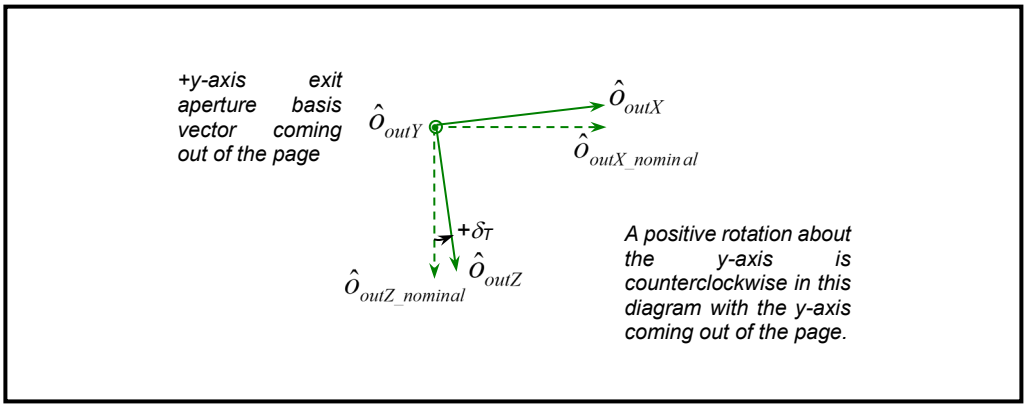

Figure 3-22: Telescope Exit Aperture Coordinate Frame

The telescope rotation is applied in the same manner as the HAM rotation:

$$\mathbf{T}_T(\theta_T) = \begin{bmatrix} 1 & 0 & 0 \\ 0 & \cos(\theta_T) & -\sin(\theta_T) \\ 0 & \sin(\theta_T) & \cos(\theta_T) \end{bmatrix} \tag{3.3-49}$$

Both sets of basis vectors are rotated about the RTA X-axis using the $\mathbf{T}_T$ matrix and then converted to the instrument coordinate system using the telescope to instrument coordinate system transformation matrix $\mathbf{T}_{inst/tel}$ defined in Eq. (3.3-6):

$$\mathbf{M}_{in}(\theta_T) = \left[\hat{\mathbf{o}}'_{inX} \quad \hat{\mathbf{o}}'_{inY} \quad \hat{\mathbf{o}}'_{inZ}\right] = \mathbf{T}_{inst/tel}\mathbf{T}_T(\theta_T)\left[\hat{\mathbf{o}}_{inX} \quad \hat{\mathbf{o}}_{inY} \quad \hat{\mathbf{o}}_{inZ}\right] \tag{3.3-50}$$

The column vectors of matrix $\mathbf{M}_{in}(\theta_T)$ are the rotated entrance aperture basis vectors in the instrument coordinate system. The exit aperture basis vectors are handled similarly to construct the matrix $\mathbf{M}_{out}(\theta_T)$:

$$\mathbf{M}_{out}(\theta_T) = \left[\hat{\mathbf{o}}'_{outX} \quad \hat{\mathbf{o}}'_{outY} \quad \hat{\mathbf{o}}'_{outZ}\right] = \mathbf{T}_{inst/tel}\mathbf{T}_T(\theta_T)\left[\hat{\mathbf{o}}_{outX} \quad \hat{\mathbf{o}}_{outY} \quad \hat{\mathbf{o}}_{outZ}\right] \tag{3.3-51}$$

Note that the exit aperture basis vectors form the identity matrix.

The RTA magnification scales the off-axis components of the viewing vector by the magnification factor m. The specified VIIRS RTA magnification factor is m = 4. The specified aft optics effective focal length is f = 285.25.

$$\mathbf{M}_{mag} = \begin{bmatrix} \frac{1}{m} & 0 & 0 \\ 0 & \frac{1}{m} & 0 \\ 0 & 0 & 1 \end{bmatrix} \tag{3.3-52}$$

3.3.2.1.8. Generation of the Object Viewing Vector

This section summarizes the generation of an object-viewing vector. For any focal plane location (x,y) the following can be used to generate an object space viewing vector $\mathbf{u}_{\text{inst}}$ in the instrument coordinate system at time *t*. Typically, the focal plane location will be the center of a spatial element or detector and the time *t* will be the time t_{center} when the center of the sample was imaged.

1. Generate the image space-viewing vector $\mathbf{u}_{foc}$ in focal plane coordinates from the focal plane location (x,y) and the focal length *f*. (Note: this is static and can be pre-computed and stored in a sensor specific geolocation parameter file.)

$$\mathbf{u}_{foc} = \begin{bmatrix} x & y & f \end{bmatrix}^t \tag{3.3-53}$$

The x component of the $\mathbf{u}_{foc}$ vector is given by equations 3.3-19 & 3.3-19a, and the y component is given by equation 3.3-19 for the Moderate and Imagery bands. The x and y components of the $\mathbf{u}_{foc}$ vector vary as a function of aggregation zone for the DNB band, since the parameters x_{space} and y_{space} vary as a function of DNB aggregation zone. The modified 3.3-19 equations for the DNB band are given by:

$$\begin{aligned} x_i &= x_{\text{res}i} - B_{pos} * x_{\text{space}} - 0.5 * x_{\text{DNB\_space}}(DNB\_agg\_zone) \\ y_i &= y_{\text{cen}} + y_{\text{DNB\_space}}(DNB\_agg\_zone)\left[\tfrac{1}{2}(N_{\text{det}}+1) - i\right] + y_{\text{res}i} \end{aligned} \tag{3.3-53A}$$

Where:

x_{space} - Spacing between MOD detectors in scan direction

$x_{\text{DNB\_space}}$ - Spacing between DNB detectors in the scan direction, dependent on DNB aggregation zone

$y_{\text{DNB\_space}}$ - Spacing between DNB detectors in the track direction, dependent on DNB aggregation zone

Note that N_{samp} = 1 for DNB and f_j = f_0 so these terms drop out of equation 3.3-19a to yield equation 3.3-51a for the x-component of the DNB u_aft vector.

2. Transform the view vector from the focal plane to the aft optics coordinate system. (Note: this is static and can be pre-computed using equation 3.3-1 and then stored in an instrument specific geolocation parameter file.)

$$\mathbf{u}_{aft} = \mathbf{T}_{aft/foc}\mathbf{u}_{foc} \tag{3.3-54}$$

3. Compute the RTA encoder position n_{encT} at time *t*.

$$n_{\text{enc}} = f_{\text{enc}}\left(t, \mathbf{n}_{\text{encT}}, \mathbf{t}_{\text{pulse}}\right) \tag{3.3-55}$$

4. Compute the RTA angle θ_T from the RTA encoder position n_{encT}:

$$\theta_T = A_0^T + A_1^T n_{\text{encT}} + A_2^T n^2{}_{\text{encT}} + \ldots \tag{3.3-56}$$

5. Compute the HAM encoder position n_{encH} at time *t*.

$$n_{\text{enc}} = f_{\text{enc}}\left(t, \mathbf{n}_{\text{encH}}, \mathbf{t}_{\text{pulse}}\right) \tag{3.3-57}$$

6. Compute the HAM angle θ_{HA} from the HAM encoder position n_{enc}:

$$\theta_{HA} = A_0^H + A_1^H n_{\text{enc}} + A_2^H n^2{}_{\text{enc}} + \ldots \tag{3.3-58}$$

7. Compute the HAM normal vector $\hat{\mathbf{n}}_{\text{HA}}$ using the HAM angle θ_{HA} and the normal $\hat{\mathbf{n}}_{\text{side}\,i}$ for the appropriate mirror side *i*.

$$\hat{\mathbf{n}}_{\text{HA}} = \mathbf{T}_{\text{rot}}\left(\theta_{HA}\right)\hat{\mathbf{n}}_{\text{side}\,i} \tag{3.3-59}$$

where $\mathbf{T}_{\text{rot}}\left(\theta_{HA}\right)$ is computed using equation (3.3-31) and $\hat{\mathbf{n}}_{\text{side}\,i}$ is computed using equations (3.3-29) and (3.3-30).

8. Transfer the HAM normal vector from the HA mirror to the instrument coordinate system using a pre-determined sensor specific $\mathbf{T}_{\text{inst/HA}}$ and then normalize it:

$$\mathbf{n}_{\text{mirr}} = \mathbf{T}_{\text{inst/HA}}\hat{\mathbf{n}}_{\text{HA}} \quad \hat{\mathbf{n}}_{\text{mirr}} = \frac{\mathbf{n}_{\text{mirr}}}{\left|\mathbf{n}_{\text{mirr}}\right|} \tag{3.3-60}$$

9. Transfer the viewing vector from the aft optics to instrument coordinate system using the static transformation matrix $\mathbf{T}_{\text{inst/aft}}$ and the viewing vector in the aft optics coordinate system $\mathbf{u}_{\text{aft}}$:

$$\mathbf{u}_{\text{HA}} = \mathbf{T}_{\text{inst/aft}}\mathbf{u}_{\text{aft}} \tag{3.3-61}$$

[Note: see Eq. (3.3-4) for $\mathbf{T}_{\text{inst/aft}}$ and Eq.(3.3-54) for $\mathbf{u}_{\text{aft}}$]

10. Reflect the viewing vector $\mathbf{u}_{\text{HA}}$ off the mirror to generate the viewing vector $\mathbf{u}_{\text{tel}}$ at the telescope entrance aperture:

$$\mathbf{u}_{\text{tel}} = \mathbf{u}_{\text{HA}} - 2\hat{\mathbf{n}}_{\text{mirr}}\left(\mathbf{u}_{\text{HA}} \cdot \hat{\mathbf{n}}_{\text{mirr}}\right) \tag{3.3-62}$$

11. Project the incoming viewing vector onto the entrance aperture basis vectors by premultiplying by $\mathbf{M}_{in}^{T}(\theta_T)$:

$$\mathbf{u}_{\text{in}} = \mathbf{M}_{in}^{T}(\theta_T)\mathbf{u}_{\text{tel}} \tag{3.3-63}$$

where $\mathbf{M}_{in}$ is given by equation (3.3-50).

12. Apply the magnification factor and reconstruct the object space viewing vector:

$$\mathbf{u}_{\text{inst}} = \mathbf{M}_{out}(\theta_T)\mathbf{M}_{mag}\mathbf{u}_{\text{in}} = \mathbf{u}_{\text{tel}}\mathbf{M}_{out}(\theta_T)\mathbf{M}_{mag}\mathbf{M}_{in}^{T}(\theta_T)\mathbf{u}_{tel} \tag{3.3-64}$$

where $\mathbf{M}_{\text{out}}$ is given by equation (3.3-51). The magnification factor is used to pre-compute $\mathbf{M}_{\text{mag}}$ (see equation (3.3-52)).

3.3.2.2. Geolocation Algorithm

The VIIRS geolocation algorithm computes the Earth location and derived parameters for a viewing vector. Three subsections describe this calculation: the standard algorithm for intersection with the Earth ellipsoid; the terrain intersection algorithm; and the algorithm to generate the satellite, solar, and lunar viewing angles and the satellite range.

3.3.2.2.1. Basic Earth Ellipsoid Intersection Algorithm

Given an object viewing vector $\mathbf{u}_{\text{inst}}$ in the instrument coordinate system and a corresponding time *t*, the basic Earth ellipsoid intersection algorithm proceeds as follows:

1. Compute the required coordinate transformations:

   1a. Get instrument-to-spacecraft alignment matrix $\mathbf{T}_{\text{sc/inst}}$ (see Eq. (3.3-7). [Construct the instrument-to-spacecraft alignment matrix based on the time *t* if a time varying model is needed.]

   1b. Interpolate the spacecraft attitude to time *t* and construct the spacecraft to orbital coordinate transformation matrix $\mathbf{T}_{\text{orb/sc}}$ (see Eq. (3.3-8).

   1c. Interpolate the ECI spacecraft position $\mathbf{P}_{\text{eci}}$ and velocity $\mathbf{V}_{\text{eci}}$ to time *t* and

construct the orbital to ECI transformation matrix $\mathbf{T}_{\text{eci/orb}}$ (see Eq. (3.3-12).

1d. Construct the ECI to ECEF rotation matrix $\mathbf{T}_{\text{ecef/eci}}$ from the sampling time *t*.

1e. Construct the composite transformation matrix:

$$\mathbf{T}_{\text{ecef/inst}} = \mathbf{T}_{\text{ecef/eci}}\mathbf{T}_{\text{eci/orb}}\mathbf{T}_{\text{orb/sc}}\mathbf{T}_{\text{sc/inst}} \tag{3.3-65}$$

2. Transform the viewing vector and spacecraft position vector to the ECEF coordinate system:

2a. Rotate the viewing vector $\mathbf{u}_{\text{inst}}$ to the ECEF coordinate system:

$$\mathbf{u}_{\text{ecef}} = \mathbf{T}_{\text{ecef/inst}}\,\mathbf{u}_{\text{inst}} \tag{3.3-66}$$

2b. Rotate the spacecraft position vector to the ECEF coordinate system:

$$\mathbf{p}_{\text{ecef}} = \mathbf{T}_{\text{ecef/eci}}\,\mathbf{p}_{\text{eci}} \tag{3.3-67}$$

3. Intersect the ECEF viewing vector with the WGS84 Earth ellipsoid (Figure 3.3-23). Note: These equations do not account for the travel time of light or for aberration due to spacecraft motion or relativistic effects. These effects cause a systematic bias of 7 m at nadir and 14 m at the edges of the scans,

3a. Re-scale the viewing vector and satellite vector using the ellipsoid semi-major *a* and semi-minor *b* axis dimensions (*a, a, b*):

$$\mathbf{u}' = \begin{bmatrix} u_1/a \\ u_2/a \\ u_3/b \end{bmatrix} \quad \mathbf{p}' = \begin{bmatrix} p_1/a \\ p_2/a \\ p_3/b \end{bmatrix} \tag{3.3-68}$$

Note:

$$\mathbf{x}' = \begin{bmatrix} x_1/a \\ x_2/a \\ x_3/b \end{bmatrix} \text{ - the unknown ground point vector (re-scaled)} \tag{3.3-69}$$

3b. Solve for the scaling *d* of $\mathbf{u}'$ which intersects the unit sphere.

From the law of cosines:

$$|\mathbf{x}'|^2 = |d\,\mathbf{u}'|^2 + |\mathbf{p}'|^2 - 2\,|d\,\mathbf{u}'|\,|\mathbf{p}'|\cos(w) \tag{3.3-70}$$

Using the dot-product, the cosine of the acute angle *w* between $\mathbf{u}'$ and $-\mathbf{p}'$ is:

$$\cos(w) = -(\mathbf{u}'\cdot\mathbf{p}')/(|\mathbf{u}'||\mathbf{p}'|) \tag{3.3-71}$$

By definition $|\mathbf{x}'| = 1$ so:

$$1 = d^2|\mathbf{u}'|^2 + |\mathbf{p}'|^2 + 2d|\mathbf{u}'||\mathbf{p}'|(\mathbf{u}'\cdot\mathbf{p}')/(|\mathbf{u}'||\mathbf{p}'|) \tag{3.3-72}$$

Simplifying and rearranging:

$$d^2|\mathbf{u}'|^2 + 2d(\mathbf{u}'\cdot\mathbf{p}') + |\mathbf{p}'|^2 - 1 = 0 \tag{3.3-73}$$

This can be solved for *d* using the quadratic formula:

$$d = \frac{-(\mathbf{u}'\cdot\mathbf{p}') - \sqrt{(\mathbf{u}'\cdot\mathbf{p}')^2 - |\mathbf{u}'|^2(|\mathbf{p}'|^2 - 1)}}{|\mathbf{u}'|^2} \tag{3.3-74}$$

This is the smaller of the two solutions for *d*, the intersection closest to the satellite. If the solution is not real, then there is no intersection.

3c. Use *d* to compute $\mathbf{x}'$ and $\mathbf{x}$:

$$\mathbf{x}' = \mathbf{p}' + d\,\mathbf{u}' \tag{3.3-75}$$

$$\mathbf{x} = \begin{bmatrix} x'_1\,a \\ x'_2\,a \\ x'_3\,b \end{bmatrix} = \begin{bmatrix} (p'_1 + d\,u'_1)a \\ (p'_2 + d\,u'_2)a \\ (p'_3 + d\,u'_3)b \end{bmatrix} = \begin{bmatrix} p'_1\,a + d\,u'_1\,a \\ p'_2\,a + d\,u'_2\,a \\ p'_3\,b + d\,u'_3\,b \end{bmatrix} \tag{3.3-76}$$

$$\mathbf{x} = \mathbf{p} + d\,\mathbf{u} \tag{3.3-77}$$

4. Convert the ECEF ellipsoid pierce point to geodetic coordinates (special case direct solution):

$$lon = \tan^{-1}\left(\frac{x_2}{x_1}\right) \tag{3.3-78}$$

$$lat = \tan^{-1}\left(\frac{x_3/(1-e^2)}{\sqrt{x_1^2 + x_2^2}}\right) \tag{3.3-79}$$

$$h = 0 \tag{3.3-80}$$

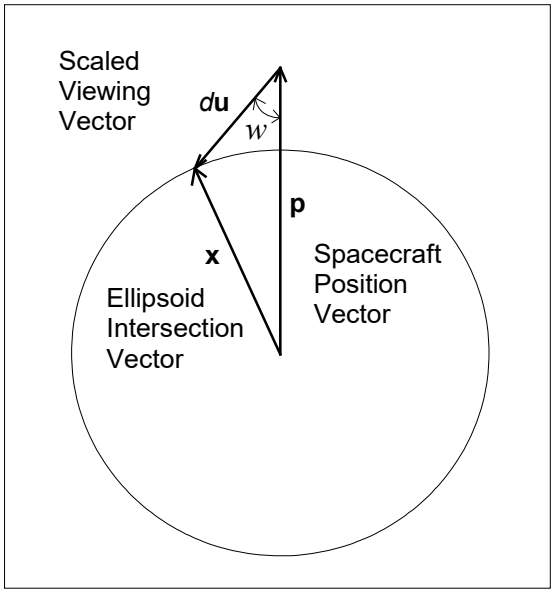

Figure 3-23: Ellipsoidal Viewing Vector Intersection

3.3.2.2.2. Terrain Intersection Algorithm

The terrain intersection algorithm refines the earth ellipsoid intersection to account for the local terrain parallax. The method uses the ECEF coordinate system and geodetic coordinate system and obtains geodetic coordinates where the view vector from the satellite intersects the terrain.

1. Compute the local ellipsoid normal unit vector from the geodetic latitude and longitude at **x** on the Eart ellipsoid:

$$\hat{\mathbf{n}} = \begin{bmatrix} \cos(lat)\cos(lon) \\ \cos(lat)\sin(lon) \\ \sin(lat) \end{bmatrix} \tag{3.3-81}$$

2. Compute the ECEF unit vector from the ground point **x** to the satellite:

$$\hat{\mathbf{u}} = -\frac{\mathbf{u}}{|\mathbf{u}|} \tag{3.3-82}$$

3. Compute the component of the satellite vector that is in the local vertical direction:

$$\cos(\nu) = \hat{\mathbf{u}} \cdot \hat{\mathbf{n}} \tag{3.3-83}$$

4. Compute the distance along the satellite vector ($D_{\max}$) we must move to achieve a height of $H_{\max}$ where $H_{\max}$ is a pre-computed value representing the highest local terrain height:

$$D_{\max} = \frac{H_{\max}}{\cos v} \tag{3.3-84}$$

5. Compute the ECEF coordinates of the point along the viewing vector that corresponds to $H_{\max}$:

$$\mathbf{x}_{\max} = \mathbf{x} + D_{\max}\hat{\mathbf{u}} \tag{3.3-85}$$

6. Compute the distance along the satellite vector ($D_{\min}$) we must move to achieve a height of $H_{\min}$ where $H_{\min}$ is a pre-computed value representing the lowest local terrain height:

$$D_{\min} = \frac{H_{\min}}{\cos v} \tag{3.3-86}$$

7. Compute the ECEF coordinates of the point along the viewing vector that corresponds to $H_{\min}$:

$$\mathbf{x}_{\min} = \mathbf{x} + D_{\min}\hat{\mathbf{u}} \tag{3.3-87}$$

8. Convert $\mathbf{x}_{\max}$ to geodetic coordinates (iterative general solution), with coordinates (ϕmax, λmax, Hmax)
9. Define points $\mathbf{s}_{\max}$ on the ellipsoidal surface from point $\mathbf{x}$max by: (ϕmax, λmax, 0)
10. Perform terrain intersection iterations (see Figure 3.3-24):

$$\mathbf{s}_0 = \mathbf{s}_{\max} = (\phi_{\max}, \lambda_{\max}, 0) \text{ - (Geodetic Coordinates)} \tag{3.3-88}$$

$$h_0 = \mathrm{DEM}(\mathbf{s}_0) \tag{3.3-89}$$

where DEM is height above ellipsoid, which is a combination of geoid height and terrain height.

$$h'_0 = H_{\max} \tag{3.3-90}$$

$$ds = (\text{nominally } 1/2 \text{ km}) \tag{3.3-91}$$

$$dD = \frac{ds}{\sin v} \tag{3.3-92}$$

$$i = 0 \tag{3.3-93}$$

$$D_0 = D_{\max} \tag{3.3-94}$$

do until
$(h_i \geq h'_i)$ (3.3-95)

$$i = i+1 \tag{3.3-96}$$

$$D_i = D_{i-1} - dD \tag{3.3-97}$$

$$\mathbf{x}_i = \mathbf{x} + D_i \hat{\mathbf{u}} \tag{3.3-98}$$

$$\mathbf{x}_i \Rightarrow (\phi_i, \lambda_i, h_i) \text{ - (Convert from ECEF to geodetic)} \tag{3.3-99}$$

$$\mathbf{s}_i = (\phi_i, \lambda_i, 0) \tag{3.3-100}$$

$$h_i = \text{DEM}(\mathbf{s}_i) \tag{3.3-101}$$

end do

$$D = D_i \tag{3.3-102}$$

11. Compute the precise terrain intersection from the last two iterations. The final terrain intersection height can be expressed:

$$h_{\text{final}} = \alpha h_i + (1-\alpha) h_{i-1} = \alpha h'_i + (1-\alpha) h'_{i-1} \tag{3.3-103}$$

Solving for the weights with $dh' = (h'_i - h'_{i-1})$,

$$\alpha = \frac{h'_{i-1} - h_{i-1}}{h_i - h_{i-1} - dh'}$$
$$1 - \alpha = \frac{h_i - h'_i}{h_i - h_{i-1} - dh'} \tag{3.3-104}$$

The final position is:

$$D_{\text{final}} = D + (1-\alpha) dD \tag{3.3-105}$$

$$\bar{\mathbf{x}} = \mathbf{x} + D_{\text{final}} \hat{\mathbf{u}}$$
$$\Rightarrow (\phi_{final}, \lambda_{final}, h') \text{ - (Convert from ECEF to geodetic)} \tag{3.3-106}$$

$$h_{\text{final}} = \alpha h_i + (1-\alpha) h_{i-1} \tag{3.3-107}$$

12. Final geodetic coordinates (*lat, lon, height*) on the terrain are given by: $(\phi_{\text{final}}, \lambda_{\text{final}}, h_{final})$. Care must be taken, so that ds is in sync with the resolution of the DEM; otherwise, tops of steep mountains at large scan angles might be missed.

The database used for performing the terrain correction is the 30 arc-second SDPTK DEM. Height information is retrieved from the DEM database by performing linear interpolation to the specified geographic location from the four nearest-neighbor DEM data points using the SDPTK software. Both height of the geoid relative to the WGS84 ellipsoid and height of the terrain relative to the geoid can be retrieved using the SDPTK.

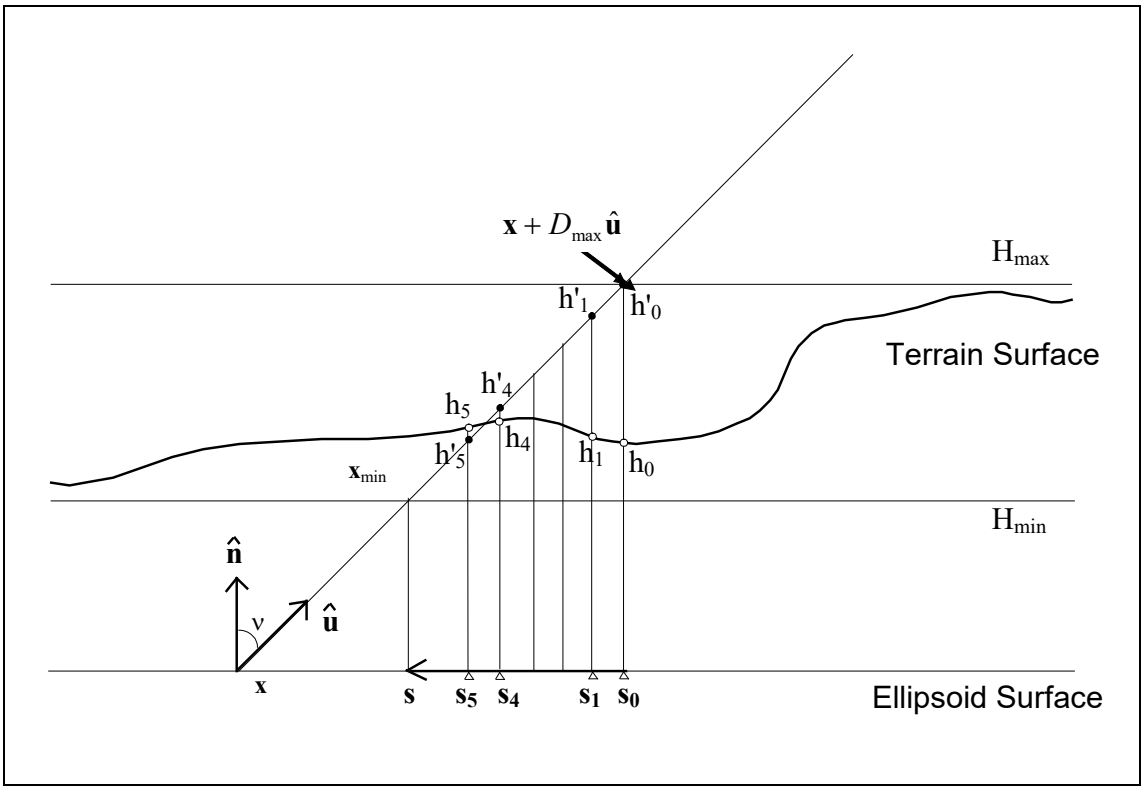

Figure 3-24: Terrain Intersection Search Geometry

3.3.2.2.3. Computing Additional Parameters

The remaining derived parameters can now be calculated from the final geodetic coordinates. These parameters are the zenith and azimuth angles to the satellite, the range to the satellite and the zenith and azimuth angles to the Sun and Moon. Also, solar vectors and, in the case of the DNB lunar vectors and lunar phase are provided, which are useful in the instrument calibration and necessary for the production of Near Constant Contrast (NCC) imagery.

Given the final geodetic position latitude, longitude and height (φ, λ, h), ECEF coordinates $(x, y, z) = \mathbf{x}_{ecf}$ can be expressed (as given at the beginning of Section 3.3.1.3.10) by:

$$x = (N + h)\cos\varphi\cos\lambda \tag{3.3-108}$$

$$y = (N + h)\cos\varphi\sin\lambda \tag{3.3-109}$$

$$z = (N(1 - e^2) + h)\sin\varphi \tag{3.3-110}$$

$$N = a/(1 - e^2\sin^2\varphi)^{1/2}$$

$$e^2 = 1 - \frac{b^2}{a^2} \tag{3.3-111}$$

1. Compute the unit normal vector $\hat{\mathbf{n}}$ at the final geodetic position (φ,λ,h) by

differentiating equations (3.3-106), (3.3-107), and (3.3-108) with respect to *h* and evaluate at (φ,λ,h):

$$\hat{\mathbf{n}} = \begin{bmatrix} \cos(\varphi)\cos(\lambda) \\ \cos(\varphi)\sin(\lambda) \\ \sin(\varphi) \end{bmatrix} \tag{3.3-112}$$

2. Compute a unit vector $\hat{\mathbf{E}}$ in the east direction at the geodetic position by differentiating equations (3.3-106), (3.3-107), and (3.1-108) with respect to λ and evaluate at the position:

$$\hat{\mathbf{E}} = \begin{bmatrix} -\sin\lambda \\ \cos\lambda \\ 0 \end{bmatrix} \tag{3.3-113}$$

3. Compute a unit vector $\hat{\mathbf{N}}$ in the north direction at the geodetic position by computing the cross product of $\hat{\mathbf{n}}$ and $\hat{\mathbf{E}}$:

$$\hat{\mathbf{N}}=\hat{\mathbf{n}}\times\hat{\mathbf{E}} \tag{3.3-114}$$

4. Generate the range to the spacecraft r_{sc} and the ground to spacecraft unit vector $\mathbf{v}_{sc}$:

$$\begin{aligned} \mathbf{v}_{\mathbf{sc}} &= \mathbf{p}_{\mathbf{ecr}} - \mathbf{x}_{\mathbf{ecr}} \\ r_{sc} &= \left|\mathbf{v}_{\mathbf{sc}}\right| \\ \hat{\mathbf{v}}_{sc} &= \frac{1}{r_{sc}}\mathbf{v}_{sc} \end{aligned} \tag{3.3-115}$$

5. The zenith angle ζ_{sc} is the angle between the spacecraft view vector and the normal:

$$\cos(\zeta_{sc}) = \hat{\mathbf{n}} \cdot \hat{\mathbf{v}}_{sc} \tag{3.3-116}$$

6. Compute the azimuth angle α_{sc}:

   a. Compute two directional cosines by:

$$l = \mathbf{v}_{sc} \cdot \hat{\mathbf{E}} \quad m = \mathbf{v}_{sc} \cdot \hat{\mathbf{N}} \tag{3.3-117}$$

   b. Using the following relationship between the azimuth angle and the directional cosines *l* and *m*, determine the angle.

$$\tan(\alpha_{sc}) = \frac{l}{m} \tag{3.3-118}$$

7. The following steps are used to generate the solar vectors from the ground and from the instrument after retrieving the ECI solar vector $\mathbf{s}_{eci}$ based on the imaging time t.
   a. In the ECEF coordinate system, rotate the solar vector at time t by:

$$\mathbf{s}_{ecr} = \mathbf{T}_{ecr/eci}\mathbf{s}_{eci} \tag{3.3-119}$$

   b. In the instrument coordinate system,

$$\mathbf{s}_{inst} = \mathbf{T}_{inst/sc}\mathbf{T}_{sc/orb}\mathbf{T}_{orb/eci}\mathbf{s}_{eci} \tag{3.3-120}$$

8. The following steps are used to generate the lunar vector $\mathbf{m}_{inst}$ from the spacecraft in the instrument coordinate system after retrieving the ECI lunar vector $\mathbf{m}_{eci}$ based on the time t. In the instrument coordinate system,

$$\mathbf{m}_{inst} = \mathbf{T}_{inst/sc}\mathbf{T}_{sc/orb}\mathbf{T}_{orb/eci}\mathbf{m}_{eci} \tag{3.3-121}$$

9. The following lunar phase algorithm produces the cosine of the lunar phase angle:

$$\cos Q_{phase} = (R_{ms} \bullet R_{mb})/(r_{ms} r_{mb}) \tag{3.3-122}$$

   where R_{ms} is the moon to sun range vector, R_{mb} is the moon to ground pixel point vector, r_{ms} is the scalar moon to sun distance, and r_{mb} is the moon to ground pixel point distance.

   This algorithm uses a computed solar vector and the computed lunar vector. Lunar phase only needs to be determined once per execution of the VIIRS Geolocation algorithm.

3.3.3. Archived Algorithm Output

The geolocation algorithm creates the following output fields for each moderate resolution, imagery resolution and DNB pixel: geodetic latitude, longitude, height above the Earth ellipsoid, satellite zenith angle, satellite azimuth, range to the satellite, solar zenith angle, solar azimuth, lunar zenith angle (DNB only), and lunar azimuth (DNB only). A VIIRS scan without “bow-tie deletion” contains 3200 x 16 = 51200 ‘M’ band pixels, 6400 x 32 = 204800 ‘I’ band pixels, and 4064 x 16 = 65024 DNB pixels. “Bow-tie deletion” onboard VIIRS reduces the total “M’ band Earth view pixels to 44608/scan and the total ‘I’ band Earth View pixels to 178432/scan.

Therefore, algorithm output will consist of 2,698,240 values per Earth sector scan of which 2,434,560 (90.2%) are for pixels with reported scene values. Quality information may be

stored separately, which add to this volume, or may use unused bits within the reported fields.

3.4. ERROR ANALYSIS AND SENSITIVITY STUDIES

The error analysis and sensitivity studies section was written at the time of the original publication of the VIIRS Geo ATBD. The intent of this section was to present a snapshot of the error analysis using the current best estimates at the time of the initial publication. Coding of the VIIRS geolocation algorithm is not dependent on this section for either its software requirements or design.

3.4.1. Variance or Uncertainty Estimates

The fundamental measure of uncertainty of interest for the Earth location algorithm is the location accuracy of the geodetic coordinates computed for each spatial element. This accuracy is limited by the uncertainty in the spacecraft, instrument, and elevation data provided to the algorithm.

An analysis of VIIRS Earth location error is presented in this and the following sections. This analysis includes a detailed breakdown of the anticipated sources of error in the NPOESS spacecraft ephemeris and attitude knowledge, and in the VIIRS instrument pointing knowledge. It also demonstrates the effects these errors and errors in the ancillary digital elevation data have on the resulting data product Earth location accuracy. The current best estimates of the contributing errors from the VIIRS instrument error budget were used in conjunction with the spacecraft specification requirements for this analysis.

The sensitivity of the output product accuracy to the uncertainty in the input data varies with scan angle. Plots depicting this sensitivity for spacecraft position, spacecraft attitude pointing, and instrument pointing knowledge errors are presented in Section 3.4.2.

The three error components, spacecraft position, spacecraft attitude, and instrument pointing knowledge, were analyzed separately with all contributing errors classified as either static or dynamic. Static errors are unknown constant or repeatable periodic offsets caused by imprecise knowledge of the instrument or spacecraft geometry, or by geometric distortions occurring before or in-flight. These error components, though initially unknown, should not change with time in-flight. Estimates of these constant offsets or biases will be computed using the geometric parameter estimation and algorithm verification procedures described in Section 3.6.1. The dynamic error components are time varying and cannot be easily modeled. Tables detailing the various error sources and their expected magnitudes are presented in Section 3.4.3. Table 3.4-1, Table 3.4-2, and Table 3.4-3 summarize the impact on Earth location of the various error sources. Two cases are shown in each table: the current design before on-orbit calibration case; and the after on-orbit calibration case. Table 3.4-4 shows the combined effect (Root Sum Square (RSS)) of all of the components.

Table 3.4-1: Geolocation Impact of 3 Sigma Spacecraft Position Errors

Spacecraft Position	X-Axis Platform	Corresponding Along-Track Earth Location Error		Y-Axis Platform	Corresponding Along-Scan Earth Location Error		Z-Axis Platform	Corresponding Along-Scan Earth Location Error	
	Position Error	scan = 0°	scan = 55°	Position Error	scan = 0°	scan = 55°	Position Error	scan = 0°	scan = 55°
Before Calibration	75.0 m	66.4 m	64.5 m	75.0 m	66.4 m	66.4 m	75.0 m	0.0 m	177.9 m
After Calibration	75.0 m	66.4 m	64.5 m	75.0 m	66.4 m	66.4 m	75.0 m	0.0 m	177.9 m

Table 3.4-2: Geolocation Impact of 3 Sigma NPOESS Platform Attitude Knowledge Error Components

Platform Attitude	Roll Pointing Error	Corresponding Along-Scan Earth Location Error		Pitch Pointing Error	Corresponding Along-Track Earth Location Error		Yaw Pointing Error	Corresponding Along-Track Earth Location Error	
		scan = 0°	scan = 55°		scan = 0°	scan = 55°		scan = 0°	scan = 55°
Before Calibration	56.7 arcsec	228.2 m	1417.4 m	67.7 arcsec	272.4 m	330.6 m	61.6 arcsec	0.0 m	446.3 m
After Calibration	36.8 arcsec	148.1 m	919.7 m	36.8 arcsec	148.1 m	179.7 m	36.8 arcsec	0.0 m	266.5 m

Figure 3.4-1 and Figure 3.4-2 show these combined Earth location errors graphically. In the first figure, the four error ellipses correspond to the two cases at two different scan angles, 0 and 55 deg with the error given in meters. The second figure shows plots of Earth location error growth, in the along-track and across-track directions, as a function of distance from nadir for the after-calibration case.

Table 3.4-3: Geolocation Impact of 3 Sigma Instrument Pointing Knowledge Error Components

Instrument Pointing	Roll Pointing Error	Corresponding Along-Scan Earth Location Error		Pitch Pointing Error	Corresponding Along-Track Earth Location Error		Yaw Pointing Error	Corresponding Along-Track Earth Location Error	
		scan = 0°	scan = 55°		scan = 0°	scan = 55°		scan = 0°	scan = 55°
Before Calibration	144.7 arcsec	582.3 m	3616.1 m	144.7 arcsec	582.1 m	706.5 m	154.5 arcsec	0.0 m	1118.9 m
After Calibration	27.6 arcsec	111.2 m	690.4 m	29.6 arcsec	119.0 m	144.4 m	31.9 arcsec	0.0 m	230.6 m

Table 3.4-4: Total Combined 3 Sigma RSS Geolocation Error

	Total RSS Along-Scan Earth Location Error (3 sigma) (Y-Axis Spacecraft Position) (Z-Axis Spacecraft Position) (Platform Roll) (Instrument Roll)		Total RSS Along-Track Earth Location Error (3 sigma) (X-Axis Spacecraft Position) (Platform Pitch) (Instrument Pitch) (Platform Yaw) (Instrument Yaw)		Equivalent Circular Error (3 sigma) (Equal Area Circle Radius)	
	scan = 0°	scan = 55°	scan = 0°	scan = 55°	scan = 0°	scan = 55°
Before Calibration	628.9 m	3888.6 m	646.1 m	1436.6 m	637.5 m	2363.5 m
After Calibration	196.7 m	1165.6 m	201.2 m	426.1 m	199.0 m	704.7 m

The accuracy impact of the digital elevation data is also a function of scan angle with no effect on Earth location at nadir and a greater than one-to-one correspondence between height and position errors at high scan angles. Figure 3.4-3 shows the impact of two different terrain accuracies on the Earth location accuracy in fractions of a pixel (in the along-scan direction). The discontinuities in these plots are due to the changes in pixel aggregation factor in the along-scan direction. In each graph, the Earth location error in pixel fraction reaches a peak and drops down after that point. Although both the Earth location error and ground pixel size increase as the scan angle increases, the rate of increase in the pixel size is slower than the rate of increase in the Earth location error close to nadir, but becomes faster at higher scan angles where the ratio begins to decrease. See Figure 3.3-1 for growth of the pixel size on the ground. In the context of image-to-image registration, the displacement due to terrain errors is self-canceling if the two data sets are taken from approximately the same viewing geometry but are arithmetically added if the views are from different directions. The effect of the input elevation model on the product accuracy is further complicated by the relationship between elevation accuracy and terrain roughness. In rugged areas, elevation variations of hundreds of meters can occur within a single VIIRS spatial element. Assigning a single geodetic coordinate to such a spatial element using a representative elevation masks the true complexity of the terrain and the real differences in what is being viewed from different directions.

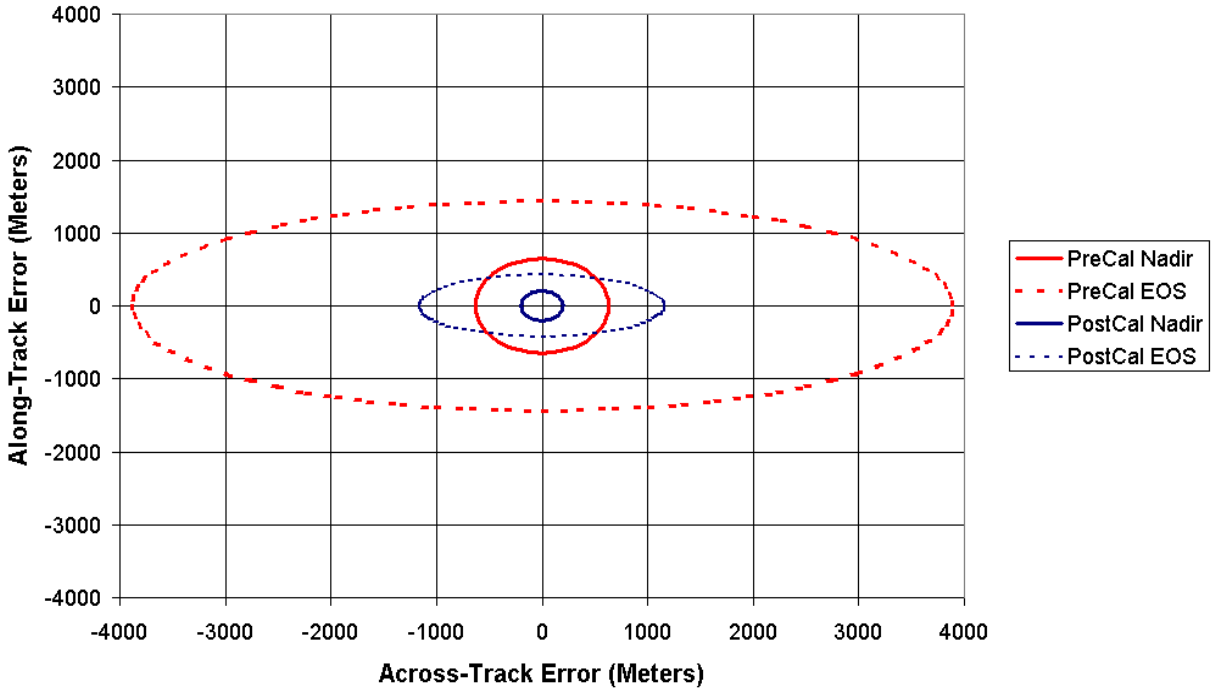

Figure 3-25: 3 Sigma Earth Location Error (Meters)

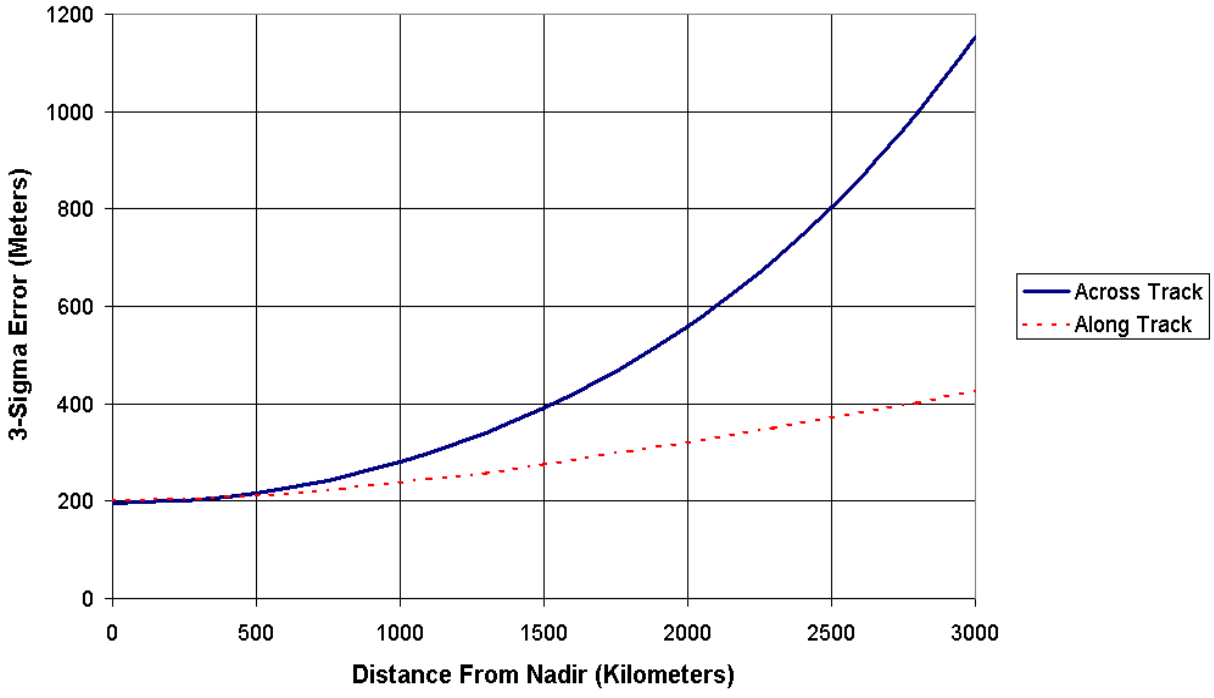

Figure 3-26: Earth Location Error Growth

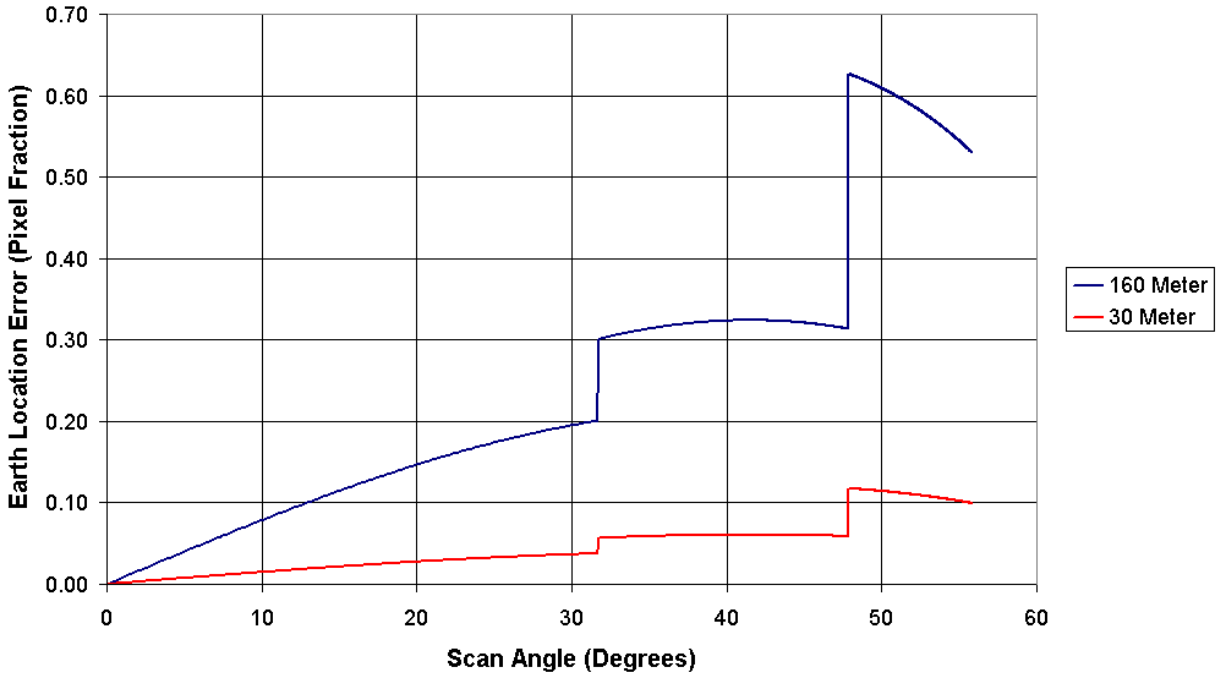

Figure 3-27: Location Error (in imagery band pixel fraction) Resulting from Various Terrain Height Errors as a Function of Scan Angle

Section 3.4.2 relates Platform position, Platform attitude, and Instrument pointing errors to Earth location error. The distortion (or growth) of VIIRS pixels as a function of scan angle is also shown. Section 3.4.3 describes the position and attitude errors specific to the NPOESS Platform and the pointing errors specific to the VIIRS Instrument. Two sets of data are provided. The first is the current at-launch error budget specification limit for each type of error. This is followed by an estimate of actual on-orbit performance following a post-launch calibration activity. The error estimates are separated into component parts and characterized as being either static or dynamic in nature. Section 3.4.4 presents the total combined Earth location error due to specific NPOESS Platform and VIIRS Instrument position, attitude, and pointing errors. Earth location error summary information is presented for both the at-launch and post-calibration Platform/ Instrument scenarios:

- Platform/Instrument errors are at the at-launch specification (or spec) limits
- Platform/Instrument errors are at the reduced estimates based on the degree to which ground processing is able to remove static error components.

Section 3.4.6 provides more details on ground processing, the approach, error characteristics, and limitations. Section 3.4.7 contains a discussion of the effect of inadequate terrain height information on pixel location as a function of scan angle. Section 3.4.8 a summary of geolocation error and Section 3.4.9 discusses error analysis algorithms.

3.4.2. Earth Location Sensitivity to Position/Pointing Error

This section will relate the units of spacecraft position error (meters in space) and platform attitude/instrument pointing error (arc seconds) to absolute geolocation error (meters on the ground). Earth location errors are scan angle dependent, growing larger with increasing scan (or view) angle. A prefacing section describes the corresponding growth of the viewed ground pixel, which also increases in size with increasing scan angle.

3.4.2.1. Pixel and Scan Growth as a Function of Scan Angle

Figure 3.3-1 depicts the growth of a moderate resolution band pixel as a function of scan angle. In the figure the lighter continuous line shows along-track growth while the darker line depicts cross-track growth. For example, a moderate resolution band pixel viewed at a scan angle of 56.063 degrees would have dimensions of 1.60 kilometers cross-track by 1.60 kilometers along-track. The discontinuities in the cross-track plot are due to the changes in pixel aggregation described in Section 3.3. Many of the plots that follow show increasing absolute geolocation error for increasing scan angle. However, pixel size is also (piece-wise) increasing and thus the error expressed as a pixel fraction is less variable.

Since the VIIRS along-track field of view is designed to collect sixteen moderate resolution band pixels at one time, the along-track dimension of the VIIRS scan also grows as a function of scan angle from 11.87 kilometers at nadir to 25.60 kilometers at a scan angle of 56.063 degrees. This leads to the so-called "bow tie" effect in the ground projection of a VIIRS scan in which the scan coverage is wider at the edges than at the center. This effect causes adjacent scans to overlap at high scan angles, with a maximum overlap over 50 percent at 56.063 degrees. This overlap is unaffected by the VIIRS pixel aggregation strategy which applies only in the cross-track direction. The overlap in coverage for two consecutive VIIRS scans is depicted in Figure 2.2-12. The two scans are shown with solid and dashed lines.

Several consequences of this VIIRS imaging geometry should be noted. When viewing VIIRS data in its raw geometric form the images will appear to be discontinuous at the edges where pixels overlap and image features are repeated. This does not affect the Earth location accuracy and the following discussion applies to all VIIRS pixels without regard to how pixels from consecutive scans are spatially related to one another. There is an impact on the way in which VIIRS Earth location data must be computed and stored to correctly represent this geometry.

3.4.2.2. Geolocation Sensitivity to Position Error

The relationship between spacecraft position error and Earth location error is shown in Figure 3.4-4. Two assumptions are made to compute these curves. First, the spacecraft altitude (not including Z-Axis displacement) is taken to be 830 kilometers. Second, a spherical Earth model, with a radius of 6378 kilometers, is used. Terrain variation and non-sphericity of the Earth are second order effects for this part of the analysis.

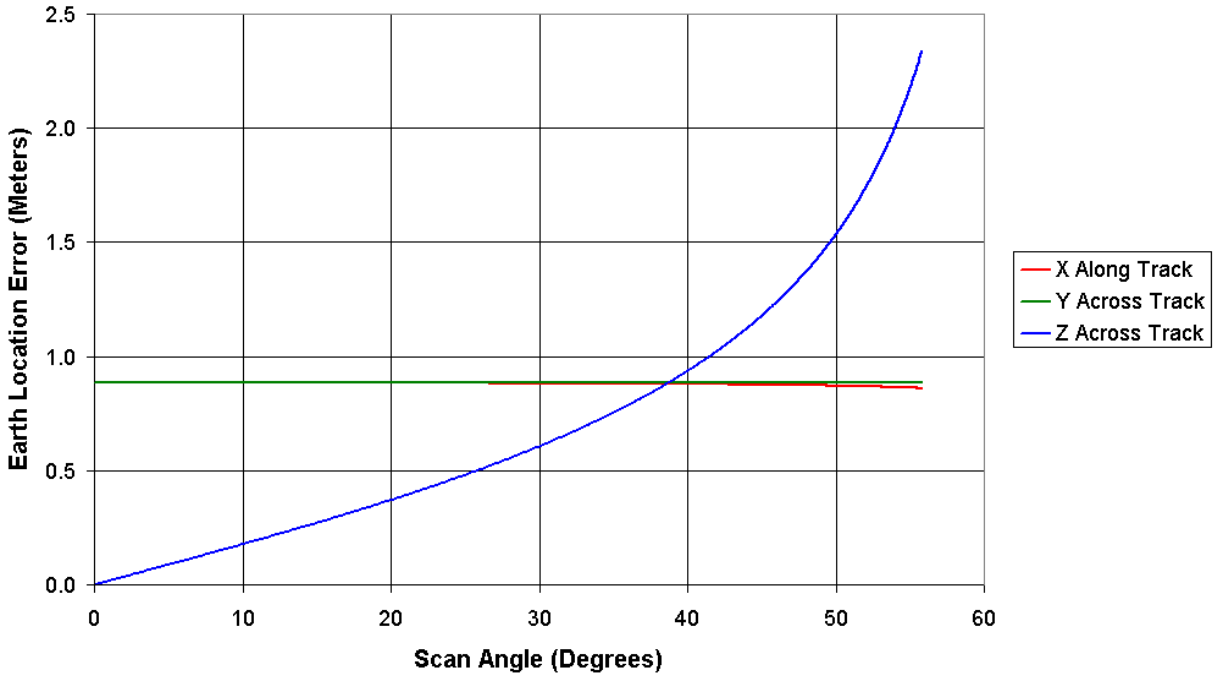

Figure 3-28: Earth Location Error (in meters) resulting from Spacecraft Position Error (in meters) as a Function of Scan Angle

Each curve relates spacecraft position error in meters along a given axis in the Orbital Reference Coordinate Frame to along-track or cross-track Earth location error in meters as a function of scan angle. In this and all subsequent figures, a solid line depicts Earth location errors in the along-track direction, while cross-track Earth location errors are depicted by a dotted line with stars. Spacecraft position errors along the Orbital Reference X-Axis contribute geolocation errors only in the along-track direction. Position errors along the Y and Z-axes contribute geolocation errors only in the cross-track direction.

At nadir (scan angle 0 degrees), a 1.0-meter displacement of the spacecraft along the X-Axis causes an Earth location error of 0.885 meters in the along-track direction as does a 1.0-meter Y-Axis displacement but in the cross-track direction. Spacecraft displacement along the Z-Axis does not impact Earth location at nadir.

At a scan angle of 56.063 degrees, a 1.0-meter X-Axis displacement causes a 0.860 meter along-track Earth location error. A 1.0-meter Y-Axis displacement causes a 0.885-meter cross-track Earth location error. Finally, a 1.0-meter spacecraft displacement along the Z-Axis causes a 2.372-meter cross-track Earth location error. The slight downward dip in the X-Axis displacement curve becomes intuitively obvious when one considers the smaller circle the Earth-surface pixel will traverse during a complete orbit at large scan angle, than at nadir.

3.4.2.3. Geolocation Sensitivity to Attitude/Pointing Error

The relationship between Platform attitude/Instrument pointing error and Earth location error is shown in Figure 3.4-5. The same assumptions of a spherical earth and a 830 km

orbit are made to compute these curves.

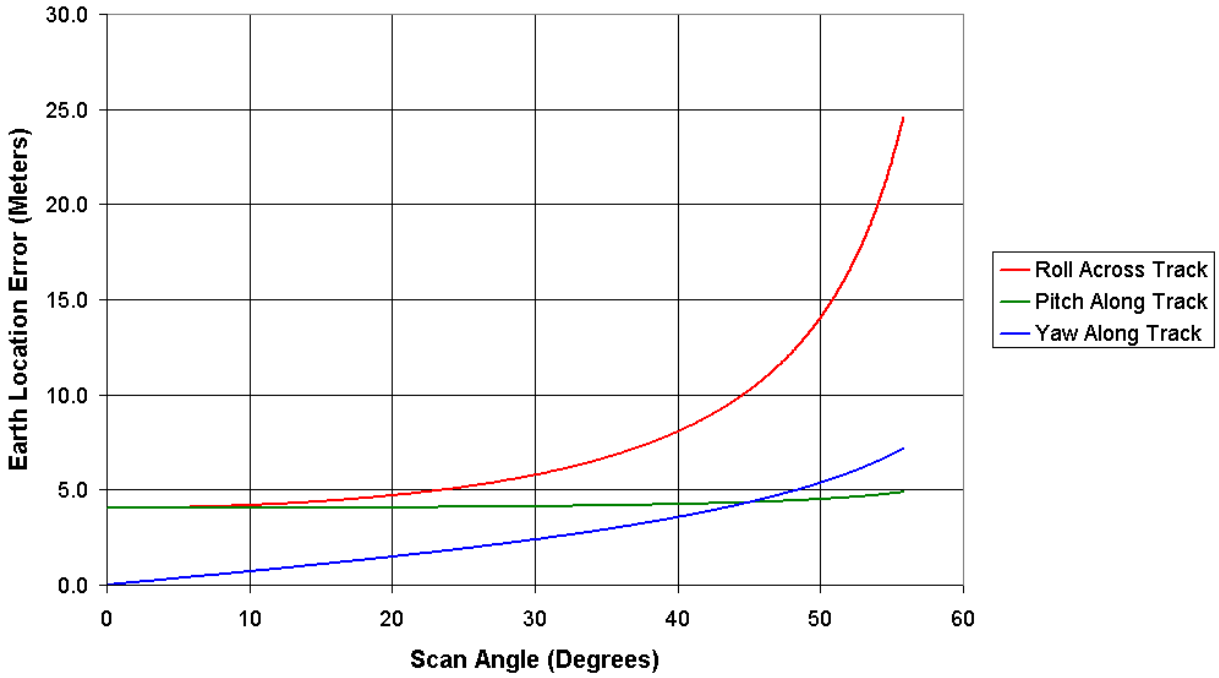

Figure 3-29: Earth Location Error (in meters) resulting from Instrument/Platform Pointing Error (in arcseconds) as a Function of Scan Angle

Each curve relates attitude/pointing error (in arc-seconds) about a given axis in the Orbital Reference Coordinate Frame to along-track or cross-track Earth location error (in meters) as a function of scan angle. Roll pointing errors contribute geolocation errors only in the cross-track direction. Pitch pointing errors contribute geolocation errors only in the along-track direction. Yaw pointing errors effect geolocation primarily in the along-track direction for small angular displacement.

At nadir, a 1 arc-second error in roll causes an Earth location error of 4.024 meters in the cross-track direction. A 1 arc-second error in pitch also causes a 4.024 meter Earth location error, but in the along-track direction. Errors in yaw pointing do not impact Earth location at nadir.

At a scan angle of 56.063 degrees a 1 arc-second error in roll causes a 24.990 meter cross-track Earth location error. A 1 arc-second error in pitch causes a 4.884 meter along-track Earth location error. Finally, a 1 arc-second error in yaw causes a 7.241 meter Earth location error, primarily in the along-track direction.

The large increase in cross-track Earth location error from roll pointing error at high scan angle corresponds to the cross-track distortion of the pixel at high scan angle (see Figure 3.3-1). So the growth in absolute geolocation error from roll pointing error at high scan angles is partially offset by the increase in pixel size so that the error in terms of pixel fraction is more stable.

3.4.3. Position and Attitude Error Specification and Estimation

3.4.3.1. NPOESS Platform Position Error

Platform position errors are specified in meters along 3 axes in the Orbital Reference Coordinate Frame. This coordinate frame moves with the satellite along the space trajectory and defines the orientation of the satellite. The origin of coordinates is at the center of mass of the spacecraft. The positive Z-Axis points from the Spacecraft center of mass to the center of the Earth. The Y-Axis is normal to the Z-Axis and to the Spacecraft's instantaneous velocity vector. The X-Axis completes the right-handed set and is positive in the direction of motion of the satellite. Due to orbit eccentricity, the X-Axis and the Spacecraft's instantaneous velocity vector are not generally co-aligned.

Table 3.4-5 shows the current 3 sigma platform position error specification. The source of information is the VIIRS SRD.

Table 3.4-5: NPOESS Platform Position 3 sigma Error Specification

Spacecraft Position Error	X-Axis Position Error Spec	Y-Axis Position Error Spec	Z-Axis Position Error Spec
3 sigma Spec	75.0 meters	75.0 meters	75.0 meters

Assuming a zero-mean Gaussian distribution, the linear (per coordinate axis) position error requirement implies that 99.7% of the observations would have position errors less than the 3-sigma value (75 meters), 95.5% of the observations would have position errors less than the 2-sigma value (50 meters), and 68.3% of the observations would have position errors less than the 1 sigma value (25 meters).

3.4.3.2. NPOESS Platform Attitude Error

Attitude errors are expressed in terms of two components, attitude accuracy and attitude knowledge. Attitude accuracy is a measurement of the angle between the desired and actual orientation of the Orbital Reference Coordinate Frame (described below) about a given axis. Attitude knowledge is the accuracy of determination of the actual orientation of a given axis of the Orbital Reference Coordinate Frame. For purposes of geolocation, one is more concerned with attitude knowledge than attitude accuracy.

Platform attitude errors are described as rotations about the 3 axes of the Orbital Reference Coordinate Frame in units of arc-seconds. In this report, rotation about the X-Axis is described as Roll, rotation about the Y-Axis is described as Pitch, and rotation about the Z-Axis is described as Yaw. Table 3.4-6 shows the current 3 sigma specification of roll, pitch, and yaw attitude knowledge of the NPOESS Platform at the Instrument Mounting Plate. The information source is the NPOESS SRD. In the SRD the requirement is expressed in terms of separate low (0-10 Hz) and high (> 10 Hz) frequency uncertainties. These have been root sum squared in the table.

Table 3.4-6: NPOESS Platform Attitude Knowledge 3 sigma Error Specification

Platform Attitude Knowledge	Roll Error Spec	Pitch Error Spec	Yaw Error Spec
3 sigma Spec	33.5 arcsecs	33.5 arcsecs	33.5 arcsecs

Table 3.4-7 shows a 3 sigma error budget for the net NPOESS Platform pointing knowledge. This error budget includes the attitude determination component levied on the spacecraft as well as additional terms which effect instrument pointing, based upon experience with the Terra spacecraft, to compile an overall pointing error budget. The errors in this budget were separated into component parts with dynamic error components listed in the first four rows followed by static error components.

Each error term was assumed to be independent with zero-mean Gaussian distribution. Errors within each category were combined by computing the sum of the squares of the component errors then taking the square-root (RSS error). The total RSS dynamic and static errors around each axis are shown towards the bottom of the table. The estimated Platform attitude/pointing error has an approximately equal static/dynamic breakdown.

Table 3.4-7: NPOESS Platform Attitude Knowledge 3 sigma Error Estimates

Platform Attitude Knowledge Error Source	Roll Error Estimate	Pitch Error Estimate	Yaw Error Estimate
DYNAMIC TERMS			
Attitude Determination	33.5 arcsecs	33.5 arcsecs	33.5 arcsecs
Ephemeris Error	2.1	2.1	2.1
Thermal Distortion	15.0	15.0	15.0
STATIC TERMS			
Thermal Distortion	26.1 arcsecs	26.1 arcsecs	26.1 arcsecs
Moisture Distortion	18.0	15.0	15.0
Measurement Error	15.0	15.0	15.0
Gravity Effects	7.5	39.0	15.0
Launch Shift	24.0	24.0	33.0
Total Dynamic (RSS)	36.8 arcsecs	36.8 arcsecs	36.8 arcsecs
Total Static (RSS)	43.2 arcsecs	56.8 arcsecs	49.4 arcsecs
3 sigma Total Combined Allocation	56.7 arcsecs	67.7 arcsecs	61.6 arcsecs

3.4.3.3. VIIRS Instrument Pointing Error

Pointing errors from the VIIRS instrument are also described in terms of pointing accuracy and pointing knowledge. Pointing accuracy is the ability to align the line-of-sight to the target frame. Pointing knowledge is how well one knows the line-of-sight relative to the target. For purposes of geolocation we are concerned with pointing knowledge rather than pointing accuracy.

Instrument pointing errors are described in the same way as Platform pointing errors. It is an angular measurement, in units of arc-seconds, rotated about one of the 3 axes of the Orbital Reference Coordinate Frame. Rotation about the X-Axis is described as Roll pointing error, rotation about the Y-Axis is described as Pitch pointing error, rotation about the Z-Axis is described as Yaw pointing error.

Table 3.4-8 shows the current 3 sigma error estimates for VIIRS pointing knowledge. Once again, pointing errors were broken down into component parts. The expected dynamic error components about each axis are listed in the first 9 rows, the static error components follow. All error terms are assumed to be independent zero-mean Gaussian distributions.

The 3 sigma static terms, in Table 3.4-8, are based on expected worst case scenarios. Once again, errors about each axis and within static or dynamic categories are assumed to be independent with zero-mean Gaussian distributions. The RSS of the error components within each category was computed to give a total dynamic and total static error. The estimated Instrument pointing error is dominated by the static instrument-to-spacecraft alignment uncertainty term. This component can be reduced by on-orbit calibration. The total RSS dynamic and static errors around each axis are shown towards the bottom of Table 3.4-8.

3.4.4. Earth Location Impact

Section 3.4.2 explored the sensitivity of Earth location errors to position and attitude/pointing errors. Section 3.4.3 presented position, attitude, and pointing errors specific to the NPOESS Platform and VIIRS Instrument. In this section, this information is combined, and geolocation errors resulting from specific position/pointing errors of the NPOESS Platform and the VIIRS Instrument are explored.

The component Earth location errors are presented for 2 specific Platform/Instrument cases: the at-launch design, and the post-calibration (static bias removed) case. The at-launch design assumes the Platform and Instrument are built to the current specifications and performance estimates. The post-calibration case assumes that the Platform and Instrument are built to meet the current estimates, the current static error estimates are correct, and that much of this static error is removable through ground processing.

3.4.4.1. Platform Position Error Component Impact

Table 3.4-9 summarizes the Earth location error resulting from the 3 sigma X, Y, and Z-Axis NPOESS Platform position error components. The first column in Table 3.4-9 presents the at-launch design and the second column presents the post-calibration case. The second column is included here for consistency with the tables to follow even though the on-orbit calibration has no effect on platform position knowledge. The first 3 rows show the 3 sigma X-Axis position error and the corresponding Earth location error, in meters. These numbers were computed both at nadir and at scan angle of 56.063 degrees. The middle 3 rows show Y-Axis related errors, and the last 3 rows show Z-Axis related errors.

3.4.4.2. Platform Attitude Error Component Impact

Table 3.4-10 summarizes the Earth location error resulting from the 3 sigma pitch, roll, and yaw NPOESS platform attitude/pointing error components. Once again, the at-launch design and the post-calibration case are presented. The first 3 rows show the 3 sigma platform roll error and the corresponding Earth location error. The middle 3 rows show pitch related errors, the last 3 rows show yaw related errors.

Table 3.4-8: VIIRS Instrument Pointing Knowledge 3 sigma Error Estimates

Instrument Pointing Knowledge Error Source	Roll Error Estimate	Pitch Error Estimate	Yaw Error Estimate
DYNAMIC TERMS			
Telescope Thermal Effects	10.0 arcsecs	10.0 arcsecs	10.0 arcsecs
Telescope Bearing Runout	0.0	9.8	0.0
Telescope Control System Error	5.0	5.0	0.0
S/C-Induced Telescope Jitter	5.0	5.0	5.0
HAM Bearing Runout	0.0	4.9	0.0
HAM Thermal Effects	2.5	1.25	5.0
HAM Control System Error	2.5	1.25	5.0
S/C-Induced HAM Jitter	2.5	1.25	5.0
Aft Optics to OBA Thermal Effects	2.5	2.5	10.0
S/C-Induced Aft Optics Jitter	1.25	1.25	5.0
Detector Field Angle Stability	1.25	1.25	0.0
OBA Structure Thermal Effects	20.0	20.0	20.0
S/C-Induced OBA Jitter	5.0	5.0	5.0
STATIC TERMS			
Telescope Rotation Axis Tilt Error	10.0 arcsecs	10.0 arcsecs	0.0 arcsecs
Telescope Rotation Axis Cone Error	10.0	10.0	10.0
Telescope 1-G Sag	20.0	20.0	20.0
Telescope Environmental Shift	50.0	50.0	50.0
HAM Wedge Angle Error	0.8	0.4	1.7
HAM Rotation Axis Alignment Error	5.0	2.5	10.0
HAM to OBA Alignment Error	5.0	2.5	10.0
HAM 1-G Sag	2.5	1.25	5.0
HAM Environmental Shift	10.0	5.0	20.0
Aft Optics to OBA Alignment Error	2.5	2.5	10.0
Aft Optics Environmental Shift	12.5	12.5	50.0
Detector Field Angles	3.75	3.75	0.0
Focal Plane Orientation	1.75	1.75	0.0
OBA Structure 1-G Sag	50.0	50.0	50.0
OBA Environmental Shift	120.0	120.0	120.0
Total Dynamic (RSS)	24.6 arcsecs	26.6 arcsecs	27.4 arcsecs
Total Static (RSS)	142.6 arcsecs	142.2 arcsecs	152.1 arcsecs
3 sigma Total Combined Allocation	144.7 arcsecs	144.7 arcsecs	154.5 arcsecs

Table 3.4-9: Geolocation Impact of 3 sigma Spacecraft Position Errors

	At-Launch	Post-Calibration
X-Axis Platform Position Error	75.0 m	75.0 m
Corresponding Along-Track Earth Location Error (scan=0)	66.4 m	66.4 m
Corresponding Along-Track Earth Location Error (scan=55.8)	64.5 m	64.5 m
Y-Axis Platform Position Error	75.0 m	75.0 m
Corresponding Cross-Track Earth Location Error (scan=0)	66.4 m	66.4 m
Corresponding Cross-Track Earth Location Error (scan=55.8)	66.4 m	66.4 m
Z-Axis Platform Position Error	75.0 m	75.0 m
Corresponding Cross-Track Earth Location Error (scan=0)	0.0 m	0.0 m
Corresponding Cross-Track Earth Location Error (scan=55.8)	177.9 m	177.9 m

Table 3.4-10: Geolocation Impact of 3 NPOESS Platform Attitude Knowledge Error Components

Platform Attitude	At-Launch	Post-Calibration
Roll Pointing Error	56.7 arcsecs	36.8 arcsecs
Corresponding Cross-Track Earth Location Error (scan=0)	228.2 m	148.1 m
Corresponding Cross-Track Earth Location Error (scan=55.8)	1417.4 m	919.7 m
Pitch Pointing Error	67.7 arcsecs	36.8 arcsecs
Corresponding Along-Track Earth Location Error (scan=0)	272.4 m	148.1 m
Corresponding Along-Track Earth Location Error (scan=55.8)	330.6 m	179.7 m
Yaw Pointing Error	61.6 arcsecs	36.8 arcsecs
Corresponding Along-Track Earth Location Error (scan=0)	0.0 m	0.0 m
Corresponding Along-Track Earth Location Error (scan=55.8)	446.3 m	266.5 m

3.4.4.3. Instrument Pointing Error Component Impact

Table 3.4-11 summarizes the Earth location error due to the 3 sigma pitch, roll, and yaw VIIRS Instrument pointing error components.

Table 3.4-11: Geolocation Impact of 3 sigma VIIRS Instrument Pointing Knowledge Error Components

Instrument Pointing	At-Launch	Post-Calibration
Roll Pointing Error	144.7 arcsecs	27.6 arcsecs
Corresponding Cross-Track Earth Location Error (scan=0)	582.3 m	111.2 m

Instrument Pointing	At-Launch	Post-Calibration
Corresponding Cross-Track Earth Location Error (scan=55)	3616.1 m	690.4 m
Pitch Pointing Error	144.7 arcsecs	29.6 arcsecs
Corresponding Along-Track Earth Location Error (scan=0)	582.1 m	119.0 m
Corresponding Along-Track Earth Location Error (scan=55)	706.5 m	144.4 m
Yaw Pointing Error	154.5 arcsecs	31.9 arcsecs
Corresponding Along-Track Earth Location Error (scan=0)	0.0 m	0.0 m
Corresponding Along-Track Earth Location Error (scan=55)	1118.9 m	230.6 m

3.4.4.4. Combined Cross-Track and Along-Track Geolocation Error due to Position, Attitude, and Pointing Errors

Combined Earth location error in the along-track and cross-track directions are calculated by evaluating the square root of the sum of the squares (RSS) of the components.

Cross-track Earth location errors are contributed by errors in:

- Y-Axis Spacecraft position
- Z-Axis Spacecraft position
- Platform roll
- Instrument roll

Along-track Earth location errors are contributed by errors in:

- X-Axis Spacecraft position
- Platform pitch
- Instrument pitch
- Platform yaw
- Instrument yaw

Table 3.4-12 summarizes the cross-track and along-track Earth location error for the two cases presented earlier. In addition, Earth location error based on fraction of a moderate resolution band pixel and an imagery band pixel is shown.

Table 3.4-12: Total Combined 3-sigma RSS Geolocation Error in Cross-Track and

Along-Track Directions

	Total RSS Cross-Track Earth Location Error (3 sigma) (Y-Axis Spacecraft Position) (Z-Axis Spacecraft Position) (Platform Roll) (Instrument Roll)		Total RSS Along-Track Earth Location Error (3 sigma) (X-Axis Spacecraft Position) (Platform Pitch) (Instrument Pitch) (Platform Yaw) (Instrument Yaw)	
	scan = 0	**scan = 55.8**	**scan = 0**	**Scan = 55.8**
At-Launch	628.9 meters 0.800 pixels Moderate resolution Bands 1.600 pixels Imagery Bands	3888.6 meters 2.430 pixels Moderate resolution Bands 4.861 pixels Imagery Bands	646.1 meters 0.871 pixels Moderate resolution Bands 1.742 pixels Imagery Bands	1436.6 meters 0.898 pixels Moderate resolution Bands 1.796 pixels Imagery Bands
Post-Calibration	196.7 meters 0.250 pixels Moderate resolution Bands 0.501 pixels Imagery Bands	1165.6 meters 0.728 pixels Moderate resolution Bands 1.457 pixels Imagery Bands	201.2 meters 0.271 pixels Moderate resolution Bands 0.542 pixels Imagery Bands	426.1 meters 0.266 pixels Moderate resolution Bands 0.533 pixels Imagery Bands

The cross-track and along-track combined Earth location error can also be presented graphically. Figure 3.4-6 depicts the combined 3 sigma Earth location error resulting from platform/instrument position, attitude, and pointing errors based on the at-launch design. The centered origin of the plot represents perfect Earth location. Dashed grid lines are overlaid at 200-meter intervals. The innermost ring represents the 3 sigma Earth location error of pixels viewed at a scan angle of 0 degrees. Successive rings depict 3 sigma geolocation errors for pixels observed from increasing scan angle.

Figure 3.4-7 shows the combined 3 sigma Earth location error resulting from platform/ instrument position, attitude, and pointing errors based on the post-calibration case.

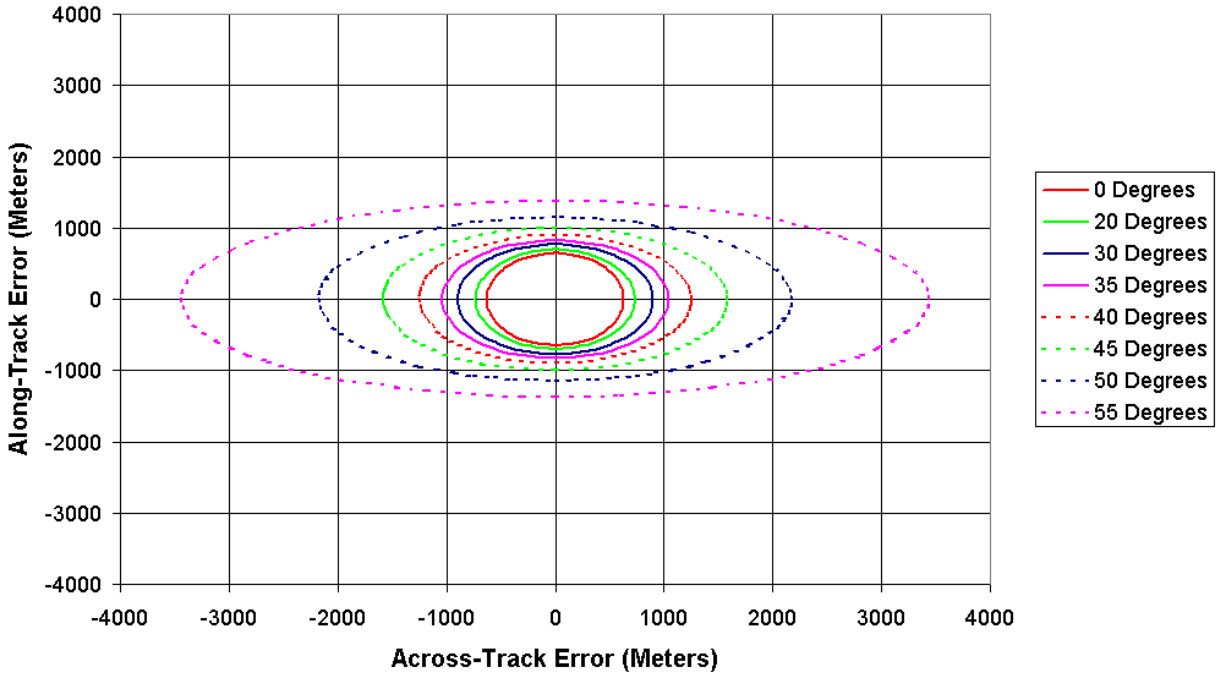

Figure 3-30: Three-Sigma Earth Location Error (in meters) resulting from the at-launch design for Scan Angles of 0, 20, 30, 35, 40, 45, 50, and 55 degrees

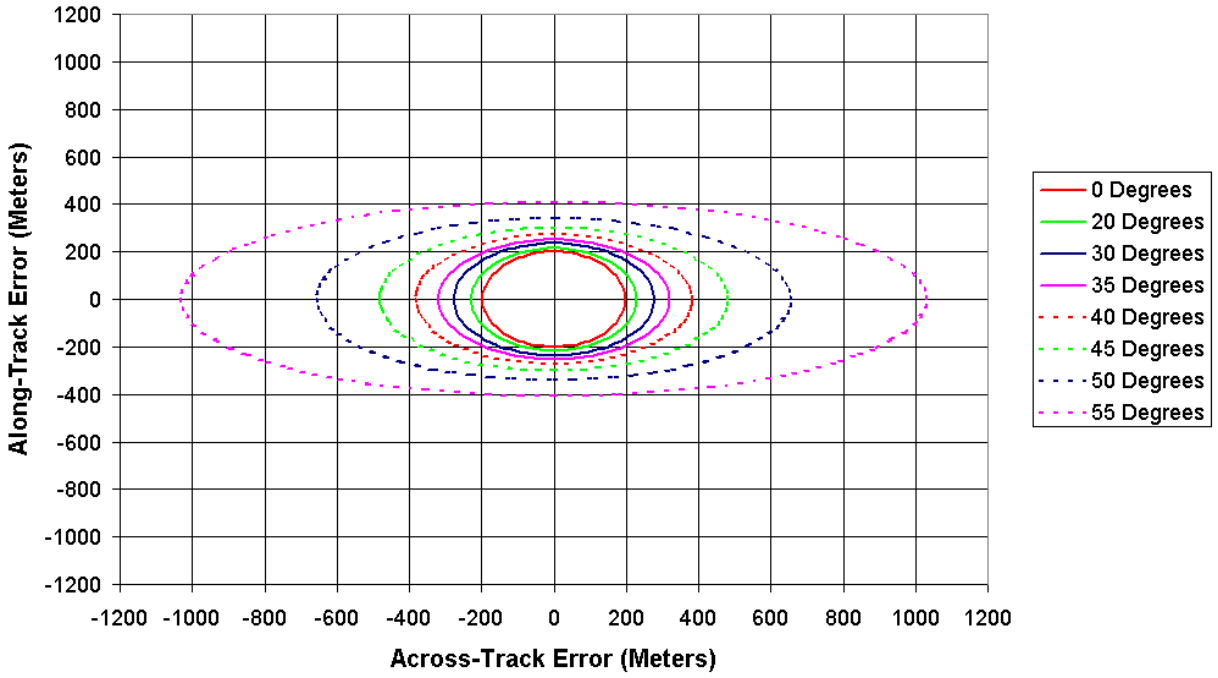

Figure 3-31: Three-Sigma Earth Location Error (in meters) resulting from the post-calibration estimates for Scan Angles of 0, 20, 30, 35, 40, 45, 50, and 55 degrees

3.4.5. Geolocation Equations and Methods

The equations used to calculate pixel geolocation error resulting from errors in platform position in space, platform/instrument pointing, Earth terrain height, (also equations to calculate pixel distortion), were taken from the “MODIS Earth-Location Algorithm Theoretical Basis Document” (Nishihama *et al*., 1997). A complete presentation of the underlying equations, with accompanying figures, is presented in that document and will not be repeated here.

3.4.6. Ground Processing

The VIIRS ground processing system is being designed to incorporate the capability to estimate and correct some of the residual errors described in this report. This includes building additional features into the operational VIIRS product generation software and developing additional tools for off-line geometric data analysis. This analysis will contribute to the refinement of the VIIRS geometric models over time.

3.4.6.1. Earth Location Processing Approach

The VIIRS processing software is being designed with the minimization of Earth location error as a primary goal. Errors that are known or measured (e.g., telescope angles, band and detector offsets) will be corrected, or correction data will be appended, during geolocation processing. The geolocation algorithm will use the best available estimates of the platform and instrument geometric parameters (e.g., platform/instrument alignment) stored in a calibration parameter file as ancillary data. These parameters will be refined over time using measurements of the residual error present in previously processed data products.

Errors that are static or slowly varying and can be adequately modeled will be estimated by comparing VIIRS data products with ground control to measure the residual geometric distortion. The measured distortion from a series of products will be used to detect systematic trends and to estimate improved values for the platform and instrument geometric parameters. A library of GCPs will be created and maintained to provide the necessary geometric reference. The control point images will be compared with the VIIRS imagery bands from selected data products, using automated image correlation techniques to measure the residual (presumable sub-pixel) geometric distortion. Trend analysis and parameter estimation activities will be carried out off-line using the distortion measurements from multiple data products.

The geometric distortion measurements will be collected routinely and analyzed to estimate the residual static biases in the pre-flight platform and instrument geometric parameters and to monitor the stability of these static error estimates. Improved values of the bias estimates will periodically be generated for use in subsequent processing and reprocessing. Selected data products will be extracted from the archive for more rigorous interactive evaluation. This will include manually verifying the residual error measurements at the control points to validate the automated correlation process and comparing products from the same orbital path to verify image-to-image registration.

The off-line geometric analysis and parameter estimation effort will grow more ambitious

with time as more data becomes available. A long data record will make it possible to compare the control point data with VIIRS image data from repeated and different orbital passes under varying conditions to detect constant offsets and slowly varying trends. Slowly varying dynamic errors that are repeatable and can be effectively modeled will be incorporated into the VIIRS geometric models over time.

3.4.6.2. Geometric Error Characteristics

The primary sources of VIIRS geometric error are described in the preceding sections and fall into four main categories: ephemeris errors, attitude errors, instrument/platform alignment errors, and instrument internal geometry errors. Errors from each of these sources have been characterized as static or dynamic. Static errors can, in principle, be estimated and corrected but the ability to model, estimate, and compensate for dynamic errors is limited by the time constant of the error dynamics. Low frequency dynamic errors (e.g., those varying over an orbit) can be detected and estimated with a reasonable number of GCPs while high frequency errors (e.g., those varying within a scan) cannot. This makes an understanding of the nature of the anticipated errors central to the development of geometric correction models and places a limit on what can be achieved by ground processing.

Ephemeris errors are dynamic but can be successfully modeled as constant biases to the six-element "spacecraft state vector" over periods of several minutes. Although these errors could be estimated using GCP observations, it would require a dense global network of ground control to perform routine ephemeris error correction. The same comments apply to the dynamic component of the attitude error though these attitude errors typically vary more rapidly than ephemeris errors, requiring even more frequent ground control observations. A significant component of the anticipated attitude error has been characterized as static. The problem of estimating the static attitude biases is complicated by their high correlation with the residual biases in the instrument-to-platform alignment.

The instrument pointing errors are likewise divided between static and dynamic errors with the largest single term being the instrument-to-platform alignment knowledge. The instrument-to-platform alignment error should be primarily a static bias, possibly with some slowly varying, repeatable thermal effects included. The geometric relationship between the instrument and the platform will initially be assumed to be static, but the VIIRS processing software will be designed to accommodate a time varying transformation to allow for future model refinement. Telescope rotation variations, though dynamic, are measured in the VIIRS instrument and will be corrected in geolocation processing. Other internal instrument geometric errors are difficult to measure. Most internal alignment errors are highly correlated with the external instrument-to-platform alignment.

3.4.6.3. Limitations of Ground Processing

As mentioned above, the ability to model and correct residual geometric errors through ground processing is limited by the time scale and repeatability of the dynamic error components and the observability (parameter correlation) of both the static and dynamic

errors. This is made even more challenging by the demanding VIIRS operational environment, in which continuously acquired data must be processed in near real-time with no operator intervention.

The ability to accurately measure sufficient GCPs in a fully automated system is limited by cloud cover, the availability and quality of world-wide ground control, and the performance of automatic correlation methods over varying viewing geometry and scene conditions. Attempting to estimate and apply corrections specific to a particular data set runs the risk of introducing product consistency problems due to differences in cloud cover and the resulting control point correlation performance. These concerns have led to the current approach in which control point data from multiple products will be analyzed with human intervention to monitor and refine the knowledge of the static and slowly varying error components for use in subsequent processing.

The achievable geometric product accuracy is also limited by the quality of the ancillary data sources, specifically the digital elevation model used to correct for terrain effects, and by the characteristics of the VIIRS instrument itself. The accuracy with which GCPs can be measured in the VIIRS data is limited by the resolution of the VIIRS pixels. Experience with Landsat and SPOT data has shown that operational automated image matching techniques reliably measure image displacement to an accuracy of 1/3 to 1/2 of a pixel. Using the 742 meter moderate resolution bands will provide a control point measurement accuracy of from 250 to 375 meters. Achieving bias estimation accuracy better than this will require the use of many control point observations. The ability to transfer the Earth location knowledge gained through the use of the imagery bands to the moderate resolution bands is further limited by the band-to-band registration knowledge.

3.4.7. Terrain Height Error Impact

The National Imagery and Mapping Agency (NIMA) Digital Terrain Elevation-1 (DTED-1), a digital terrain data base distributed by the United States Geological Survey (USGS) for the United States and by the Department of Defense (DoD) for selected parts of the world, has a specified vertical accuracy of 30 meters (linear error encompassing 90% of the data points). The portion of DTED controlled by DoD has large areal gaps over South America, Africa, Australia, Antarctica, and remote parts of Asia; in addition, it has not yet been approved for general release. Over the next several years data from the Shuttle Radar Topography Mission (SRTM) will become available for most of the world's land area between 60 degrees north latitude and 56 degrees south latitude at a spatial resolution (~100 meters) and accuracy (~30 meters) comparable to or better than the DTED-1. Regions outside the SRTM latitude range are covered by the global GTOPO-30 elevation database constructed for the EOS project. This data set provides elevations approximately every 1000 meters (30 arc-seconds) and was compiled from a variety of sources including DTED and Digital Chart of the World (DCW). A conservative estimate of the accuracy of the GTOPO-30 data is 160 meters (90% linear error) based on the DCW accuracy measured during the construction of GTOPO-30 by comparing DCW to DTED.

Figure 3.4-8 shows the Earth location errors resulting from a 30 meter and a 160 meter terrain height error. A 30 meter inaccuracy is representative of the SRTM data while the

160 meter inaccuracy is representative of the DCW-derived GTOPO-30 data available at high latitudes. The resulting Earth location error is primarily in the cross-track direction and is a function of scan angle. There is no impact on geolocation at nadir. The geolocation error reaches a one-to-one correspondence (a 1 meter terrain height error leads to a 1 meter geolocation error) at a scan angle of approximately 40 degrees. Since geolocation error is linear with terrain height error, one can easily estimate Earth location error resulting from any terrain height error from this plot.

Terrain height induced error is unlike the other errors described in this document with regard to collocation of two pixels observed at different times. For any given location it is not random from one observation to the next. There is good and bad news resulting from this. The good news is, if two observations of the same point are made during different times but when the pixel is directly under the spacecraft, there will be no terrain height induced error in location or coregistration. If the two observations are made from different orbits with very similar ground tracks, for instance both ground tracks pass about 800 km to the right of the point under consideration, there may be a large location error but it will be nearly the same for both observations. Thus there will only be a small coregistration error. The bad news is, if one orbit ground track is to the left of the ground point and the other is to the right, the geolocation error will be the same in magnitude but in opposite directions. This means that the terrain height induced coregistration error will be the sum of the magnitudes of the two geolocation errors. Thus if precise coregistration is important for a particular investigation, it becomes important to give special consideration to the viewing geometry of the various observations.

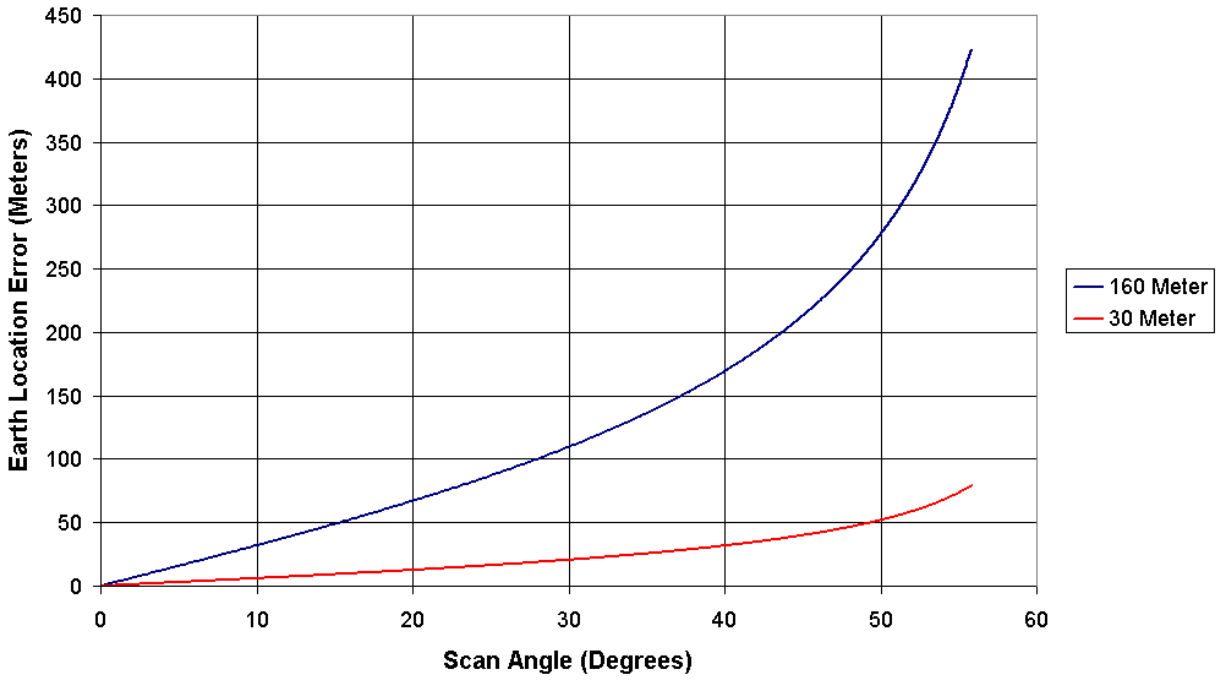

Figure 3-32: Earth Location Error (in meters) resulting from various Terrain Height

Errors as a Function of Scan Angle

3.4.8. Summary

There are five issues which are of concern with regard to accurate geolocation and/or coregistration of VIIRS data: Platform position knowledge, Platform attitude knowledge, Instrument pointing knowledge, detector to detector registration, and terrain height error. Three of these, the location and attitude of the Platform and the pointing of the Instrument are comparable to or better than that for previous instrument data sets such as MODIS. Their impact is such that VIIRS pixel data could be correctly Earth located within 0.7 (moderate resolution band) pixels (3 sigma). Earth location accuracy could be improved to within 0.3 pixels if ground processing is able to remove the expected biases. Thus these errors are of the same scale as those due to band-to-band registration accuracy error (0.2 pixels) and inadequate terrain height information at high latitudes (0.1 pixels).

3.4.9. Error Analysis Algorithms

The 0.371 km resolution VIIRS imagery bands will be used in conjunction with sets of GCPs to validate the accuracy of the VIIRS Earth location data. GCPs will be used to estimate residual errors in the spacecraft ephemeris and attitude. Small geolocation errors are mainly caused by errors in these parameters. Other parameter errors are difficult to analyze. However, through long-term trend analysis, we are hoping to expand error analysis to the focal plane, telescope geometry, and half-angle mirror assembly geometry. The land ground control matching algorithm is first explained and then the trend and bias analysis.

3.4.9.1. Land Control Point Matching and Correlation Algorithm

The Control Point Matching software will use the control points to automatically collect the raw verification data (in the form of GCP residual errors). These data will then be analyzed off-line. The control point processing methods to be employed for VIIRS are the same as those developed for the MODIS sensor. These techniques are described in detail in the “MODIS Earth-Location Algorithm Theoretical Basis Document” (Nishihama et al., 1997) and will only be summarized here.

3.4.9.1.1. General Background and Preprocessing

The higher resolution VIIRS imagery bands will be used in conjunction with preassembled sets of GCPs to validate the accuracy of the VIIRS Earth location data. The known position of the control point can be used to extract an image neighborhood from the new VIIRS data at the location predicted by the Earth location data. Nominal moderate resolution calibration parameters will be applied to the VIIRS neighborhood to remove moderate resolution artifacts (detector to detector striping). A simple cloud detection algorithm (e.g. thresholding) will also be used to identify areas that are not suitable for image correlation. This product validation will be scheduled after the moderate resolution correction and cloud detection algorithm have been performed so that the simple moderate resolution correction, snow, sea ice and cloud detection algorithm would be skipped. In either case, the control point image chip can then be correlated with the VIIRS neighborhood to measure the sub-pixel displacement between its predicted and observed locations. The control data image chips will be processed to simulate the effects of the

VIIRS viewing geometry including the elevation-related parallax and correlated with the real image data. This will include applying the VIIRS modulation transfer function (MTF) to the higher resolution control chips. The extracted VIIRS data will be shifted along the image lines and pixel counts over the control point chip. At each fraction of shift in the positive or negative direction, the MTF is applied over this higher resolution control point chip and matched with the VIIRS resolution. The measured image displacement shift or error angles, along with the extracted VIIRS neighborhoods, will then be passed along for off-line analysis.

3.4.9.1.2. Control Point Image Chips and Control Scenes

The MODIS control point library, derived from Landsat Thematic Mapper data, will be augmented as necessary by Landsat 7 Enhanced Thematic Mapper Plus (ETM+) data. The improved absolute geodetic accuracy of the ETM+ data combined with the availability of SRTM terrain data make it possible to construct high-quality control points over a larger portion of the globe. Each control point is selected to contain a primary identifiable feature that will provide a strong target for image correlation at the VIIRS imagery band scale.

The term feature is used here to mean a single, identifiable, geographical point on the earth's surface, specified by exactly one set of coordinates: latitude, longitude, and elevation. Ideally, the latitude, longitude, and elevation values point to a stable geographical feature that is detectable in VIIRS data. Each land control point chip will have exactly one key feature. Features that are close together may be used but they will be put into separate, possibly overlapping, control point chips.

3.4.9.1.3. Extraction of Control Scene for Each Control Point Chip

Based on VIIRS granule's geographical metadata, (i.e., on the latitude and longitude coordinates of the corner points of the VIIRS data granule) a list of control points that could be in that granule will be constructed. The following steps will be taken to build a VIIRS control scene for each control point.

Step 1. Find a scan that contains the predicted control point based on the geographic locations of the scan,
Step 2. Find a fractional pixel/line number from the geographic location of the control point using an inverse mapping algorithm and determine a nearest pixel (called feature pixel),
Step 3. Extract line segments from the current scan containing its neighborhood,
Step 4. Extract extra line segments from the above (and or below) the scan if the control point is too near the edge of the scan.

Figure 3.4-9 shows schematically a typical control scene created using three scans.

3.4.9.1.4. Simulated VIIRS Scenes with VIIRS Pixel Resolution

When a VIIRS detector in motion views TM pixels on the ground, the TM pixel radiances must be summed and put through the triangular weighting function, and pixel aggregation, to generate expected VIIRS pixels. All of the TM pixels within a 2-VIIRS-pixel wide rectangle are weighted and added together to get the VIIRS pixel value, as shown in

Figure 3.4-10, where geometry does not show possible terrain and scan angle effects.

In Figure 3.4-10, TM pixel locations 1 and 2 are contributing to VIIRS pixel I and II, while No 3 and 4 are contributing to VIIRS pixel II and III. The triangular weighting function and the two-pixel wide set of TM pixels used to generate an expected VIIRS pixel in bold outline.

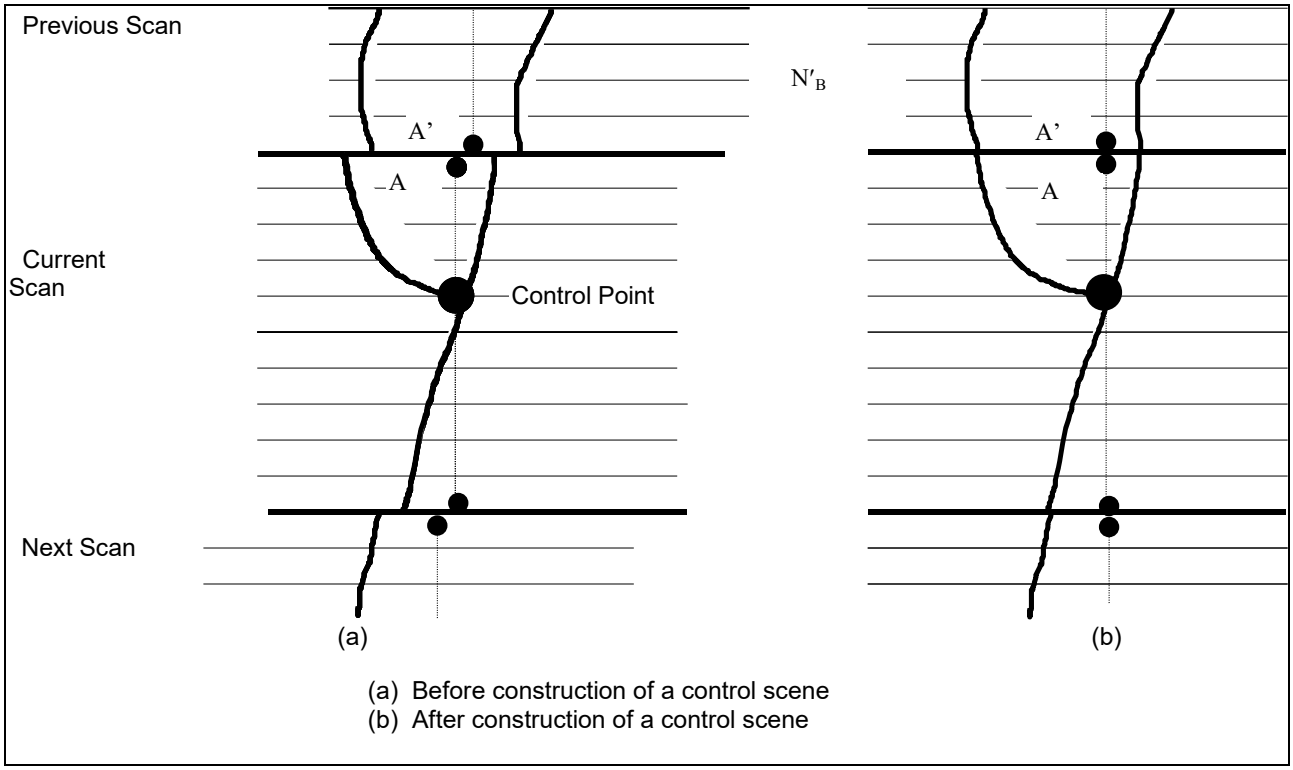

Figure 3-33: Connecting Parts of 3 Scans

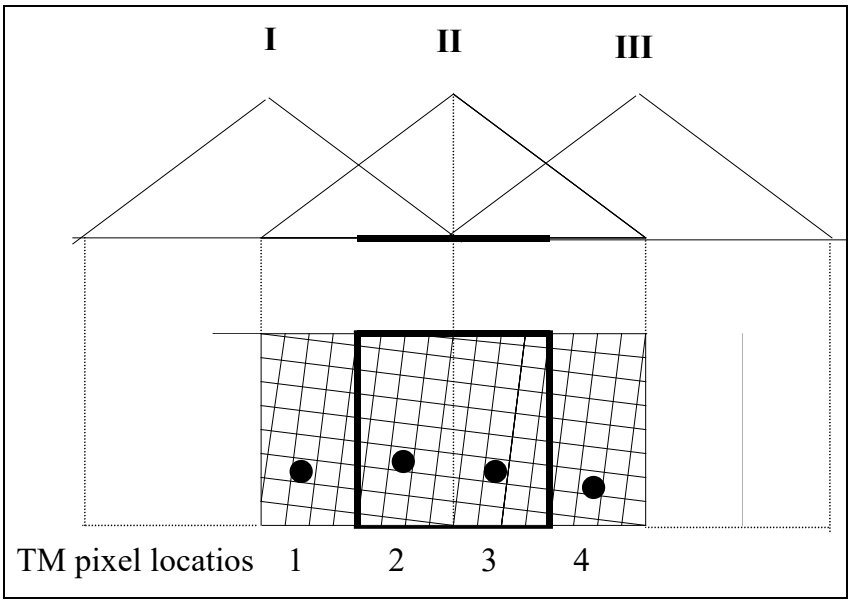

Figure 3-34: Triangular Weighting Function

To prepare for the correlation of TM and VIIRS chips, multiple simulated VIIRS scenes are generated at different sub-pixel offsets. Finding the simulated VIIRS scene which best matches the actual VIIRS data identifies the best-fit sub-pixel offset for that control point.

3.4.9.1.5. Correlation of Simulated VIIRS Scenes and Actual VIIRS Control Scene

The cross correlations between simulated and actual VIIRS scenes will be performed using the normalized cross correlation function. (See ECS Project, 1995 at page 683, Equation 20.4-1.)

In a shift pattern of ten steps of 1/10th of a pixel each, there are 11 x 11 = 121 cross correlations to be performed. After all of the expected VIIRS pixel arrays are constructed and all the cross correlations are computed, the offsets that produce the maximum cross correlation are determined. The actual location of the best sub-pixel match point can be used to generate:

(1) Actual location of the control point in the VIIRS scene in terms of fractional line/pixel numbers.

(2) Sensor view vector.

(3) Systematically computed geodetic coordinates of the control point.

(4) Residuals error for residual data base, along with the VIIRS control scene.

3.4.9.1.6. Error Conditions

The following conditions are regarded as errors:

- If the maximum cross correlation occurs at the edge of the shift region, then that set of geolocation residual error values should be flagged as suspect and as out of range.

- It is likely that either the cross correlations failed to detect the correct location of the feature in the image, or that the image correction needed is larger than what the algorithm is capable of measuring (e.g., larger than one VIIRS pixel).
- If a maximum cross correlation value occurs in two adjacent elements of the cross-correlation matrix, then the residuals could be recorded as the average of the two corresponding values.
- If the maximum cross correlation value occurs in more than two (or more than one) element of the cross-correlation matrix, then no residuals will be recorded for that control scene.

3.4.9.2. Error Analysis and Parameter Estimation Algorithm

The geolocation error comes from various sources including errors in satellite position, velocity, attitude, sensor misalignments, and telescope related errors. It may also be possible to have clock drift in the sensor data stream differing from the spacecraft's. Many of the sensor and telescope characteristics and internal temperature will be continuously collected and included in the telemetry. Some changes may appear in the form of such as attitude parameters and could be observed through the evaluation of control point residuals.

In this section, we describe the algorithm to estimate satellite position/velocity and attitude parameters through use of GCPs. It is assumed that some of the sensor misalignments and telescope error will be absorbed in the attitude parameter error.

From the control point matching algorithms, the following values are expected for each control point:

1. Time of control point observation,
2. Satellite position and velocity,
3. Attitude parameters $\xi_r^0, \xi_p^0, \xi_y^0$ for roll, pitch, and yaw
4. Fractional scan line and pixel counts and a view vector in the spacecraft coordinate
   system pointing to the control point,
5. Systematic control point coordinates in the ECEF coordinate system,
6. Observed control point coordinates in the ECEF coordinate system,
7. Half-angle mirror side information (used in the trend analysis).

It is important to know that the error analysis depends on the accuracy of the control point matching results.

To express a GCP and view vector, the following notations are used:

p - True location of satellite (to be estimated),
$\mathbf{p}_0$ - Satellite location from the systematic data,

$\mathbf{x}_0$ - GCP location through the systematic data,
$\mathbf{x}_{cp}$ - True GCP location.

For their relationship, see Figure 3.4-11.

Errors detected and calculated by the GCP matching algorithm as described above will be used in the error analysis algorithm. Assuming errors are small, we will follow a methodology used by Landsat 7 (see USGS, 1997) and MODIS (Nishihama *et al*., 1997) and refine our error estimate for correcting the parameters. In this approach, satellite position/velocity and attitude parameter residuals are estimated through use of the Earth and satellite geometry. The differences in the control point location and systematic point locations are used to construct a normal equation. By solving the normal equation, the error is estimated and the original parameter set is updated to create a new set of parameters. This process continues until it reaches a certain threshold.

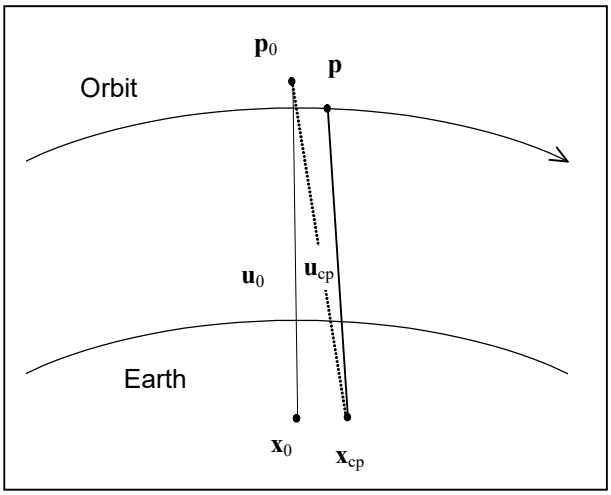

Figure 3-35: Satellite Position and Ground Control Point

The process is described in detail in the “MODIS Earth-Location Algorithm Theoretical Basis Document” (Nishihama *et al*., 1997) and in the “Landsat 7 Image Assessment System Geometric Algorithm Theoretical Basis Document” (USGS, 1997) and will not be repeated here. The algorithm solves a set of observation equations using standard minimum-variance estimation techniques. Since the observation equations are non-linear and are linearized by computing partial derivatives, the entire process must be iterated until the correction parameters converge.

Sensor misalignments and telescope errors will be studied by examining the trends in long term results. More complex (e.g., time or temperature dependent) models for these parameters will be developed based on actual experience with VIIRS data and will be verified against a long-term data record prior to implementation in the production stream.

3.5. PRACTICAL CONSIDERATIONS

The following sections discuss practical implementation and operational considerations

including numerical stability, computational efficiency, algorithm verification, product validation, automated quality control and metadata generation, and possible processing exception conditions.

3.5.1. Numerical Computation Considerations

The VIIRS geolocation algorithm incorporates two iterative procedures that must be implemented carefully to ensure convergence. The first of these is the general iterative conversion from ECEF to geodetic coordinates. The SDPTK function that is utilized in the VIIRS geolocation algorithm has demonstrated robust performance in the operational processing of EOS sensors including MODIS.

The second iterative procedure is the detection of the VIIRS LOS intersection with the terrain. Simple approaches to implementing this algorithm break down at high off-nadir angles due to the possibility of multiple intersections of the LOS with the terrain surface. Under these conditions, care must be taken to ensure that the algorithm converges to the correct terrain intersection point (i.e. the intersection closest to the satellite). This is achieved here by searching from above to find the first (highest) terrain intersection. The iteration proceeds down monotonically until the viewing vector is below the terrain surface so that convergence is not a problem. The precision of the final terrain intersection determination is a function of the local relief. The degree to which this approximation breaks down is a function of the height range searched and the satellite look angle.

3.5.2. Programming/Procedural Considerations

The computational burden imposed by the VIIRS Earth location algorithm arises primarily from the terrain intersection computation. Current estimates indicate that approximately 80% of the Earth location processing load is used by the terrain correction step. Within this procedure the conversion from ECEF to geodetic coordinates consumes the bulk of the processing.

In the ECEF to geodetic conversion the main computational driver is the number of trigonometric functions that must be performed. One way to achieve efficiency in these computations is to carefully apply small angle approximations and Taylor series expansions when the angles involved change very little between invocations. Another approach is to implement the standard sine and cosine functions as look-up tables that have been pre-computed based on the required precision of the calling routine. The tradeoff of computational precision for computational performance would have to be carefully weighed before implementing any of these approximations.

3.5.3. Configuration of Retrievals

The Earth location data fields will be generated using a fully automated process during routine operations with human intervention required only if there is a need to update the input geolocation parameters based on offline validation and analysis results. In order to achieve the required Earth location accuracy, however, it will be necessary to perform an initial on-orbit geometric calibration to estimate the static pointing errors that will be present when using only prelaunch characterization data. These instrument characterization and calibration activities will require a skilled analyst with considerable

knowledge of the VIIRS instrument. It will also require the development of the necessary analysis software tools and the assembly of the required supporting ground control data and reference imagery before launch.

3.5.4. Quality Assessment and Diagnostics

At the time of this writing various studies are ongoing to consider the level of diagnostic checks and quality flags that should be included in the operational code implementation of the VIIRS geolocation algorithm. It can be anticipated that some sort of sanity check should be employed to ensure that reasonable S/C ephemeris and attitude data and VIIRS scan time and encoder data inputs are available. Minimally error diagnostics should be available and pixels that cannot be geolocated either due to problems with input data, orientation of the spacecraft, or limitations of the algorithm should be flagged in the geolocation output.

A minimal set of metadata should accompany the geolocation output. The metadata should identify the applicability of the data, the temporal and spatial coverage, and the algorithm version and run-time options that were used to produce the data.

3.5.5. Exception Handling

The Earth location algorithm will provide mechanisms for gracefully handling the following three known exception conditions:

1. There are missing ephemeris or attitude data,
2. There are missing DEM data, and
3. The instrument LOS does not intersect the Earth.

The input ephemeris and attitude data will be checked for consistency and completeness by the geolocation processing software. These checks will be first order only and will primarily remove blunders. For example, the magnitude of the position and velocity must be close to the nominal values and the instrument must be pointing downward, etc. If these ancillary data are completely missing or unusable, an error message will be generated and Earth location data will be filled by interpolation with appropriate quality control information entered into the product metadata. In the case of missing input DEM data, the Earth location will proceed using the Earth ellipsoid as the reference terrain surface. A warning message will be generated and an appropriate notation added to the product metadata. If the LOS intersection algorithm detects a viewing vector that does not intersect the Earth ellipsoid, the geodetic position fields will be populated with fill values, a warning message will be generated, and a notation will be added to the product metadata.

3.6. ALGORITHM VALIDATION AND DISCUSSION

3.6.1. Algorithm Verification

The purpose of the algorithm verification process is to verify that the algorithm will accurately calculate the location of VIIRS samples. This verification process will verify the

accuracy of the algorithms presented here in this document as well as the algorithm's implementation in software. Initially at launch there will be systematic biases in the model that will be removed by the geometric parameter estimation process. It is expected that over time the algorithm will converge to an accurate solution which will be stable and repeatable in both scene to scene and scene to ground measurements.
There are three steps in the verification process. First, the software implementation of the Earth location model must match the algorithm. Second, the algorithm implementation must correctly represent the instrument. Third, the software implementation should match the end-to-end system, which verifies both the instrument model and the satellite and Earth models. The tools for measuring the accuracy will be tested as part of the verification process.

Once the algorithm has been verified, care must be taken that, as the algorithm evolves, the chain of verification is not broken. This process will involve careful feedback of model changes, both to the algorithm and constants. This will be done by verifying that the new model increases the accuracy from the previous baseline for multiple products.

3.6.1.1. Verification Standard

The VIIRS accuracy testing involves two types of related measurements, absolute and relative. The former measures how well the VIIRS instrument matches a location on the Earth. The latter measures how well multiple images from the same area on the ground match one another. If two images have an absolute accuracy of 100 m, then the relative accuracy of the images is better than 200 m and would be around 141 m if the errors are uncorrelated and normally distributed. A measurement of relative accuracy does not necessarily give any information about the absolute accuracy; two scenes that are well registered to one another could be off by a large amount in an absolute sense.

The absolute error is very important in using VIIRS data with other data sets, such as maps and other satellite data. The standard by which the absolute accuracy is based is the World Geodetic System of 1984 (WGS84), an international standard model of the Earth. This standard is based on a number of physical constants, including the origin and orientation of an Earth centered and fixed Cartesian coordinate system, a standard ellipsoid model of the Earth, and a definition of mean sea level. Many countries are now basing their new maps on this standard and there are standard transformations from most older maps to this standard.

The relative measurement is very important in determining what changes occur between images. Since the mission is to look at global change, measuring season-to-season and year-to-year variations are very important. There is no standard for the relative accuracy measurements. It is expected that by achieving the absolute accuracy goal, the relative accuracy requirements will be met.

3.6.1.2. Preflight Verification

The VIIRS algorithms will be verified preflight by prototyping key Earth location subsystems to develop and refine geometric models, and data processing and analysis techniques using both preflight data and VIIRS simulated data from other instruments such as MODIS.

The verification that the software matches the theoretical algorithm will be performed by software walk through and unit testing of individual parts of the algorithm. Separate hand calculations will be performed to verify that the unit testing is correct. The second step is to verify the instrument part of the model. This will be done by verifying that the results from the instrument model match those from live data from the engineering model. The third step will be done both preflight and in-flight. The preflight part will be done using satellite data from other instruments such as MODIS. Parts of the software model, which are common to both VIIRS and MODIS, will be tested by verifying the Earth location of the MODIS data. In addition, simulated VIIRS data will be available to test the algorithm preflight.

3.6.1.3. In-flight Verification

The in-flight accuracy of the VIIRS Earth location data will be verified using automated control point correlation methods coupled with off-line analysis. Control point measurement will be built into the VIIRS geolocation production system but, operationally, will only be applied to a subset of the data products based on control availability and cloud cover. This product verification activity is described in more detail below.

The schedule for in-flight Earth location/geometric verification activities is less well defined than the preflight phase. The planned activities are divided into Short-Term (conducted in the first three months after activation), Medium-Term (conducted in the first year of operation), and Long-Term (ongoing sustaining activities) in Table 3.6-1.

The performance of the automatic correlation procedure will be verified through interactive control point mensuration. The performance of interactive control point mensuration method is expected to be less accurate than the automatic procedure but will be used to provide a double check of the algorithm. The image internal geometric accuracy will be verified by correlating multiple VIIRS products from the same orbital path. This will include looking for even/odd scan artifacts due to differences in the two half-angle mirror sides. The control chips and neighborhoods will be used to verify the performance of the control point mensuration procedure itself, while the measured distortions will be used in anomaly detection, trend analysis, and to build up a statistical record of Earth location performance.

3.6.1.4. Verification of Inputs

The verification of the inputs to the VIIRS Earth location process must be performed to enable the overall process to be verified. It is expected that the inputs to the VIIRS Earth location algorithms will have systematic biases in them. As part of the verification process, these inputs will be verified and biases removed. These inputs include information about the geometric characterization and calibration of the instrument and spacecraft, information about the spacecraft position, velocity, attitude, RTA encoder data, GCPs, and the DEM. For the computational saving, the geolocation calculation is performed only for the ideal band. All real bands' locations on the ground are derived from the ideal band location as described in Section 3.3.2. Because of this, the control point residual calculation relies on the approximated values. The approach will create some systematic or random error for the GCP residual error calculation.

Table 3.6-1: In-Flight Algorithm Verification Activities

Time Frame	Activity
Short-Term (first three months)	Verify Earth location algorithm performance as soon as operational data becomes available.
	Look for constant bias terms in control point QA results to assess accuracy of instrument alignment knowledge.
Medium-Term (first year)	Estimate refinements to instrument alignment knowledge using control point QA data.
	Analyze ancillary digital terrain data accuracy using orbit-to-orbit tie points.
	Analyze control point QA results to characterize repeatable errors correlated with scan angle and/or mirror side.
	Use control point QA results to detect repeatable within-orbit trends such as thermal effects.
	Use data from multiple instruments to estimate spacecraft position and attitude accuracy performance.
Long-Term (sustaining activities)	Analyze control point QA data for trends to monitor stability of instrument geometric parameters.
	Refine geometric models for mirror and thermal effects as appropriate based on longer data record.

3.6.1.4.1. Instrument and Spacecraft Data Verification

The geometric characterization and calibration of instrument, spacecraft, and ancillary data are integral to the verification process. Geometric calibration activities that are being performed by the instrument and spacecraft contractors will be carried out in accordance with their contract schedules. Specifically, the preflight VIIRS instrument geometric calibration will be performed by the Raytheon SBRS according to their calibration plan. Of particular interest to the Earth location model are the absolute orientation, RTA positioning, MTF, and band-to-band registration tests. Preflight measurements of the instrument-to-spacecraft alignment will presumably be carried out during the instrument/spacecraft integration phase per the NPOESS development schedule.

The verification of the spacecraft pointing knowledge and position information will be performed by the spacecraft builder and the IPO. The science and telemetry data from the instrument and the telemetry data from the spacecraft, up to the point where it is input into the Earth location model, must also be verified.

Refinements to the knowledge of the alignment between the various parts of the instrument, and the instrument to the spacecraft, will be done as part of the geometric parameter estimation process.

The input data stream to be used for geolocation of VIIRS products will be read from the engineering packets and validated, which includes the spacecraft orbit position and

velocity, attitude angles and rates, and the RTA encoder times. The scan start times and half-angle mirror side indicators, which are also required for geolocation, will be unpacked and converted by the unpacking software. It is assumed that any validation required for those data has been performed prior to geolocation. The validation tests to be performed fall into four basic categories: absolute limits, delta limits, consistency, and sanity.

1. The absolute limit test checks individual measurements against a specified range. For a value *V* and lower and upper limits *L* and *U*, the test requires that:

$$L \le V \le U \tag{3.6-1}$$

2. The delta limit test checks the differences between successive values of an individual measurement against a specified range. For a delta limit δ, the test requires that:

$$\left|V_{j+1} - V_j\right| \le \delta \text{ for j-}th \text{ and } j+1th \text{ sample of } V. \tag{3.6-2}$$

3. Consistency tests compare different measurements within a general category to verify consistency among the measurements.
4. Sanity tests involve computing additional quantities from the measurements, which can be checked against absolute limits such as magnitude of position and velocity vectors. These are performed to take advantage of our knowledge of the mission limits or the physical processes involved.

3.6.1.4.2. Ground Control Verification

There are two methods for verifying the accuracy of the GCP information. The first method is to internally verify the control using information from either VIIRS or other satellites. The second is to use some other type of verification such as an accurate map base or points from the Global Positioning System (GPS). In either case, there will be some prior knowledge of the accuracy of the control point information based on the source.

To use satellite data for validating the control points, it will be assumed that the error in the position of the satellite is random and that the pointing knowledge errors do not systematically vary over any single location. If both these assumptions were true, it would be easy to take the large number of measurements of the points and then improve the knowledge of the control points using this information. However, only the first is true. The pointing knowledge errors are expected to have some systematically varying component, which we plan to remove as part of the geometric parameter estimation. If only the NPOESS satellite or satellites with similar orbit characteristics are used, the same type of bias may occur in all of the measurements. This would prevent the separation of the ground control bias from the systematically varying component of the pointing knowledge. So, it is not possible to use only the satellite data to validate the GCPs.

One problem in verifying the absolute accuracy of the VIIRS instrument is with the original maps and other sources, which may to be used in collecting control point information. In some well mapped areas of the world such as the United States of America (USA), it is easy to acquire highly accurate maps. In the continental USA, Canada, Europe, and some other areas, typical maps have a low enough vertical and horizontal error to be used as sources for absolute control point location information. The rest of the world is not as well mapped. In some areas the only maps available are 1:250,000, or even 1:1,000,000 scale maps. The accuracy of these maps is typically from 125 to 450 m horizontally and 50 to 200 m vertically. In areas of the world where accurate maps are unavailable, Landsat 7 ETM+ and SRTM elevation data, accurate to approximately 50 meters horizontally and 30 meters vertically, can be used instead.

Using an accurate map base or GPS has some appeal but there are also problems with this approach. First, the availability of accurate maps throughout the world is limited and the collection of GPS verified control points is likely to be expensive. Even once the ground control has been identified there is still the problem of transferring this knowledge to the image. Typically, a control point can only be identified in an image to the nearest 1/2 pixel by an operator. This should not be much of a problem with VIIRS because the control points are being identified in higher resolution images.

The correlation process may introduce a systematic bias into the process since it relies on correlation of an area and not the location of a single point. One bias may be caused by a change in elevation over the correlation area; the second may be caused by temporal changes in the scene or in the viewing geometry of the scene. In the case of errors introduced by elevation, correlation techniques rely on locking up on unique strong features in the correlation area. In the case when there is only a single strong feature at the center of the correlation area, this is not a problem. Many times, however, there are a number of less strong features in the area, which, if they are at a different elevation than the main feature, may cause the correlation process to be biased. To minimize this type of effect, efforts will be made to pick control points in areas that are relatively flat, or to orthorectify the control points before use.

Temporal changes and changes in the viewing geometry may cause other biases. Both may cause the correlation to fail completely. If a correlation is successful, there is a possibility that a systematic bias may be introduced by changes in the scene. For instance, if the correlation is occurring on a large lake in which the shallow end is partially covered by ice in the winter, the correlation of this area would tend to be biased toward the deep end of the lake. A different viewing geometry may also cause a similar bias. Suppose the image is of a volcanic island and the original image of the GCP is taken when the shadows are to the left of the mountain. If, when the point is later imaged, the viewing conditions are such that the shadow has moved to the right side of the mountain, there is a good possibility the correlation will be biased.

One solution that has been used in the past to alleviate this problem with correlation has been to use a large number of control points. If many control points of different types are used then this error can be treated as a random error. In any case, statistics should be kept for each control point. Moreover, care should be taken to use the good control points

in the geometric parameter estimation, and to include the control point correlation statistics in the solution as well as any measured mean shift in the location.

3.6.1.4.3. Digital Elevation Model Verification

The terrain correction accuracy will be verified and areas of poor DEM data will be identified by measuring tie points between overlapping VIIRS products. The DEM will be verified in two ways. First, the provider of the DEM will perform quality checks to verify its accuracy. It is expected that the DEM provided will have, at worst, a 1 km resolution with 160 m uncertainty in vertical direction (e.g., GTOPO-30). Second, multiple elevation data sets (SRTM and GTOPO-30) will be compared to each other in regions of common coverage.

Once the images have been correctly navigated, the image data will be rectified and then areas from overlapping orbits will be correlated. The tie points would be generated automatically, possibly using an interest operator to generate "good" tie points. Once this is done a sufficient number of times, there may be certain areas of the world where there is a systematic bias between every image pair. It is expected that biases covering large areas may be found using this method but the vertical accuracy when correlating the imagery bands is expected to be, at best, 250 m (1 sigma). Particular care should be taken to do this type of correlation only after sufficient systematic biases have been removed from the pointing knowledge. Lack of sufficient high frequency information in the DEM will cause residual high frequency errors in the VIIRS Earth location knowledge. It will not be possible to remove these errors until a higher resolution DEM becomes available.

3.6.2. Product Validation

The validation process will examine the end result of the process (the Earth location product) and not the mechanism for producing the product. This process will be done independently of the verification process. A number of products will be selected and measurements will be performed independently of the production software. This process will not necessarily be a global process but sufficient number of measurements will be made so that there is a high level of confidence in product accuracy for the entire globe. This validation process will be done with some regularity, either biannually or annually, and after any significant modifications to the production software or constants occur. Both the absolute and relative accuracy of the products will be validated.

The validation measurement tools will be developed independently of the production tools. Ground control information will also be independently collected for measurements of absolute accuracy. Of course, the same source material, maps, etc., may be used for GCPs.

3.6.3. Risks and Risk Reduction Efforts

The most significant Earth location algorithm risk is that the Earth location data fields generated will not be sufficiently accurate due to inadequate knowledge of the VIIRS instrument’s operating characteristics. As the error analysis in Section 3.4 demonstrates, the anticipated prelaunch knowledge of the key geometric characteristics is such that the

initial on-orbit Earth location data is not expected to meet the accuracy requirements. The errors present in the at-launch geometric parameters can be categorized into four groups:

1. Static errors that are unknown but do not change after launch, such as an overall rotation of the sensor relative to the spacecraft
2. Quasi-static errors that do not change with time, but do vary with scan angle, such as telescope axis or half-angle mirror wedge and tilt angle errors
3. Low-frequency dynamic errors that change slowly with time in a more-or-less predictable way, such as orbital temperature-induced distortion
4. High-frequency dynamic errors that change too rapidly or randomly to predict or measure, such as bearing runout and servo errors.

As shown in Section 3.4, the initial on-orbit Earth location error model is dominated by static pointing errors. These errors can be effectively measured and modeled as sensor alignment offsets using the calibration techniques successfully demonstrated by Landsat 7 (USGS, 1997) and MODIS (Nishihama *et al*., 1997). Quasi-static errors are more challenging but can also be addressed using reference imagery to measure VIIRS offsets at all scan angles and by analyzing data from many VIIRS scans. A method for solving the similar problem of estimating the Landsat 7 Enhanced Thematic Mapper Plus scan mirror profile on orbit has also been demonstrated (USGS, 1997).

The fundamental approach to mitigating the risk of inadequate Earth location accuracy has two aspects. First, the Earth location algorithm and its software implementation are designed to explicitly model and allow for updates to the values of the key geometric characteristics of the VIIRS. Second, the required algorithms, software, analysis skills, and supporting data needed to measure, characterize and, through calibration, remove both static and quasi-static errors will be prepared prior to launch. Following the examples of Landsat 7 (USGS, 1997) and MODIS (Nishihama *et al*., 1997), this analysis suite will also include the capability to measure and characterize low-frequency errors such as thermal distortions so that corresponding modeling and calibration software can be implemented as necessary.

4. ASSUMPTIONS AND LIMITATIONS

4.1. ASSUMPTIONS

The error analysis presented in Section 3.4.1 assumed that the individual contributors to the overall VIIRS Earth location error were independent zero-mean Gaussian distributed random variables. In addition, the Earth location algorithm was developed under the assumption that the nature and magnitudes of the errors are essentially correct. The quality of the available DEM data is assumed to conform to the characteristics specified in Section 3.4.7, although this does not affect the algorithm itself, only its final performance.

The implementation of the VIIRS Earth location algorithm described in previous sections is based on the final assumption that the output product data structure will be sufficient to allow the efficient extraction of control point neighborhoods from the imagery bands for product validation.

4.2. LIMITATIONS

Several simplifying assumptions were made in the development of the VIIRS Earth location algorithm. These assumptions and their justifications are as follows:

- Ignore atmospheric refraction of the LOS - Analysis of the refraction indicates it may be as high as 30 m at the edge of a scan.
- Ignore light travel time - The maximum range to a terrestrial target seen by VIIRS is about 1800 km. This corresponds to a light travel time of 6 msec. This is a significant effect that causes as much as a 21 m bias at the edges of the scans. Later versions of the software will take this effect into account.
- Ignore velocity aberration – The relativistic deflection of the apparent instrument line-of-sight toward the spacecraft velocity vector is less than 15 meters (TBR) and does not vary greatly as a function of scan angle since the scan is nearly normal to the velocity vector. As such it can be subsumed under the pitch component of the instrument to spacecraft alignment calibration.
- Ignore the instrument telescope offset from the spacecraft center of mass - The ephemeris position represents the spacecraft center of mass rather than the instrument optical origin, but this offset is a few meters at most, which is less than the accuracy of the ephemeris data and much less than a VIIRS pixel. There is concern however that the structure has torsional and vibrational modes that may translate into larger geolocation errors.

[This page is intentionally blank]

5. REFERENCES

5.1. VIIRS DOCUMENTS

The following VIIRS documents are referenced in this ATBD using their Raytheon SBRS document number in italicized brackets, e.g., *[Y12345]*:

[EDDS154640-101]	VIIRS Command, Telemetry, Science & Engineering Data Design
[PS154640-102]	Performance Specification Algorithm Specification for the VIIRS
[Y2388]	VIIRS Software Development Plan
[Y2469]	VIIRS Context Software Architecture
[Y2479a]	VIIRS Geolocation Unit Software Architecture
[Y2487]	VIIRS Build RDR Module Level Detailed Design Document
[Y2494]	VIIRS Cloud Cover Layers Unit Level Detailed Design Document
[Y3245]	VIIRS Geolocation Unit Detailed Design

The following VIIRS documents contain information about the VIIRS design that is relevant to geolocation:

[PS154640-121]	VIS/NIR Focal Plane Subassembly NPOESS VIIIRS
[PS154640-122]	S/MWIR Focal Plane Subassembly NPOESS VIIRS
[PS154640-123]	LWIR Focal Plane Subassembly NPOESS VIIRS
[PS154640-124]	DNB Module Performance Specification NPOESS
[PS154640-360]	Digital Preprocessor Product Specification for VIIRS
[PS154640-380]	DNB Timing CCA Product Specification for VIIRS
[TP154640-001]	VIIRS System Verification and Validation Plan
[TP154640-118]	VIIRS Characterization and Calibration Plan
[Y0011855]	VIIRS Line of Sight vs. Telescope and HAM Angles
[Y12249]	NPOESS VIIRS Day-Night Band Description

5.2. NON-VIIRS DOCUMENTS

The following non-VIIRS documents are references for this ATBD:

ECS Project, 1995. *Theoretical Basis of the SDP Toolkit Geolocation Package for the ECS Project*, Technical Paper, 445-TP-002-002.

Fleig, Albert J., Paul A. Hubanks, James C. Storey and Lloyd Carpenter, 1993. *An Analysis of MODIS Earth Location Error*, Version 2.0, by MODIS Science Data Support Team (SDST).

Julian, Richard, 2003, *VIIRS Sensor Overview*, presented at the 1 October 2003 VIIRS SDR Geolocation Algorithm Continuance Meeting held at Raytheon ITSS, Upper Marlboro, Maryland.

Nishihama, Mash, Robert Wolfe, David Solomon, Frederick Patt, Jeffrey Blanchette, Albert Fleig, and Edward Masuoka, 1997. *MODIS Level 1A Earth Location: Algorithm Theoretical Basis Document*, Version 3.0, MODIS Science Data Support Team (SDST).

NIMA, 1997. NIMA TR8350.2: *Department of Defense World Geodetic System 1984 – Its Definition and Relationship with Local Geodetic Systems*, Third Edition, prepared by the NIMA WGS84 Development Committee.

NPOESS IPO, 2001, *Integrated Operational Requirements Document (IORD) II*, NPOESS Integrated Program Office.

Pratt, W.K., 1991. "*Digital Image Processing*", Second Edition, John Wiley & Sons, Inc.

Rosborough, G.W., D.G. Baldwin and W.J. Emery, 1994. "*Precise AVHRR Image Navigation*", IEEE Transaction on Geoscience and Remote Sensing, Vol 32, No. 3.

Snyder, John P., 1987. *Map Projections - A Working Manual*, United States Geological Survey (USGS) Professional Paper 1395, U. S. Government Printing Office, Washington.

USGS, 1997. *Landsat 7 Image Assessment System Geometric Algorithm Theoretical Basis Document*, Version 2, USGS EROS Data Center.

Wertz, J.R. (ed.), 1985. *Spacecraft Attitude Determination and Control*, D. Reidel Publishing Co., Vol. 73, pp 447-455.

APPENDIX A **Thermal Compensation Algorithm**

By the nature of its orbit and the operational cycling of internal components, the VIIRS instrument is subject to changes in temperature resulting in non-static thermal distortions. These thermal distortions can ultimately affect the instrument's line of sight, resulting in a measurable geolocation error.

For simplicity it is assumed that from the view of an ideal band detector, these thermal distortions all appear as a single error in effective attitude (roll, pitch and yaw). The Thermal Compensation Algorithm provides a means of correcting for these thermally induced errors by providing corrections to the instrument-to-spacecraft effective alignment (in terms of roll, pitch, and yaw) based on elements of vehicle state.

Since these errors are not localized to a single component, but are spread out over the entire optical path, instrument mountings, and attitude reference system. Most thermally induced errors will not be observable until after launch. With this in mind this thermal compensation algorithm was designed to be flexible enough to cover a large number of possible scenarios, and to be updateable throughout the life of the instrument by an off-line process capable of quantifying the geolocation accuracy of the instrument.

It achieves this flexibility by using a combination of Look-up Tables (LUTs) and correction-coefficient sets. The LUTs define the discrete conditions that a certain set of correction-coefficients will be used. The correction-coefficients are then applied to determine the required correction in terms of other more continuous conditions. The flexibility of the LUT layout allows the near real time operational processing system to be designed so that the updates from the offline correction process will not impact the processing software.

DESCRIPTION OF ALGORITHM

The near real time operational processing algorithm for the thermal geolocation correction is based on a two stage approach that converts an *input vector* containing various geometric and thermal metadata values into the final three element vector containing roll, pitch, and yaw corrections. The first stage of the process samples and/or weights the values in the input vector and produces a quantized integer index value for each defined dimension of the *Correction Coefficient LUT.* The number of dimensions used to characterize the instrument state is parameterized within the table. The offline process can later determine the required complexity to properly fit the needed geometric corrections. The quantized index values are used to extract a single correction index value from a *Correction Index LUT* to access the proper group of coefficient sets from the *Correction Coefficient LUT*. The second stage of the process samples and/or weights the input vector values to generate the floating-point values used in the specified functional equations to calculate the final correction factors.

Figure A-1 shows the first stage process of using the current instrument state in the form of the *input vector* in conjunction with metadata contained in the *Correction Index LUT*'s header to retrieve an index value to access the proper coefficient group that is associated

with the instrument's current state.

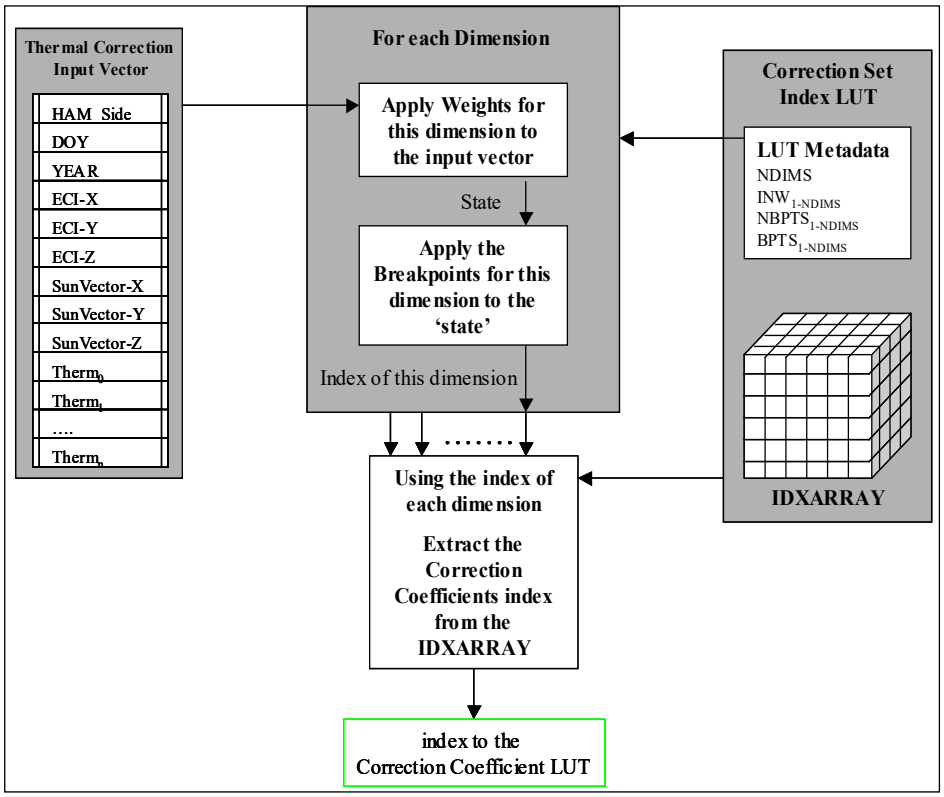

Figure A-1: Correction Index LUT Usage

Figure A-2 shows the second stage process of using the index value determined in the first stage to select a corresponding set of coefficients from the *Correction Coefficient LUT*. Metadata, contained in the header of the *Correction Coefficient LUT*, describes how to apply the *input vector* to the retrieved coefficients in order to calculate the corrections to effective roll, pitch and yaw.

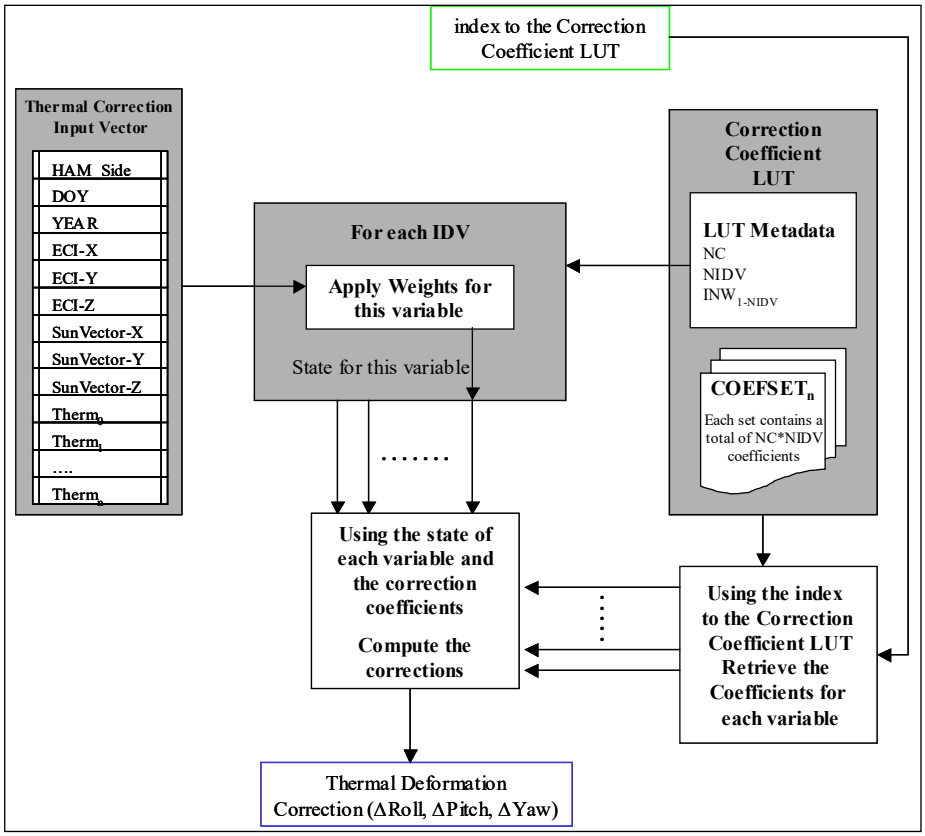

Figure A-2: Correction Coefficient LUT Usage

LUT GENERATION

After the offline analysis of the collected data is performed the *Correction Index LUT*, the *Correction Coefficient LUTs* can be populated. In order to illustrate the LUT generation process, a hypothetical example using the results of the method described in Section 3.4.9 is given below. The data illustrated in the following examples is similar to the errors observed with the MODIS sensor. Each example builds on the previous example showing how the LUTS can be updated, as more information is made available.

Example 1: Initial LUT generation

Observations made over a 16-day period using the method of Section 3.4.9 reveal the following errors as function of latitude. Since latitude is not a member of the *input-vector* The ECI-Z term is used to estimate the latitude range.

For this first example the discrete measured corrections will be applied over the ranges of ECI-Z indicated in the table of Figure A-3. A zero correction will be applied to regions where no data are available (Latitude < -40° and Latitude > 50°).

Errors in Effective Attitude as function of ECI-Z vector

Day017-032

ECI-Z Range (km)		Mid-ECI-Z (km)	Latitude Range		Mid-Lat	Mean Track Shift (m)	Mean scan shift (m)	Effective Pitch (urad)	Effective Roll (urad)
-4551.03	-3539.94	-4060.92	-40	-30	-35	10.717537	-4.711736	15.20	-6.68
-3539.94	-2421.40	-2992.04	-30	-20	-25	3.58734	18.077482	5.09	25.64
-2421.40	-1229.36	-1832.34	-20	-10	-15	-16.544576	19.293688	-23.47	27.37
-1229.36	0.00	-617.02	-10	0	-5	23.735449	-10.449365	33.67	-14.82
0.00	1229.36	617.02	0	10	5	20.515838	9.804958	29.10	13.91
1229.36	2421.40	1832.34	10	20	15	37.430011	9.055189	53.09	12.84
2421.40	3539.94	2992.04	20	30	25	7.253063	-31.021553	10.29	-44.00
3539.94	4551.03	4060.92	30	40	35	0.621592	-20.369467	0.88	-28.89
4551.03	5423.98	5006.54	40	50	45	3.06274	-29.221335	4.34	-41.45

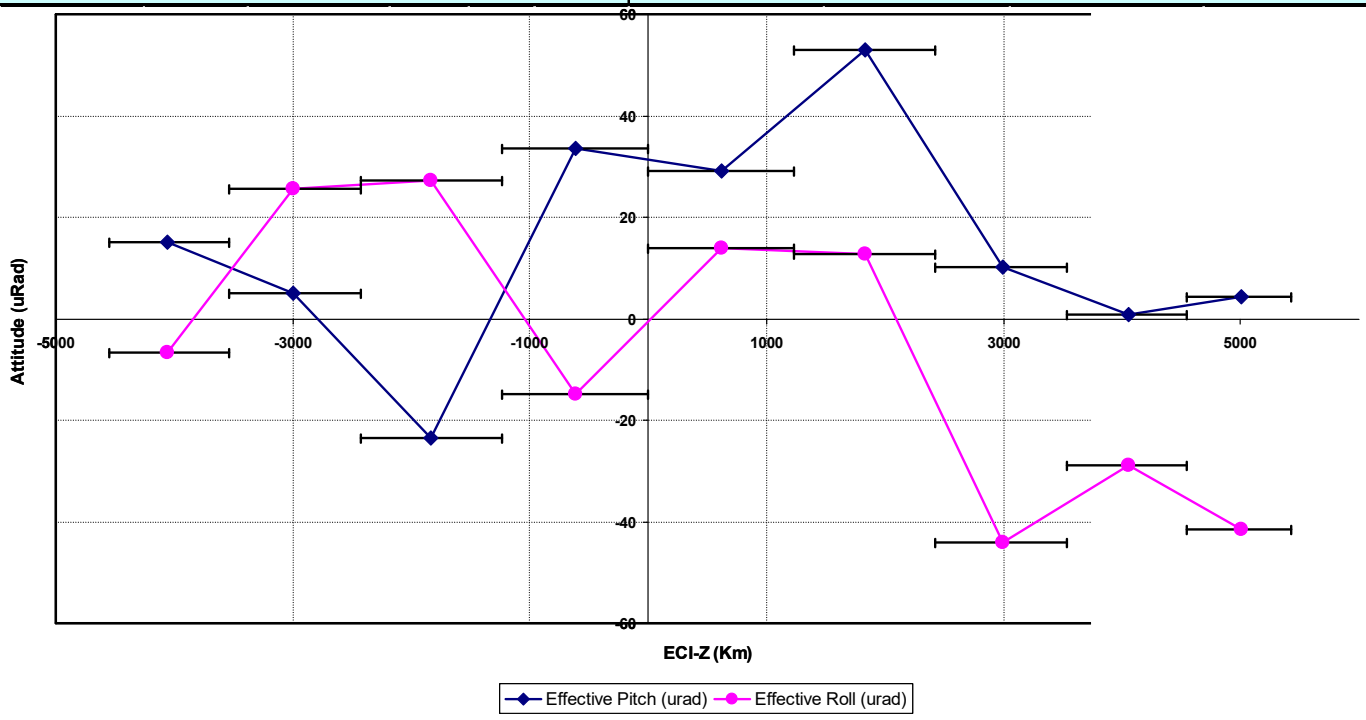

Figure A-3: Errors in Effective Attitude as a Function of the ECI-Z Vector

Population of the Correction Index LUT

1. First the number of dimensions (NDIMS) is defined. For this example, only one dimension is required. (NDIMS=1)
2. Set the weighting vector (INW) for dimension 1. Within the input-vector, the only term we are interested in for this correction is the ECI-Z term, which is index 5. Thus, the weighting vector will contain the value 1.0 at index 5 and 0.0 everywhere else as shown in Table A-1.

Table A-1: Weighting Vector Example

Index	0	1	2	3	4	5	6	….	NUM_INPUTS-1
Weight	0.0	0.0	0.0	0.0	0.0	1.0	0.0	…	0.0

3. Set the number of breakpoints (NBPTS) for this dimension. There are nine explicit ranges provided from the offline analysis. There are two additional ranges off each

end of the data-set (*-40* ° to -∞ and *50* ° to +∞) for which no error values are available. This gives a total of eleven ranges. The number of breakpoints will be (NBPTS=*11-1=10*)

4. Define each breakpoint (BPTS). Breakpoints are given for the eleven ranges illustrated in Table A-2. Only ten actual values are needed to describe these ranges. These 10 values make up the Breakpoint vector.

Table A-2: Breakpoints Example

Quantized index value	Range <= ECI-Z <		Breakpoints	
0	-∞	-4551.03	-∞	$BPTS_1[0]$
1	-4551.03	-3539.94	$BPTS_1[0]$	$BPTS_1[1]$
2	-3539.94	-2421.40	$BPTS_1[1]$	$BPTS_1[2]$
3	-2421.40	-1229.36	$BPTS_1[2]$	$BPTS_1[3]$
4	-1229.36	0.00	$BPTS_1[3]$	$BPTS_1[4]$
5	0.00	1229.36	$BPTS_1[4]$	$BPTS_1[5]$
6	1229.36	2421.40	$BPTS_1[5]$	$BPTS_1[6]$
7	2421.40	3539.94	$BPTS_1[6]$	$BPTS_1[7]$
8	3539.94	4551.03	$BPTS_1[7]$	$BPTS_1[8]$
9	4551.03	5423.98	$BPTS_1[8]$	$BPTS_1[9]$
10	5423.98	∞	$BPTS_1[9]$	∞

5. Next the index values to the *Correction Coefficient LUT* are defined. The total size of this table is given by multiplying NBPTS+1 for each dimension (NDIMS) of the LUT. Since this is a one-dimensional table with eleven entries the LUT is only eleven entries in size. The correction value to be used for each of these entries is illustrated in Table A-3 (Note: Corrections are the negative of the error).

   Due to the index states of 0 and 10 resulting in the same correction, they are both pointed to the same entry in the *Correction Coefficient LUT.* As the size of the tables increase, due to the addition of new data, it is likely that more identical values would be observed. Grouping these values under a single entry in the *Correction Coefficient LUT* helps reduce the size of the LUT. In extreme cases it may be helpful to further reduce the size of the *Correction Coefficient LUT* by grouping corrections that are not identical but are very close to each other into a single correction.

Table A-3: Index Example

IDXARRAY Index	Corrections to effective			Index into *Correction Coefficient LUT*
	Roll	Pitch	Yaw	
0	0.0	0.0	0.0	0
1	6.683313475	-15.20218014	0.0	1
2	-25.64181844	-5.088425532	0.0	2
3	-27.36693334	23.46748369	0.0	3
4	14.82179433	-33.66730355	0.0	4

5	-13.90774184	-29.10047944	0.0	5
6	-12.84423972	-53.09221421	0.0	6
7	44.00220285	-10.28803262	0.0	7
8	28.892861	-0.88169078	0.0	8
9	41.44870214	-4.344312057	0.0	9
10	0.0	0.0	0.0	0

6. The LUT can now be populated with the data given above. The final result should look something like Table A-4.

Table A-4: Results Example

NAME	Format	Value
TBLIDENT	char[80]	Example-1
TBLGENINFO	char[80]	Correction in ECI-Z for days a-b
NDIMS	Byte	1
INW_1	float[NUM_INPUTS]	[0.0, 0.0, 0.0, 0.0, 0.0, 1.0, 0.0, …, 0.0]
$NBPTS_1$	Uint	10
$BPTS_1$	float[NBPTS]	[-4551.03, -3539.94, -2421.40, -1229.36, 0.00, 1229.36, 2421.40, 3539.94, 4551.03, 5423.98]
IDXARRAY		[0, 1, 2, 3, 4, 5, 6, 7, 8, 9, 0]

Population of the Correction Coefficient LUT

1. Set the number of coefficients (NC). Since this correction is purely a discrete correction only the DC component of the correction function is used. Thus NC=1.
2. Set the number of independent variables (NIDV). Once again this is a table of discrete corrections and only the DC component of the correction function is used. This means that the function is not dependent on any variable of the input-vector and NIDV=0.
3. Since NIDV=0 there are no input weighting coefficients.
4. Set the number of entries (NENTRIES) for this table there are ten entries, one for each set of correction terms, using the index values of 0 through 9.
5. Populate the coefficient sets (COEFSET) there are ten coefficient sets numbered 0 through 9. Each set consists of either 3*NC*NIDV coefficients or 3*NC coefficients if NIDV is equal to zero. For this LUT, NIDV equals zero, thus there are 3*1 coefficients per set. The layout of the coefficient sets for this portion of the LUT is shown in Table A-5.

Table A-5: Cofficient Sets Example

Set Index	Roll C_0	Pitch C_0	Yaw C_0
0	0.0	0.0	0.0

1	6.683313475	-15.20218014	0.0
2	-25.64181844	-5.088425532	0.0
3	-27.36693334	23.46748369	0.0
4	14.82179433	-33.66730355	0.0
5	-13.90774184	-29.10047944	0.0
6	-12.84423972	-53.09221421	0.0
7	44.00220285	-10.28803262	0.0
8	28.892861	-0.88169078	0.0
9	41.44870214	-4.344312057	0.0

6. The full LUT can now be populated with the data given above. The final result should look something like Table A-6.

This provides an initial set of LUTs capable of applying discrete corrections over a limited period. Additional corrections must be added to the LUT over time to account for seasonal changes.

Table A-6: Final Results Example

Name	Format	Value
TBLIDENT	char[80]	Example-1
TBLGENINFO	char[80]	Correction in ECI-Z for days a-b
NC	Byte	1
NIDV	Byte	0
NENTRIES	Uint	10
$COEFSET_0$	float[***coef_per_set*****]	[0.0, 0.0, 0.0]
$COEFSET_1$	float[***coef_per_set*****]	[6.683313475, -15.20218014, 0.0]
$COEFSET_2$	float[***coef_per_set*****]	[-25.64181844, -5.088425532, 0.0]
$COEFSET_3$	float[***coef_per_set*****]	[-27.36693334, 23.46748369, 0.0]
$COEFSET_4$	float[***coef_per_set*****]	[14.82179433, -33.66730355, 0.0]
$COEFSET_5$	float[***coef_per_set*****]	[-13.90774184, -29.10047944, 0.0]
$COEFSET_6$	float[***coef_per_set*****]	[-12.84423972, -53.09221421, 0.0]
$COEFSET_7$	float[***coef_per_set*****]	[44.00220285, -10.28803262, 0.0]
$COEFSET_8$	float[***coef_per_set*****]	[28.892861, -0.88169078, 0.0]
$COEFSET_9$	float[***coef_per_set*****]	[41.44870214, -4.344312057, 0.0]
** if NIDV>0, ***coef_per_set*** =NIDV*NC*3 else ***coef_per_set*** =NC*3		

Example 2: Growing the LUT

This example assumes that the analysis used to obtain the data illustrated in Figure A-3 is repeated once every 30 days. This example illustrates the updates that must be made to add two additional correction periods to the LUTS.

Additions to the Correction Index LUT

1. Add another dimension to the Correction Index LUT to account for the day of year (NDIMS=2).
2. The input weighting vector for dimension 1 (ECI-Z) remains the same
3. The breakpoints vector for dimension 1 (ECI-Z) remains the same
4. Add an input weighting vector (INW) for dimension 2 in terms of the day of year (DOY). Using the description of the input vector given in section-X the DOY term is stored at index –1 of the input vector. Thus, the weighting vector will contain the value 1.0 at index 1 and 0.0 everywhere else as shown in Table A-7.

Table A-7: Weighting Vector - Example 2

Index	0	1	2	3	4	5	6	….	NUM_INPUTS-1
Weight	0.0	1.0	0.0	0.0	0.0	0.0	0.0	…	0.0

5. Add the breakpoints vector for dimension 2. This vector is in terms of DOY and is broken down into 30-day segments for three time periods as in Table A-8.

Table A-8: Breakpoints Vector - Example 2

Data collection days	Quantized value	Correction use Range <= DOY <	
17-32	0	-∞	32
37-62	1	32	62
67-92	2	62	∞

6. Next the index values to the *Correction Coefficient LUT* are defined. The total size of this table is given by multiplying NBPTS+1 for each dimension (NDIMS) of the LUT. Sine this is now a two-dimensional table with 11 entries in dimension 1 and 3 entries in dimension 2 the LUT is 3*11=33 entries in size. The correction value to be used for each of these entries is illustrated in Table A-9. The portion of the table from the previous example is shaded cyan. The new data from the 2 new periods is shown as the An, Bn, Cn, and Dn entries.

Table A-9: Corrections - Example 2

IDXARRAY (Dim1,Dim2)	Corrections to effective			Index into *Correction Coefficient LUT*
	Roll	Pitch	Yaw	
0,0	0.0	0.0	0.0	0
1,0	6.683313475	-15.20218014	0.0	1
2,0	-25.64181844	-5.088425532	0.0	2

3,0	-27.36693334	23.46748369	0.0	3
4,0	14.82179433	-33.66730355	0.0	4
5,0	-13.90774184	-29.10047944	0.0	5
6,0	-12.84423972	-53.09221421	0.0	6
7,0	44.00220285	-10.28803262	0.0	7
8,0	28.892861	-0.88169078	0.0	8
9,0	41.44870214	-4.344312057	0.0	9
10,0	0.0	0.0	0.0	0
0,1	0.0	0.0	0.0	0
1,1	A1	B1	0.0	10
2,1	A2	B2	0.0	11
3,1	A3	B3	0.0	12
4,1	A4	B4	0.0	13
5,1	A5	B5	0.0	14
6,1	A6	B6	0.0	15
7,1	A7	B7	0.0	16
8,1	A8	B8	0.0	17
9,1	A9	B9	0.0	18
10,1	0.0	0.0	0.0	0
0,2	0.0	0.0	0.0	0
1,2	C1	D1	0.0	19
2,2	C2	D2	0.0	20
3,2	C3	D3	0.0	21
4,2	C4	D4	0.0	22
5,2	C5	D5	0.0	23
6,2	C6	D6	0.0	24
7,2	C7	D7	0.0	25
8,2	C8	D8	0.0	26
9,2	C9	D9	0.0	27
10,2	0.0	0.0	0.0	0

7. The LUT can now be populated with the data given above. The final result should look something like the following table below.

Table A-10: Final Result - Example 2

NAME	Format	Value
TBLIDENT	char[80]	Example-2
TBLGENINFO	char[80]	Correction in ECI-Z over 3-month period
NDIMS	Byte	1
INW_0	float[NUM_INPUTS]	[0.0, 0.0, 0.0, 0.0, 0.0, 1.0, 0.0, …, 0.0]
$NBPTS_0$	Uint	10
$BPTS_0$	float[NBPTS]	[-4551.03, -3539.94, -2421.40, -1229.36, 0.00, 1229.36, 2421.40, 3539.94, 4551.03, 5423.98]
INW_1	float[NUM_INPUTS]	[0.0, 1.0, 0.0, 0.0, 0.0, 0.0, 0.0, …, 0.0]
$NBPTS_1$	Uint	2
$BPTS_1$	float[NBPTS]	[32, 62]
IDXARRAY		[0, 1, 2, 3, 4, 5, 6, 7, 8, 9, 0 0, 10, 11, 12, 13, 14, 15, 16, 17, 18, 0 0, 19, 20, 21, 22, 23, 24, 25, 26, 27, 0]

Additions to the Correction Coefficient LUT

1. The additions to the *Correction Coefficient LUT* section are minor at this point. First

change the number of entries (NENTRIES) to 28, to account for the 18 additional entries in the LUT.

2. Next add the additional coefficient sets. The first 10 entries were defined in Example 1.
3. The full coefficient LUT can now be populated with the data given in Table A-11. The final result should look something like Table A-12.

Table A-11: Coefficient Sets - Example 2

Set Index	Roll C_0	Pitch C_0	Yaw C_0
0	0.0	0.0	0.0
1	6.683313475	-15.20218014	0.0
2	-25.64181844	-5.088425532	0.0
3	-27.36693334	23.46748369	0.0
4	14.82179433	-33.66730355	0.0
5	-13.90774184	-29.10047944	0.0
6	-12.84423972	-53.09221421	0.0
7	44.00220285	-10.28803262	0.0
8	28.892861	-0.88169078	0.0
9	41.44870214	-4.344312057	0.0
10	A1	B1	0.0
11	A2	B2	0.0
12	A3	B3	0.0
13	A4	B4	0.0
14	A5	B5	0.0
15	A6	B6	0.0
16	A7	B7	0.0
17	A8	B8	0.0
18	A9	B9	0.0
19	C1	D1	0.0
20	C2	D2	0.0
21	C3	D3	0.0
22	C4	D4	0.0
23	C5	D5	0.0
24	C6	D6	0.0
25	C7	D7	0.0
26	C8	D8	0.0
27	C9	D9	0.0

Table A-12: Coefficient Result - Example 2

Name	Format	Value
TBLIDENT	char[80]	Example-2
TBLGENINFO	char[80]	Correction in ECI-Z for multiple time periods
NC	Byte	1
NIDV	Byte	0
NENTRIES	Uint	28
$COEFSET_0$	float[***coef_per_set****]	[0.0, 0.0, 0.0]
$COEFSET_1$	float[***coef_per_set****]	[6.683313475, -15.20218014, 0.0]
$COEFSET_2$	float[***coef_per_set****]	[-25.64181844, -5.088425532, 0.0]
$COEFSET_3$	float[***coef_per_set****]	[-27.36693334, 23.46748369, 0.0]
$COEFSET_4$	float[***coef_per_set****]	[14.82179433, -33.66730355, 0.0]
$COEFSET_5$	float[***coef_per_set****]	[-13.90774184, -29.10047944, 0.0]
$COEFSET_6$	float[***coef_per_set****]	[-12.84423972, -53.09221421, 0.0]
$COEFSET_7$	float[***coef_per_set****]	[44.00220285, -10.28803262, 0.0]
$COEFSET_8$	float[***coef_per_set****]	[28.892861, -0.88169078, 0.0]
$COEFSET_9$	float[***coef_per_set****]	[41.44870214, -4.344312057, 0.0]
$COEFSET_{10}$	float[***coef_per_set****]	[A1, B1, 0.0]
$COEFSET_{11}$	float[***coef_per_set****]	[A2, B2, 0.0]
$COEFSET_{12}$	float[***coef_per_set****]	[A3, B3, 0.0]
$COEFSET_{13}$	float[***coef_per_set****]	[A4, B4, 0.0]
$COEFSET_{14}$	float[***coef_per_set****]	[A5, B5, 0.0]
$COEFSET_{15}$	float[***coef_per_set****]	[A6, B6, 0.0]
$COEFSET_{16}$	float[***coef_per_set****]	[A7, B7, 0.0]
$COEFSET_{17}$	float[***coef_per_set****]	[A8, B8, 0.0]
$COEFSET_{18}$	float[***coef_per_set****]	[A9, B9, 0.0]
$COEFSET_{19}$	float[***coef_per_set****]	[C1, D1, 0.0]
$COEFSET_{20}$	float[***coef_per_set****]	[C2, D2, 0.0]
$COEFSET_{21}$	float[***coef_per_set****]	[C3, D3, 0.0]
$COEFSET_{22}$	float[***coef_per_set****]	[C4, D4, 0.0]
$COEFSET_{23}$	float[***coef_per_set****]	[C5, D5, 0.0]
$COEFSET_{24}$	float[***coef_per_set****]	[C6, D6, 0.0]
$COEFSET_{25}$	float[***coef_per_set****]	[C7, D7, 0.0]
$COEFSET_{26}$	float[***coef_per_set****]	[C8, D8, 0.0]
$COEFSET_{27}$	float[***coef_per_set****]	[C9, D9, 0.0]

This example illustrates how another dimension can be added to take into account additional effects. Any number of dimensions can be added with any desired sampling. However this can be rather cumbersome for large data sets. In cases where the data is well behaved; sinusoidal, polynomial and exponential functions are available to compute more continuous corrections.

Example 3: Using the correction functions

Long-term trend analysis of MODIS reveals that a sinusoidal error with period of one-year is responsible for the seasonal changes in geolocation accuracy. This error is further compounded by a seemingly continuous but slowly varying linear bias as illustrated in Figure A-4. It is believed that this bias variation is not related to thermal state but due to longer-term aging of the instrument or variations in the alignment tracking system.

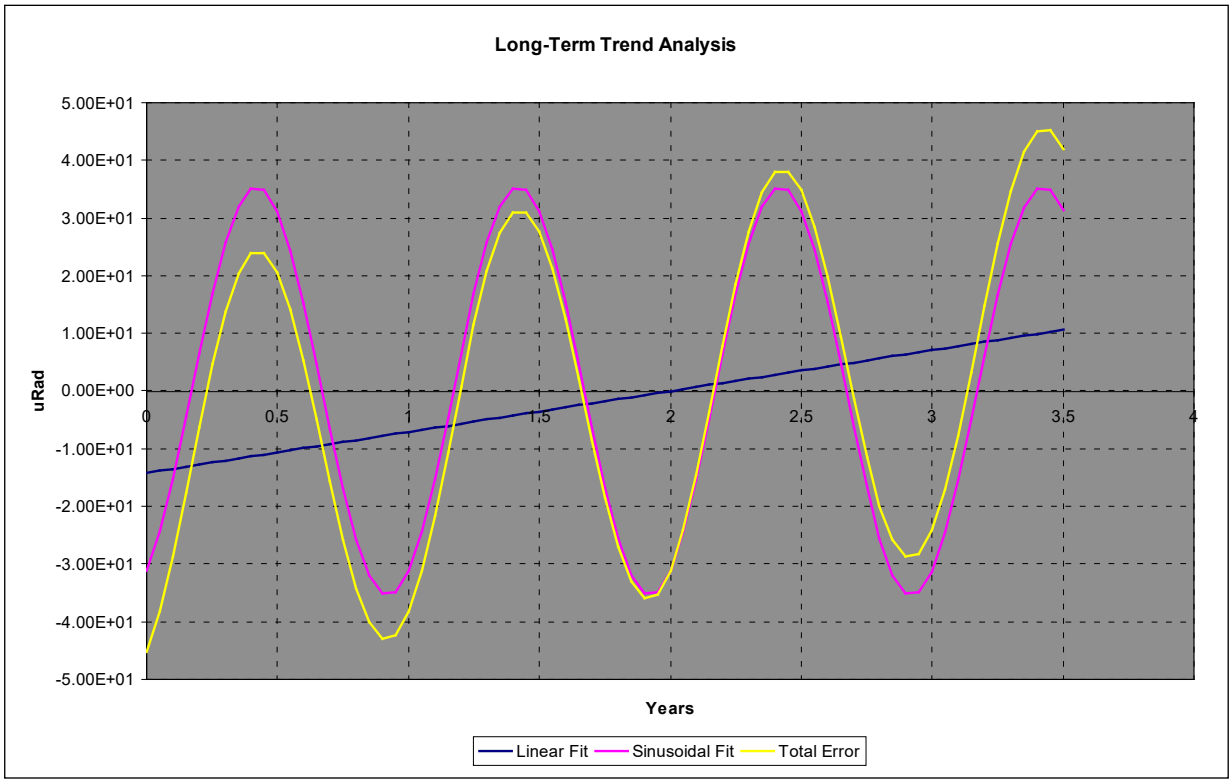

Figure A-4: Seasonal Geolocation Errors

Fits to the data indicate the following functional form for the errors in roll. For simplicity the same errors are duplicated for pitch.

roll (year)= -14.2 + (year*7.09) + 35.2*sin(year*2□+5.2124)

pitch(year)= -14.2 + (year*7.09) + 35.2*sin(year*2□+5.2124)

These two equations will be split and configured with two independent variables derived from the input vector values instead of the relative year variable from the plot.

Changes to the Correction Index LUT

Since the functional forms represent all the seasonal variations observed the *Correction Index LUT* is taken back to a single dimension to account for orbital variations only. It is populated exactly as in Example 1 (see Table A-4).

Changes to the Correction Coefficiet LUT

The *Correction Coefficient LUT* must now implement the two correction equations given above, as well as the discrete corrections due to the orbital temperature variations implemented in Example 1.

1. Set the number of coefficients (NC). Both equations can be computed using the correction function

$$f(x)=C_0 + C_1*\sin(C_2x+C_3) * \exp(C_4*x+C_5) + C_6\exp(C_7*x+C_8) + C_9*x^1$$

To configure the correction function for this example, set NC=10. Note if multiple correction functions of different sizes are required then always set NC to the highest number of coefficients and set all unneeded coefficients to zero.

2. Set the number of independent variables (NIDV). For this example NIDV is set to 2. You can technically do it with one, but this better illustrates the flexibility of the algorithm.
3. Set the input weighting vector (INWVECT) for each independent variable
    a. Since the sine term is yearly periodic it can be driven by the daily fraction of a year found by dividing the day of the year by 365 to make the C_2 equal to 2π. The daily year fraction will be listed as the x variable in the coefficient equations. The resultant weighting vector is shown in Table A-13.

Table A-13: X Variable Weighting Vector - Example 3

Index	0	1	2	3	4	5	6	….	NUM_INPUTS-1
Weight	0.0	1/365	0.0	0.0	0.0	0.0	0.0	…	0.0

    b. The ramp component is not periodic but shows a continuous change in bias for the geolocation accuracy. This term must be driven by the total fraction year calculated as (YEAR+DOY/365). The total yearly fraction will be listed as the y variable in the coefficient equations. Its weighting vector is shown in Table A-14.

Table A-14: Y Variable Weighting Vector - Example 3

Index	0	1	2	3	4	5	6	….	NUM_INPUTS-1
Weight	0.0	1/365	1.0	0.0	0.0	0.0	0.0	…	0.0

4. The number of entries (NENTRIES) remains the same as that of Example 1, (NENTRIES=10)
5. Populate the coefficient sets (COEFSET). There are 10 coefficient sets numbered 0 through 9. For this example, each set consists of 3*NC*NIDV=60 coefficients, most of which are zero. The non-zero terms of the coefficient sets for this LUT is shown in Table A-15.

$$\mathbf{Roll_{total} = Roll(x) + Roll(y)}$$

$$\mathbf{Roll(x) = C_1 * \sin(C_2 x + C_3)}$$

$$\mathbf{Roll(y) = C_0 + C_9 * x^1}$$

Table A-15: Non-zero Terms - Example 3

Set Index	Roll(x) C_1, C_2, C_3	Roll(y) C_0, C_9	Pitch(x) C_1, C_2, C_3	Pitch(y) C_0, C_9	Yaw(x) Yaw(y)

0	-35.2, 2π, 5.2	G1, -7.09	-35.2, 2π, 5.2	H1, -7.09	All Coefficients are zero
1	-35.2, 2π, 5.2	G2, -7.09	-35.2, 2π, 5.2	H2, -7.09	
2	-35.2, 2π, 5.2	G3, -7.09	-35.2, 2π, 5.2	H3, -7.09	
3	-35.2, 2π, 5.2	G4, -7.09	-35.2, 2π, 5.2	H4, -7.09	
4	-35.2, 2π, 5.2	G5, -7.09	-35.2, 2π, 5.2	H5, -7.09	
5	-35.2, 2π, 5.2	G6, -7.09	-35.2, 2π, 5.2	H6, -7.09	
6	-35.2, 2π, 5.2	G7, -7.09	-35.2, 2π, 5.2	H7, -7.09	
7	-35.2, 2π, 5.2	G8, -7.09	-35.2, 2π, 5.2	H8, -7.09	
8	-35.2, 2π, 5.2	G9, -7.09	-35.2, 2π, 5.2	H9, -7.09	
9	-35.2, 2π, 5.2	G10, -7.09	-35.2, 2π, 5.2	H10, -7.09	

Note: the G and H terms represent the sum of the discrete orbital induced errors as illustrated in Example 1 along with the offset values determined by the reference year from the input vector. The fit in Figure A-3 had a 0 year reference starting point. The offsets in Figure A-3 also had the discrete orbital induced errors removed before the linear and sinusoidal fits were applied.

6. The *Correction Coefficient LUT* can now be populated with the above information as shown in Table A-16.

Table A-16: Coefficient LUT - Example 3

Name	Format	Value
TBLIDENT	char[80]	Example-1
TBLGENINFO	char[80]	Correction in ECI-Z for days a-b
NC	Byte	10
NIDV	Byte	2
$INWVECT_0$	float[NUM_INPUTS]	[0.0, 1/365, 0.0, ……. 0.0]
$INWVECT_1$	float[NUM_INPUTS]	[0.0, 1/365, 1.0, ……. 0.0]
NENTRIES	uint	10
$COEFSET_0$	float[***coef_per_set*****]	[0.0, -35.2, 2π, 5.2, 0.0, 0.0, 0.0, 0.0, 0.0, 0.0 14.2, 0.0, 0.0, 0.0, 0.0, 0.0, 0.0, 0.0, 0.0, G1] [0.0, -35.2, 2π, 5.2, 0.0, 0.0, 0.0, 0.0, 0.0, 0.0 14.2, 0.0, 0.0, 0.0, 0.0, 0.0, 0.0, 0.0, 0.0, H1] [0.0, 0.0, 0.0, 0.0, 0.0, 0.0, 0.0, 0.0, 0.0, 0.0 0.0, 0.0, 0.0, 0.0, 0.0, 0.0, 0.0, 0.0, 0.0, 0.0]
$COEFSET_1$	float[***coef_per_set*****]	[0.0, -35.2, 2π, 5.2, 0.0, 0.0, 0.0, 0.0, 0.0, 0.0 14.2, 0.0, 0.0, 0.0, 0.0, 0.0, 0.0, 0.0, 0.0, G2] [0.0, -35.2, 2π, 5.2, 0.0, 0.0, 0.0, 0.0, 0.0, 0.0 14.2, 0.0, 0.0, 0.0, 0.0, 0.0, 0.0, 0.0, 0.0,H2] [0.0, 0.0, 0.0, 0.0, 0.0, 0.0, 0.0, 0.0, 0.0, 0.0 0.0, 0.0, 0.0, 0.0, 0.0, 0.0, 0.0, 0.0, 0.0, 0.0]
$COEFSET_2$	float[***coef_per_set*****]	[0.0, -35.2, 2π, 5.2, 0.0, 0.0, 0.0, 0.0, 0.0, 0.0 14.2, 0.0, 0.0, 0.0, 0.0, 0.0, 0.0, 0.0, 0.0, G3] [0.0, -35.2, 2π, 5.2, 0.0, 0.0, 0.0, 0.0, 0.0, 0.0 14.2, 0.0, 0.0, 0.0, 0.0, 0.0, 0.0, 0.0, 0.0, H3] [0.0, 0.0, 0.0, 0.0, 0.0, 0.0, 0.0, 0.0, 0.0, 0.0 0.0, 0.0, 0.0, 0.0, 0.0, 0.0, 0.0, 0.0, 0.0, 0.0]
$COEFSET_3$	float[***coef_per_set*****]	[0.0, -35.2, 2π, 5.2, 0.0, 0.0, 0.0, 0.0, 0.0, 0.0 14.2, 0.0, 0.0, 0.0, 0.0, 0.0, 0.0, 0.0, 0.0, G4] [0.0, -35.2, 2π, 5.2, 0.0, 0.0, 0.0, 0.0, 0.0, 0.0 14.2, 0.0, 0.0, 0.0, 0.0, 0.0, 0.0, 0.0, 0.0, H4] [0.0, 0.0, 0.0, 0.0, 0.0, 0.0, 0.0, 0.0, 0.0, 0.0 0.0, 0.0, 0.0, 0.0, 0.0, 0.0, 0.0, 0.0, 0.0, 0.0]
$COEFSET_4$	float[***coef_per_set*****]	[0.0, -35.2, 2π, 5.2, 0.0, 0.0, 0.0, 0.0, 0.0, 0.0 14.2, 0.0, 0.0, 0.0, 0.0, 0.0, 0.0, 0.0, 0.0, G5] [0.0, -35.2, 2π, 5.2, 0.0, 0.0, 0.0, 0.0, 0.0, 0.0 14.2, 0.0, 0.0, 0.0, 0.0, 0.0, 0.0, 0.0, 0.0, H5] [0.0, 0.0, 0.0, 0.0, 0.0, 0.0, 0.0, 0.0, 0.0, 0.0 0.0, 0.0, 0.0, 0.0, 0.0, 0.0, 0.0, 0.0, 0.0, 0.0]
$COEFSET_5$	float[***coef_per_set*****]	[0.0, -35.2, 2π, 5.2, 0.0, 0.0, 0.0, 0.0, 0.0, 0.0 14.2, 0.0, 0.0, 0.0, 0.0, 0.0, 0.0, 0.0, 0.0, G6] [0.0, -35.2, 2π, 5.2, 0.0, 0.0, 0.0, 0.0, 0.0, 0.0 14.2, 0.0, 0.0, 0.0, 0.0, 0.0, 0.0, 0.0, 0.0, H6] [0.0, 0.0, 0.0, 0.0, 0.0, 0.0, 0.0, 0.0, 0.0, 0.0 0.0, 0.0, 0.0, 0.0, 0.0, 0.0, 0.0, 0.0, 0.0, 0.0]
$COEFSET_6$	float[***coef_per_set*****]	[0.0, -35.2, 2π, 5.2, 0.0, 0.0, 0.0, 0.0, 0.0, 0.0 14.2, 0.0, 0.0, 0.0, 0.0, 0.0, 0.0, 0.0, 0.0, G7] [0.0, -35.2, 2π, 5.2, 0.0, 0.0, 0.0, 0.0, 0.0, 0.0 14.2, 0.0, 0.0, 0.0, 0.0, 0.0, 0.0, 0.0, 0.0, H7] [0.0, 0.0, 0.0, 0.0, 0.0, 0.0, 0.0, 0.0, 0.0, 0.0 0.0, 0.0, 0.0, 0.0, 0.0, 0.0, 0.0, 0.0, 0.0, 0.0]
$COEFSET_7$	float[***coef_per_set*****]	[0.0, -35.2, 2π, 5.2, 0.0, 0.0, 0.0, 0.0, 0.0, 0.0 14.2, 0.0, 0.0, 0.0, 0.0, 0.0, 0.0, 0.0, 0.0, G8] [0.0, -35.2, 2π, 5.2, 0.0, 0.0, 0.0, 0.0, 0.0, 0.0 14.2, 0.0, 0.0, 0.0, 0.0, 0.0, 0.0, 0.0, 0.0, H8] [0.0, 0.0, 0.0, 0.0, 0.0, 0.0, 0.0, 0.0, 0.0, 0.0 0.0, 0.0, 0.0, 0.0, 0.0, 0.0, 0.0, 0.0, 0.0, 0.0]
$COEFSET_8$	float[***coef_per_set*****]	[0.0, -35.2, 2π, 5.2, 0.0, 0.0, 0.0, 0.0, 0.0, 0.0 14.2, 0.0, 0.0, 0.0, 0.0, 0.0, 0.0, 0.0, 0.0, G9] [0.0, -35.2, 2π, 5.2, 0.0, 0.0, 0.0, 0.0, 0.0, 0.0 14.2, 0.0, 0.0, 0.0, 0.0, 0.0, 0.0, 0.0, 0.0, H9] [0.0, 0.0, 0.0, 0.0, 0.0, 0.0, 0.0, 0.0, 0.0, 0.0 0.0, 0.0, 0.0, 0.0, 0.0, 0.0, 0.0, 0.0, 0.0, 0.0]
$COEFSET_9$	float[***coef_per_set*****]	[0.0, -35.2, 2π, 5.2, 0.0, 0.0, 0.0, 0.0, 0.0, 0.0 14.2, 0.0, 0.0, 0.0, 0.0, 0.0, 0.0, 0.0, 0.0, G10] [0.0, -35.2, 2π, 5.2, 0.0, 0.0, 0.0, 0.0, 0.0, 0.0 14.2, 0.0, 0.0, 0.0, 0.0, 0.0, 0.0, 0.0, 0.0, H10] [0.0, 0.0, 0.0, 0.0, 0.0, 0.0, 0.0, 0.0, 0.0, 0.0 0.0, 0.0, 0.0, 0.0, 0.0, 0.0, 0.0, 0.0, 0.0, 0.0]
** if NIDV>0, ***coef_per_set*** =NIDV*NC*3 else ***coef_per_set*** =NC*3		

Example 4: Piecewise Correction Functions

The following example further builds upon the previous three examples by applying a piecewise polynomial correction for the error induced by the orbital motion of the instrument.

The correction curves, generated from the data presented in Figure A-3, can be fit relatively well using piecewise polynomial functions. The results of this fitting process are illustrated in Figure A-5.

Table A-17 indicates the ECI-Z range for which the polynomial coefficients are valid. No data are available outside of this range so no correction will be performed.

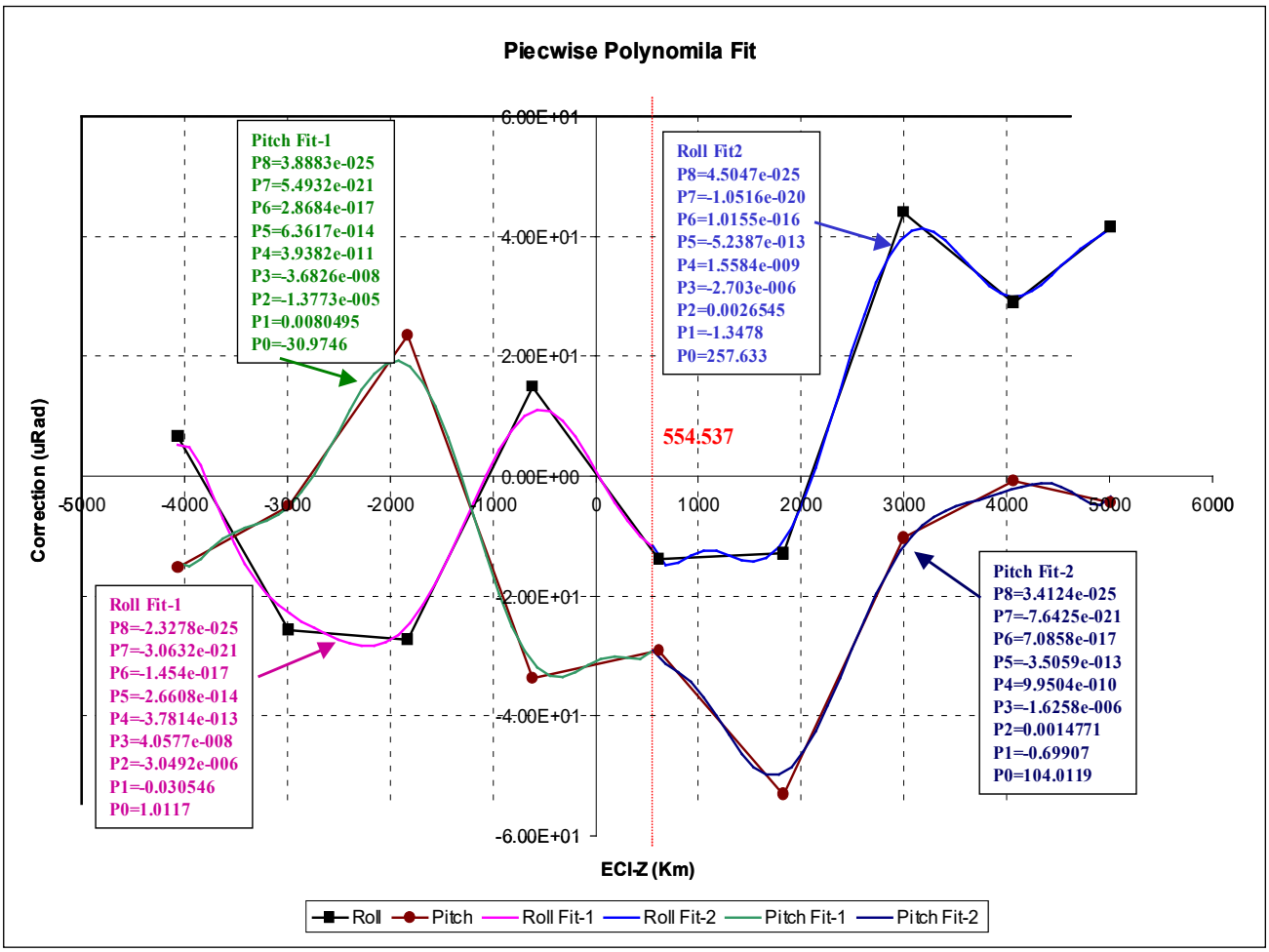

Figure A-5: Orbital Geolocation Error Correction

Table A-17: Valid ECI-Z Ranges - Example 4

ECI-Z Range	-4551.03:554.537	554.537:5423.98	-4551.03:554.537	554.537:5423.98
Polynomial Set	Roll Fit-1	Roll Fit-2	Pitch Fit-1	Pitch Fit-2
Poly Coefs				
P8	-2.3278e-025	4.5047e-025	3.8883e-025	3.4124e-025
P7	-3.0632e-021	-1.0516e-020	5.4932e-021	-7.6425e-021
P6	-1.454e-017	1.0155e-016	2.8684e-017	7.0858e-017
P5	-2.6608e-014	-5.2387e-013	6.3617e-014	-3.5059e-013
P4	-3.7814e-013	1.5584e-009	3.9382e-011	9.9504e-010
P3	4.0577e-008	-2.703e-006	-3.6826e-008	-1.6258e-006
P2	-3.0492e-006	0.0026545	-1.3773e-005	0.0014771
P1	-0.030546	-1.3478	0.0080495	-0.69907
P0 (DC)	1.0117	257.633	-30.9746	104.0119

Population of the Correction Set Index LUT

1. First the number of dimensions (NDIMS) is defined. As with Example 1, only one dimension is required. (NDIMS=1)
2. Set the weighting vector (INW) for dimension 1. Within the input vector, the only term needed for this correction is the ECI-Z term, which is index 5. Thus, the weighting vector will contain the value 1.0 at index 5 and 0.0 everywhere else as shown in Table A-18.

Table A-18: Weight Vector - Example 4

Index	0	1	2	3	4	5	6	….	NUM_INPUTS-1
Weight	0.0	0.0	0.0	0.0	0.0	1.0	0.0	…	0.0

3. Set the number of breakpoints (NBPTS) for this dimension. There are two explicit ranges given. There are two additional ranges off each end of the data-set (-*4551.03* : -∞ and *5423.98* : ∞) for which no correction will be available. This gives a total of 4-ranges. The number of breakpoints will be (NBPTS=*4-1=3*)
4. Define each breakpoint (BPTS). Breakpoints are given for the *4* ranges illustrated in Table A-19. Only 3 actual values are needed to describe these ranges. These 3 values make up the Breakpoint vector.

Table A-19: Breakpoint Vector - Example 4

Quantized Index Value	Range <= ECI-Z <	
0	-∞	-4551.03
1	-4551.03	554.537
2	554.537	5423.98
3	5423.98	∞

5. Next the index values to the *Correction Coefficient LUT* are defined. The total size of this table is given by multiplying NBPTS+1 for each dimension (NDIMS) of the LUT. Since this is a one-dimensional table with four entries the LUT is only four entries in size. Table A-20 gives the index values with their corresponding polynomial set.

Table A-20: Coefficient Indices - Example 4

IDXARRAY Index	Corrections to effective			Index into *Correction Coefficient LUT*
	Roll	Pitch	Yaw	
0	0.0	0.0	0.0	0
1	Roll Fit-1	Pitch Fit-1	0.0	1
2	Roll Fit-2	Pitch Fit-2	0.0	2
3	0.0	0.0	0.0	0

Since the corrections for (IDXARRAY Index=0=3) are both zero they are pointed to the same entry in the *Correction Coefficient LUT.*

6. The *Correction Index LUT* can now be populated with the data given above. The final result should look something like Table A-21.

Table A-21: Correction Index LUT - Example

NAME	Format	Value
TBLIDENT	char[80]	Example-4
TBLGENINFO	char[80]	Piecewise polynomial correction in ECI-Z with seasonal terms.
NDIMS	Byte	1
INW_1	float[NUM_INPUTS]	[0.0, 0.0, 0.0, 0.0, 0.0, 1.0, 0.0, …, 0.0]
$NBPTS_1$	Uint	3
$BPTS_1$	float[NBPTS]	[-4551.03,554.537, 5423.98]
IDXARRAY		[0, 1, 2, 0]

Population of the Correction Coefficient LUT

1. Set the number of coefficients (NC). For this example, the correction function must implement an 8th order polynomial. This can be accomplished by setting NC=17, this gives a correction function of the form:

$$f(x) = C_0 + C_1 \sin(C_2 x + C_3) \exp(C_4 x + C_5) + C_6 \exp(C_7 x + C_8) + C_9 x^1 + C_{10} x^2 + C_{11} x^3 + C_{12} x^4 + C_{13} x^5 + C_{14} x^6 + C_{15} x^7 + C_{16} x^8$$

Setting $C_1 = C_2 = C_3 = C_4 = C_5 = C_6 = C_7 = C_8 = 0$ leaves the polynomial part:

$$f(x) = C_0 + C_9 x^1 + C_{10} x^2 + C_{11} x^3 + C_{12} x^4 + C_{13} x^5 + C_{14} x^6 + C_{15} x^7 + C_{16} x^8$$

The polynomial coefficients given in Table A-17 map to the coefficients in the above equation as described in Table A-22.

Table A-22: Polynomial Coefficients - Example A

P0	P1	P2	P3	P4	P5	P6	P7	P8
C_0	C_9	C_{10}	C_{11}	C_{12}	C_{13}	C_{14}	C_{15}	C_{16}

2. Set the number of independent variables (NIDV). For this example, NIDV=3. The first is for ECI-Z (x), the second is for the DOY (y), and the third is for the YEAR (z).
3. Set the input weighting vector (INWVECT) for each independent variable
   a. The orbital component of the correction is defined in terms of ECI-Z.
   b. The sinusoidal component from Example 3 is the daily yearly fraction that is calculated by the day-of-year divided by 365. .
   c. As with Example 3, the total year fraction component is driven by the YEAR+DOY/365. The resulting weighting vector is shown in Table A-23.

Table A-23: Weighting Vector - Example 4

Index	0	1	2	3	4	5	6	….	NUM_INPUTS-1
Weight	0.0	1/365	1.0	0.0	0.0	0.0	0.0	…	0.0

4. Set the number of entries (NENTRIES) for this table. There are three entries, one for each set of correction terms, using the index values of 0 through 2.
5. Populate the coefficient sets (COEFSET). There are three coefficient sets numbered 0 through 2. Each set consists of 3*NC*NIDV coefficients. For this LUT, there are 3*18*3=162 coefficients per set. The nonzero coefficients for this LUT are shown in Table A-24.

Table A-24: Non-zero Coefficients - Example 4

Set Index	Roll(x) C_0, C_9, C_{10}, …, C_{16}	Roll(y) C_1, C_2, C_3	Roll(z) C_0, C_9	Pitch(x) C_0, C_9, C_{10},… C_{16}	Pitch(y) C_1, C_2, C_3	Pitch(z) C_0, C_9	Yaw(x) Yaw(y) Yaw(z)

0	All Coefficients 0.0	-35.2 2π 5.2	G1 -7.09	All Coefficients 0.0	-35.2 2π 5.2	H1 -7.09	
1	1.0117 -0.030546 -3.0492e-006 4.0577e-008 -3.7814e-013 -2.6608e-014 -1.454e-017 -3.0632e-021 -2.3278e-025	-35.2 2π 5.2	G1 -7.09	-30.9746 0.0080495 -1.3773e-005 -3.6826e-008 3.9382e-011 6.3617e-014 2.8684e-017 5.4932e-021 3.8883e-025	-35.2 2π 5.2	H1 -7.09	All Coefficients are 0.0
2	257.633 -1.3478 0.0026545 -2.703e-006 1.5584e-009 -5.2387e-013 1.0155e-016 -1.0516e-020 4.5047e-025	-35.2 2π 5.2	G1 -7.09	104.0119 -0.69907 0.0014771 -1.6258e-006 9.9504e-010 -3.5059e-013 7.0858e-017 -7.6425e-021 3.4124e-025	-35.2 2π 5.2	H1 -7.09	

6. The LUT can now be populated with the data given above. The final result should look something like Table A-25:

Table A-25: Coefficients LUT - Example 4

Name	Format	Value
TBLIDENT	char[80]	Example-1
TBLGENINFO	char[80]	Correction in ECI-Z for days a-b
NC	Byte	17
NIDV	Byte	3
$INWVECT_0$	float[NUM_INPUTS]	[0.0, 1/365, 0.0, ……. 0.0]
$INWVECT_1$	float[NUM_INPUTS]	[0.0, 1/365, 1.0, ……. 0.0]
$INWVECT_1$	float[NUM_INPUTS]	[0.0, 0.0, 0.0, 0.0, 0.0, 1.0, 0.0 ……. 0.0]
NENTRIES	Uint	3
$COEFSET_0$	float[***coef_per_set****]	All 162 entries are zero
$COEFSET_1$	float[***coef_per_set****]	[Roll(x):set-1] [Roll(y):set-1] [Roll(z):set-1] [Pitch(x):set-1] [Pitch(y):set-1] [Pitch(z):set-1]
$COEFSET_2$	float[***coef_per_set****]	[Roll(x):set-2] [Roll(y):set-2] [Roll(z):set-2] [Pitch(x):set-2] [Pitch(y):set-2] [Pitch(z):set-2]
The Coefficient Values for $COEFSET_1$ and $COEFSET_2$ can be found in Table-X, Values not listed are zero.		

APPENDIX B Euler Angles for Orbital Frame to S/C Frame Using J2000-ECI to S/C Frame Quaternion

1. Expression of Quaternions: J2000 to spacecraft frame

Assume quaternions q_1, q_2, q_3, q_4 are defined by

$$q_1 = e_1 \sin\frac{\Phi}{2} \tag{B-1}$$

$$q_2 = e_2 \sin\frac{\Phi}{2} \tag{B-2}$$

$$q_3 = e_3 \sin\frac{\Phi}{2} \tag{B-3}$$

$$q_4 = \cos\frac{\Phi}{2} \tag{B-4}$$

where Φ is an angle of rotation, and vector $\boldsymbol{e} = (e_1, e_2, e_3)$ axis of rotation with:

$$q_1^2 + q_2^2 + q_3^2 + q_4^2 = 1 \tag{B-5}$$

2. Quaternions to Transformation Matrix(J2000(ECI) to Spacecraft): $T_{sc/eci}$

Based on Wertz[19], a transformation matrix can be expressed by quaternions as below:

$$T_{sc/eci} = \begin{bmatrix} q_1^2 - q_2^2 - q_3^2 + q_4^2 & 2(q_1q_2 + q_3q_4) & 2(q_1q_3 - q_2q_4) \\ 2(q_1q_2 - q_3q_4) & -q_1^2 + q_2^2 - q_3^2 + q_4^2 & 2(q_2q_3 + q_1q_4) \\ 2(q_1q_3 + q_2q_4) & 2(q_2q_3 - q_1q_4) & -q_1^2 - q_2^2 + q_3^2 + q_4^2 \end{bmatrix} \tag{B-6}$$

3. Spaceceraft Orbital Frame to ECI

Let **p** and **v** be spacecraft position and velocity in ECI and **H** be geodetic nadir point on the earth ellipsoid dropped down from **p**.

---

[19] Wertz, J.R. (ed.), 1985. *Spacecraft Attitude Determination and Control*, D. Reidel Publishing Co., Vol. 73, page 414.

Define a vector ***p'*** by $p' = vector\ (H \rightarrow p) = \overrightarrow{Hp}$.

$$\hat{b}_3 = -\,p'/|p'| \tag{B-7}$$

$$\hat{b}_2 = \hat{b}_3 \times v/|\hat{b}_3 \times v| \tag{B-8}$$

$$\hat{b}_1 = \hat{b}_2 \times \hat{b}_3 \tag{B-9}$$

From (B-7), (B-8), (B-9), define

$$T_{eci/orb} = \left[\hat{b}_1 \quad \hat{b}_2 \quad \hat{b}_3\right] \tag{B-10}$$

4. Calculation of Attitude Matrix $T_{sc/orb}$

$$T_{sc/orb} = T_{sc/eci} \times T_{eci/orb} \tag{B-11}$$

5. Calculation of Euler Angles roll, pitch, yaw (ξ_r, ξ_p, ξ_y) from $T_{sc/orb}$

Assuming the matrix is built in the order of operations yaw, roll, and pitch, (called Type 3-1-2). Such a matrix is expressed as

$$T_{sc/orb} =$$

$$\begin{bmatrix} \cos\xi_y \cos\xi_p - \sin\xi_y \sin\xi_r \sin\xi_p & \sin\xi_y \cos\xi_p + \cos\xi_y \sin\xi_r \sin\xi_p & -\cos\xi_r \sin\xi_j \\ -\sin\xi_y \cos\xi_r & \cos\xi_y \cos\xi_r & \sin\xi_r \\ \cos\xi_y \sin\xi_p + \sin\xi_y \sin\xi_r \cos\xi_p & \sin\xi_y \sin\xi_p - \cos\xi_y \sin\xi_r \cos\xi_p & \cos\xi_r \cos\xi_p \end{bmatrix} \tag{B-12}$$

$$\equiv |a_{ij}|$$

Assuming the absolute values of all angles are less than 90 degrees,

$$\xi_r = \sin^{-1} a_{23} \tag{B-13}$$

$$\xi_p = \sin^{-1}(-a_{13} / \cos \xi_r) \tag{B-14}$$

$$\xi_y = \sin^{-1}(-a_{21} / \cos \xi_r) \tag{B-15}$$

Note: If any of the absolute value of attitude angles are equal to or greater than 90 degrees, various combinations of tests may be needed.

APPENDIX C JPSS-1 VIIRS DNB Aggregation Mode Change to Mitigate DNB Non-linearity

Based on prelaunch testing, JPSS-1 (J1) VIIRS DNB shows high non-linearity in radiometric response especially at the edge of scans, which is different from the behavior of NPP VIIRS (see J1 waiver documentation: RDW_VIIRS-W174A_v2). The J1 data working group proposed two onboard aggregation options in order to mitigate the DNB nonlinearity:

(1) Option 21 (Op21) which extends aggregation mode 21 up to 32;
(2) Option 21/26 (Op21/26) which extends aggregation mode 21 up to 25 and aggregation mode 26 up to 32.

The VIIRS SDR team recommended that Op21 should be the baseline aggregation mode for J1 DNB. J1 operational calibration for ground processing uses Op21 for DNB aggregation scheme. Table C-1 and Table C-2 show the DNB aggregation for J1 Op21 from the start to end of scan. Table C-2 presents the Op21 aggregation scheme in a more concise way compared Table C-1 by consolidating consecutive aggregation zones with the same aggregation mode. Table C-3 shows DNB aggregation for Op21/26 from the start to end of scan. Final selection of the J1 aggregation option to be used for the operational SDR product generation will be determined after launch.

Due to the J1 DNB aggregation mode change, VIIRS GEO code was modified in order to correctly calculate DNB sample time offsets and extrapolate encoder data for the J1 DNB extended EV samples, to compute DNB nadir sample number, and to calculate interpolation rectangles. The code change is backward compatible with Suomi NPP (SNPP). ADR 8036 documentations provide detailed information about the VIIRS GEO code change.

Figure C-1 compares ground sample distances for SNPP, Op21, and Op21/26 during a 4064-frame scan. While SNPP aggregation scheme provides near constant pixel growth for the entire scan (Figure 3.3-14), J1 options result in larger pixel growth at BOS and EOS, especially for the J1 DNB extended EV area in the along-scan direction. Op21 has larger pixel growth than Op21/26. Moreover, compared to SNPP (see Figure 3.3-15, the 2032th pixel is nadir), J1 DNB aggregation options are asymmetric about nadir, with nadir located at the 1986th pixel for Op21 and the 1976th pixel for Op21/26.

Table C-1: DNB Aggregation for J1 Op21 (BOS to EOS)

Beginning of Scan to Nadir				Nadir to End of Scan			
Index	Aggregation Mode	Lower pixel	Upper pixel	Index	Aggregation Mode	Lower pixel	Upper pixel
1	**32**	**0**	**7**	33	**1**	**1896**	**2071**
2	**21**	**8**	**15**	34	**1**	**2072**	**2079**
3	**21**	**16**	**239**	35	**2**	**2080**	**2143**
4	**21**	**240**	**247**	36	**2**	**2144**	**2151**
5	**21**	**248**	**463**	37	**3**	**2152**	**2231**
6	**20**	**464**	**471**	38	**3**	**2232**	**2239**
7	**20**	**472**	**495**	39	**4**	**2240**	**2303**
8	**19**	**496**	**503**	40	**4**	**2304**	**2311**
9	**19**	**504**	**543**	31	**5**	**2312**	**2391**
10	**18**	**544**	**551**	42	**6**	**2392**	**2463**
11	**18**	**552**	**575**	43	**7**	**2464**	**2527**
12	**17**	**576**	**647**	44	**8**	**2528**	**2591**
13	**16**	**648**	**719**	45	**9**	**2592**	**2655**
14	**15**	**720**	**791**	46	**10**	**2656**	**2719**
15	**14**	**792**	**871**	47	**11**	**2720**	**2783**
16	**13**	**872**	**927**	48	**12**	**2784**	**2863**
17	**12**	**928**	**1007**	49	**13**	**2864**	**2919**
18	**11**	**1008**	**1071**	50	**14**	**2920**	**2999**
19	**10**	**1072**	**1135**	51	**15**	**3000**	**3071**
20	**9**	**1136**	**1199**	52	**16**	**3072**	**3143**
21	**8**	**1200**	**1263**	53	**17**	**3144**	**3215**
22	**7**	**1264**	**1327**	54	**18**	**3216**	**3239**
23	**6**	**1328**	**1399**	55	**18**	**3240**	**3247**
24	**5**	**1400**	**1479**	56	**19**	**3248**	**3287**
25	**4**	**1480**	**1487**	57	**19**	**3288**	**3295**
26	**4**	**1488**	**1551**	58	**20**	**3296**	**3319**
27	**3**	**1552**	**1559**	59	**20**	**3320**	**3327**
28	**3**	**1560**	**1639**	60	**21**	**3328**	**3543**
29	**2**	**1640**	**1647**	61	**21**	**3544**	**3551**
30	**2**	**1648**	**1711**	62	**21**	**3552**	**3559**
31	**1**	**1712**	**1719**	63	**21**	**3560**	**3567**
32	**1**	**1720**	**1895**	64	**21**	**3568**	**4063**

Table C-2: Consolidated DNB Aggregation for J1 Op21 (BOS to EOS)

Aggregation Mode	Number of pixels per mode	Aggregation Mode	Number of pixels per mode
32	8	1	368
21	456	2	72
20	32	3	88
19	48	4	72
18	32	5	80
17	72	6	72
16	72	7	64
15	72	8	64
14	80	9	64
13	56	10	64
12	80	11	64
11	64	12	80
10	64	13	56
9	64	14	80
8	64	15	72
7	64	16	72
6	72	17	72
5	80	18	32
4	72	19	48
3	88	20	32
2	72	21	736

Table C-3: DNB Aggregation for J1 Op21/26 (BOS to EOS)

Beginning of Scan to Nadir				Nadir to End of Scan			
Index	Aggregation Mode	Lower pixel	Upper pixel	Index	Aggregation Mode	Lower pixel	Upper pixel
1	**32**	**0**	**7**	33	**1**	**1976**	**2151**
2	**26**	**8**	**15**	34	**1**	**2152**	**2159**
3	**26**	**16**	**327**	35	**2**	**2160**	**2223**
4	**21**	**328**	**335**	36	**2**	**2224**	**2231**
5	**21**	**336**	**543**	37	**3**	**2232**	**2311**
6	**20**	**544**	**551**	38	**3**	**2312**	**2319**
7	**20**	**552**	**575**	39	**4**	**2320**	**2383**
8	**19**	**576**	**583**	40	**4**	**2384**	**2391**
9	**19**	**584**	**623**	31	**5**	**2392**	**2471**
10	**18**	**624**	**631**	42	**6**	**2472**	**2543**
11	**18**	**632**	**655**	43	**7**	**2544**	**2607**
12	**17**	**656**	**727**	44	**8**	**2608**	**2671**
13	**16**	**728**	**799**	45	**9**	**2672**	**2735**
14	**15**	**800**	**871**	46	**10**	**2736**	**2799**
15	**14**	**872**	**951**	47	**11**	**2800**	**2863**
16	**13**	**952**	**1007**	48	**12**	**2864**	**2943**
17	**12**	**1008**	**1087**	49	**13**	**2944**	**2999**
18	**11**	**1088**	**1151**	50	**14**	**3000**	**3079**
19	**10**	**1152**	**1215**	51	**15**	**3080**	**3151**
20	**9**	**1216**	**1279**	52	**16**	**3152**	**3223**
21	**8**	**1280**	**1343**	53	**17**	**3224**	**3295**
22	**7**	**1344**	**1407**	54	**18**	**3296**	**3319**
23	**6**	**1408**	**1479**	55	**18**	**3320**	**3327**
24	**5**	**1480**	**1559**	56	**19**	**3328**	**3367**
25	**4**	**1560**	**1567**	57	**19**	**3368**	**3375**
26	**4**	**1568**	**1631**	58	**20**	**3376**	**3399**
27	**3**	**1632**	**1639**	59	**20**	**3400**	**3407**
28	**3**	**1640**	**1719**	60	**21**	**3408**	**3615**
29	**2**	**1720**	**1727**	61	**21**	**3616**	**3623**
30	**2**	**1728**	**1791**	62	**26**	**3624**	**3631**
31	**1**	**1792**	**1799**	63	**26**	**3632**	**3639**
32	**1**	**1800**	**1975**	64	**26**	**3640**	**4063**

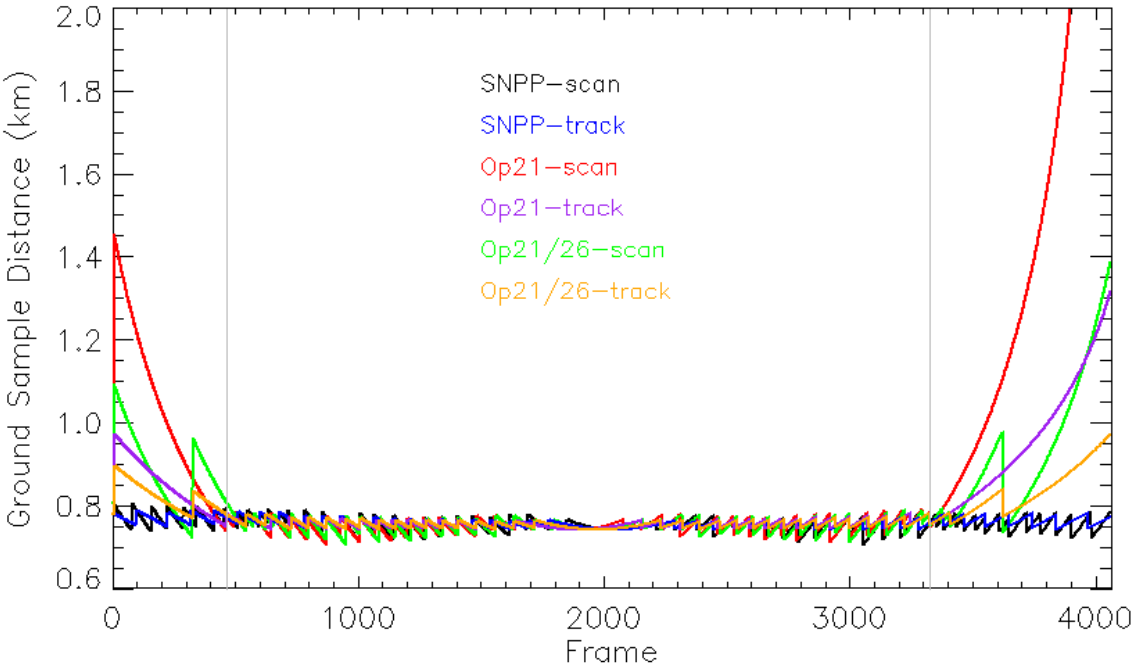

Figure C-1: Ground sample distances for SNPP, J1 Op21, and J1 Op21/26 in the along-scan and along-track directions.